Electrical Characterization of High Temperature Superconductors as a Function of Temperature

By

Timothy A. MacDonald

B.S., Nuclear Engineering 1997
Texas A&M University

Submitted to the Department of Nuclear Engineering in Partial Fulfillment of the Requirements for the Degree of

Master of Science in Nuclear Engineering
At the
Massachusetts Institute of Technology

June 2000

Signature of Author: _____
Department of Nuclear Engineering
May 1, 2000

Certified by: _____
Joseph Minervini, Ph.D
PSFC Technology and Engineering Division Head
Thesis Supervisor

Certified by: _____
Ian Hutchinson, Ph.D
Professor, Department of Nuclear Engineering
Thesis Reader

Accepted by: _____
Sow-Hsin Chen, Ph.D
Chairman, Committee for Graduate Students

Electrical Characterization of High Temperature Superconductors as a Function of Temperature

by

Timothy A. MacDonald

Submitted to the Department of Nuclear Engineering in Partial Fulfillment of the Requirements for the Degree of
Master of Science in Nuclear Engineering

Abstract

The critical currents of silver sheathed multifilamentary $Bi_2Sr_2Ca_2Cu_3O_{10}$ (BSCCO-2223/Ag) tapes at temperatures ranging from 77 K to 110 K were measured using a typical four-terminal technique for two different BSCCO-2223/Ag tapes manufactured by Vacuumschmelze (VAC). The critical currents for the two VAC samples were measured as a function of magnetic field strength. The critical current of each sample was well described by the generalized Kim model. The critical current was also measured as a function of angle of the magnetic field with respect to the plane of the tapes, in all cases perpendicular to the transport current flow. Both samples displayed a high sensitivity to the magnetic field orientation with the largest critical currents measured when the magnetic field was in-plane with the broad face of the tapes. The current ramp rate effect on the critical current was investigated and showed no significant effect on the critical current measurements for ramp speeds between 6 A/min and 120 A/min.

The energy dissipation or AC losses as a function of peak AC magnetic field, magnetic field sweep frequency, and transport current for a VAC sample and a sample manufactured by IGC – Advanced Superconductors (IGC) were measured at 77 K. The losses were measured using a pick up coil with a lock-in amplifier to measure the magnetization of the superconducting samples. The AC losses of both samples displayed complete electromagnetic coupling of the superconducting filaments at magnetic sweep frequencies of approximately 0.1 Hz. These results are consistent with results measured at magnetic field sweep frequencies of 60 Hz.

Thesis Supervisor: Dr. Joseph Minervini
Thesis Reader: Professor Ian Hutchinson

Contents

List of Figures

List of Tables

1 Introduction

Superconductivity is the ability of a material to carry DC electric current with absolutely no resistance. Superconductors do, however, experience energy loss in the presence of AC magnetic fields or while transporting AC electric current. Since superconductors are growing more popular for applications in high-current and high-field physics and engineering, understanding and quantifying AC loss mechanisms becomes increasingly important to the design and operation of systems utilizing superconducting technology.

1.1 Brief History of Superconductivity

In 1908, Kamerlingh Onnes developed methods to liquefy helium and was capable of reaching temperatures down to about 1 K for the first time anywhere on earth. One of the foremost experiments Onnes completed utilizing his newly available low-temperature range was a study of the variation of the electrical resistance of metals with temperature. While it was well known that resistance decreases linearly when metals are cooled below room temperature, there was great debate concerning the limiting value of resistance as the temperature approached absolute zero. Onnes discovered that the resistance of platinum fell to a low value that depended on the purity of the sample. At that time, the purest metal available to Onnes was mercury, and he soon found that the resistance of mercury at very low temperatures became immeasurably small, which was to be expected. However, in 1911, Onnes discovered that the manner in which the resistance of the mercury decreased was completely unexpected. Instead of decreasing linearly as the temperature approached 0 K, the resistance drops sharply at a temperature of about 4

K. Onnes also observed this sudden transition to a state of no resistance in quite impure samples of mercury. Onnes recognized that the electrical properties of mercury below 4 K are quite unlike those properties exhibited at room temperature. This state of no resistance is called the *superconducting state*.

Once Onnes discovered the behavior of certain materials in the very low-temperature range he quickly realized the implications of this new technology. With no resistance to flowing electrical currents, electromagnets would be capable of producing extremely large magnetic fields but require no power to run in steady state. Onnes soon discovered other critical properties of superconductors that prevented him from building these powerful magnets. As well as a critical temperature (T_c), superconductors are subject to a critical magnetic field (H_c) and a critical electrical current density (J_c) and will revert to the normal state if it is exposed to conditions that exceed these criteria. And for the known superconductors of Onnes time, the J_c and H_c are quite low, and thus incapable of providing useful magnetic fields.

The decades of research and development on the theory of superconductivity and on the production of superconducting materials have allowed superconductors to begin to realize their potential. Large-scale, high current and high field superconducting magnets have become very popular in various areas such as magnetic-confinement nuclear fusion, high-energy particle acceleration, and magnetic levitation. They are currently replacing copper electromagnets because the superconducting magnets produce high fields over large volumes while the refrigeration costs are much less expensive than the costs of

cooling copper magnets. The development of superconductors has lead to materials that stay in the superconducting state at temperatures up to 120 K. With more study and development, perhaps a superconductor at room temperature will be available someday.[1,2,3]

1.2 Applications of Superconductors

Superconductors are most commonly used in large electromagnets. An application of superconducting magnets that has had an enormous impact on society is magnetic resonance imaging or MRI. MRI readings have become an invaluable, non-invasive tool for the diagnosis of injuries and health problems as well as a means to map brain activity. Superconducting magnets have become widely recognized as essential research tools in other fields such as high-energy physics, magnetic-confinement nuclear fusion, particle acceleration, etc. Superconducting magnets are capable of generating extremely large magnetic fields with relatively small power consumption and refrigeration costs. In contrast, well-designed copper electromagnets dissipate large amounts of energy and require ample cooling. The power supplies and cooling systems are very large and very expensive to operate and maintain. The following sections outline a short list of several areas utilizing superconducting technology.[2,4]

1.2.1 Thermonuclear Fusion

Magnetic confinement has been a major area of study towards the commercial production of power from controlled thermonuclear fusion. Fusion is based on the reaction of two light nuclei combining into one larger nucleus accompanied by a large release of energy.

The fusion reaction begins with plasmas. A plasma is a gas in which a significant fraction of the atoms is ionized. For ionization to occur, the plasma's temperature must be raised to temperatures comparable to that of the sun and confined to a relatively small volume. Since there are no known materials that can withstand the intense heat of fusing plasma, large magnetic fields are used to suspend and contain the plasma. However, in order to achieve a net power-out using magnetic confinement, the magnetic fields must be produced using superconducting magnets because the power consumption of conventional copper magnets would probably exceed the electrical output of the power plant.[2]

Most existing experiments in plasma fusion constructed to date have used conventional magnets, although several superconducting devices have been built and more are currently under construction. The Central Solenoid Model Coil (CSMC) is one such device. The CSMC is a direct result of the work towards the International Thermonuclear Experimental Reactor (ITER). ITER is an international research effort working to build a tokamak reactor with the intention to demonstrate the capability of producing fusion power for commercial use and is one of the superconducting fusion facilities in development today. The CSMC is the largest pulsed superconducting magnet existing today. It was constructed from multi-stage superconducting cables based on the cable-in-conduit-conductor (CICC) technology.[4]

A cable-in-conduit-conductor is a superconducting cable housed in a conduit usually made of Incoloy® Alloy 908. The conduit provides mechanical support for handling of

the cable, which is very brittle after heat treatment, and can also serve as distributed structure within the winding pack. The conduit also provides an insulated channel for the forced flow of cryogen necessary for the operation of the superconducting cable. The cables are constructed by twisting three individual strands of superconductor to create sub-cables. The sub-cables are further twisted in stages with a sequence of 3 x 4 x 5 x 6 to complete the superconducting cable. The multi-stage superconducting cable can carry high currents in high magnetic fields with fast ramp rates. The resulting cable has over 1100 strands of superconductor and can carry 50 kA at 13 T. Fig 1.1 shows a cut-away and cross-sectional view of a CICC. Six sub-cables and the cryogen channel are readily apparent in the cross-sectional view of the CICC.[5,6,7]

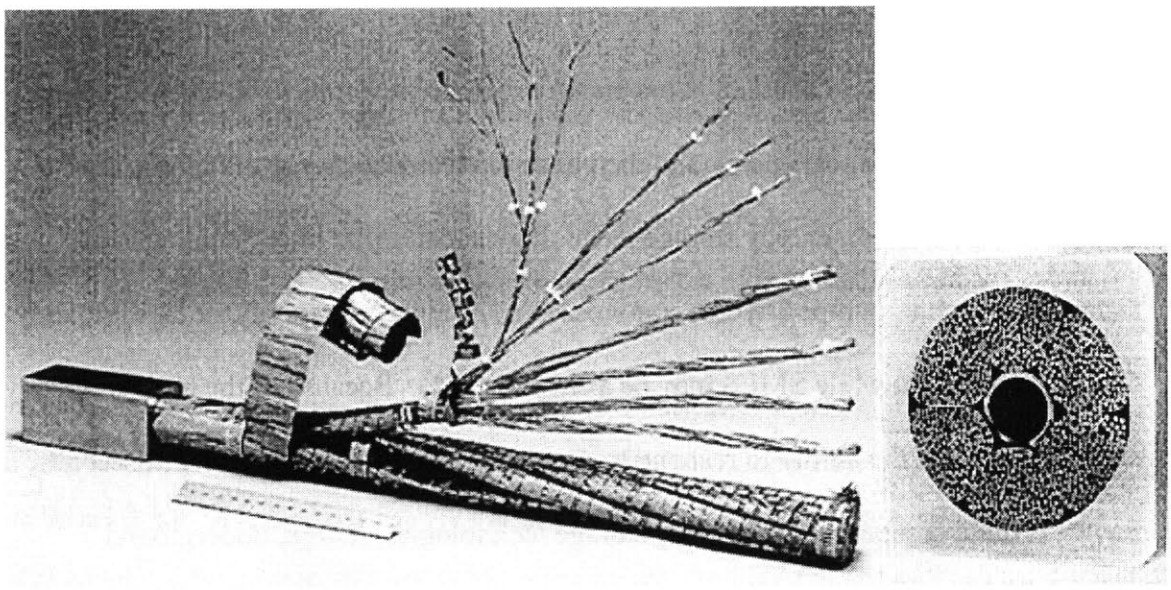

Figure 1.1 Cut-away and cross-sectional view demonstrating cable-in-conduit-conductor technology of twisting individual strands into sub-cables. This CICC was designed for the ITER CSMC.

1.2.2 High Energy Physics

Researchers in areas of high-energy physics utilize magnetic fields in order to accelerate, focus, manipulate, and analyze beams of energetic charged particles. Superconducting magnets are replacing the conventional magnets at reduced operating costs. Superconducting magnets also generate higher magnet fields and allow investigation into areas that conventional magnets simply cannot reach.[2]

1.2.3 Energy Storage

Superconducting magnets have been proposed in a variety of applications where it is necessary to transfer electrical energy back and forth or to store it for prolonged periods of time. The energy density stored in a 10 T magnetic field is larger than capacitor banks, comparable with flywheels, and somewhat less than batteries. Superconducting Magnet Energy Storage (SMES) is very efficient because there is no conversion of energy from one form to another. Conversion processes that transform electrical energy to mechanical or chemical energy and then back to electrical energy are inherently inefficient. As a result, energy storage technologies that utilize energy conversion techniques, such as pumped hydro, compressed air, and battery energy storage, are only 65 to 75% efficient while SMES may be as high as 95%. Because of the high efficiency characteristic and the ability to respond to power demands within tens of milliseconds, SMES is quite competitive with other storage technologies. Large, underground superconducting magnets have been proposed to even out the daily variations in electrical power demands while smaller systems are being used for power conditioning, power

compensation, active filters, power modulation, voltage control, spinning reserve, uninterruptible power supplies, and power system stabilization.[2,8,9]

1.2.4 Magnetic Separation

Magnetic separation has long been used in industry to concentrate iron ores or separate scrap from other materials. The process utilizes the naturally occurring magnetization properties of many materials. In the presence of a magnetic field, many materials become magnetized and are subjected to a force if placed in a magnetic field gradient. The materials will either be pulled towards the high field (paramagnetic materials) or they will be pushed away from it (diamagnetic materials). Large magnetic field gradients maximize the separation force. This effect can be used to capture particles, usually from some type of slurry flow stream.[10]

1.2.5 Magnetic Levitation

Magnetically levitated transport is not new and Japan has already demonstrated a magnetically levitated train capable of traveling at speeds of 550 km/hr unmanned and 531 km/hr manned, which are the world speed records for rail travel. Fig 1.2 shows a photograph of the test vehicle that set the world rail speed records at the Yamanashi Maglev Test Line, which is about 100 km west of Tokyo. Stable levitation is achieved through an interaction between diamagnetic copper loops on the track and an array of superconducting magnets on the train. At zero speed, there is no force between the coils and the superconducting magnets, and, therefore, the train must accelerate on wheels. As the speed increases, eddy currents are induced to flow in such a direction that the train is

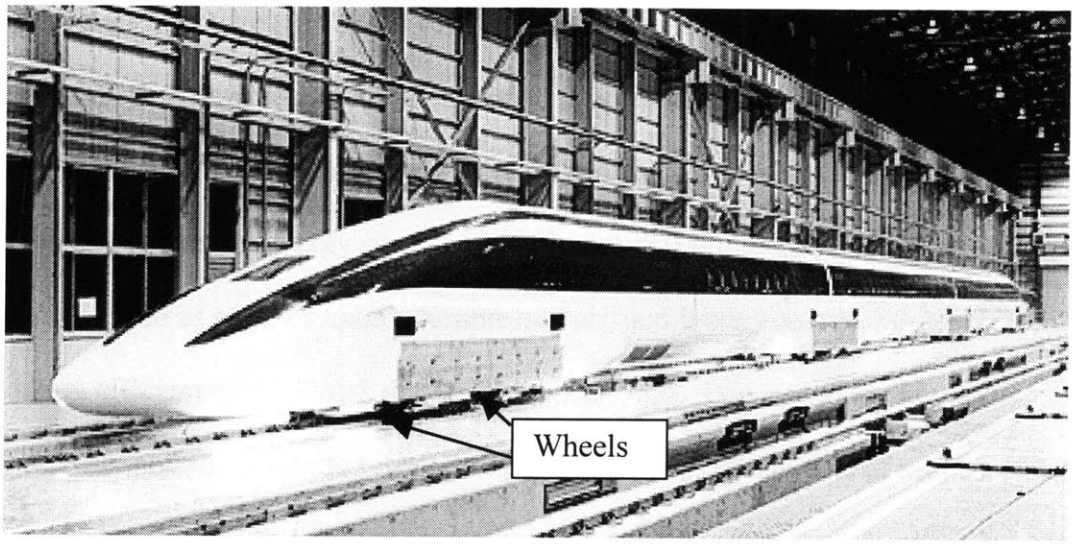

Figure 1.2 The magnetically levitated train test vehicle MLX01 of the Japanese National Railways, maximum speed 550 km/hr.[13,14]

repelled from the copper coils in the track. As the train passes the critical speed, the repulsive force exceeds the train's weight and it takes off. The train is now levitated on a cushion of magnetic field and propelled by a traveling wave of magnetic field, generated by a linear synchronous motor. Since there are no moving parts, the ride is smooth and quiet, and high speeds may be reached safely. Magnetically-levitated transport systems realize super-high-speed travel while maintaining a low environmental impact and passenger safety.[11,12,13,14]

1.3 Superconductors and Perfect Conductors

1.3.1 Zero Resistance

To get a true understanding of superconductors, the property of electrical resistance must be understood. Electric current is the result of electron motion in the conduction band. These electrons can be represented as plane waves and the material is represented as a rigid crystalline structure of atoms lying on a repeating lattice. A property of the plane wave is that it can pass through a perfectly periodic structure without being scattered in several directions. Therefore, if an electron or plane wave was moving through a perfect material or crystal lattice, then the electron or plane wave could pass with no resistance. However, there are two ways in which the perfect lattice of the material is upset. At temperatures above 0 K, the lattice atoms are vibrating and will be displaced by certain distances from their equilibrium. Also, impurities in the material will interrupt the perfect periodicity of the crystal lattice.[1]

Fig 1.3 shows the variation of electrical resistance of impure and perfectly pure metals as a function of temperature. Readily observed is the linear decrease of resistance with temperature. This is attributable to the decreasing atom motion in the lattice with the

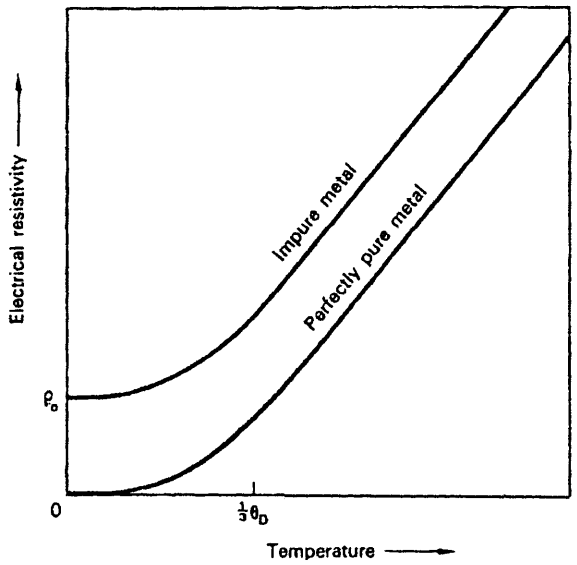

Figure 1.3 Variation of resistance with temperature for pure and impure metals.[1]

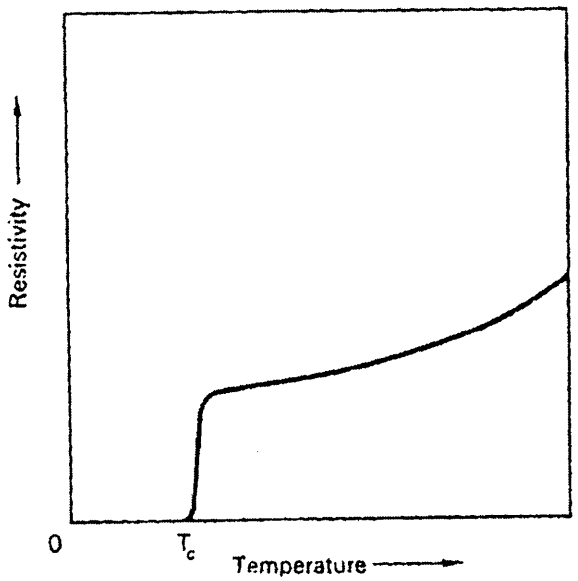

Figure 1.4 Resistivity versus temperature plot illustrating the transition to the superconducting state.[1]

decreasing temperature. For the impure case, there is a certain residual resistivity, which remains as the temperatures approach 0 K caused by the defects in the crystal lattice. For a perfect metal, it is shown that the residual resistivity approaches zero as the temperature approaches zero. However, this zero resistance of a perfect conductor is not the phenomenon of superconductivity.[1]

Fig 1.4 shows the loss of resistance at a certain temperature, T_c, for a superconductor. This temperature at which a superconductor loses its resistance is called the critical temperature. As was mentioned before, critical temperature is not the only property that characterizes the superconducting state. There also exists a critical magnetic field, H_c, and a critical current density, J_c. The critical magnetic field is the maximum magnetic field a superconductor can be exposed to and remain in the superconducting state, and the

critical current density is the maximum electrical current a material can transport before reverting back to the normal or non-superconducting state. Together, these three criteria form what is called the superconducting critical surface. Fig 1.5 shows the critical surface for a typical superconductor in arbitrary units.[1,15]

Another fundamental magnetic phenomenon exhibited by superconductors is their ability to expel a magnetic field from the interior of the bulk superconductor material when the material is cooled below the transition or critical temperature, T_c. The behavior is a characteristic of materials possessing perfect diamagnetism. This characteristic was discovered by Meissner and Ochsenfeld and hence is called the Meissner effect [16].

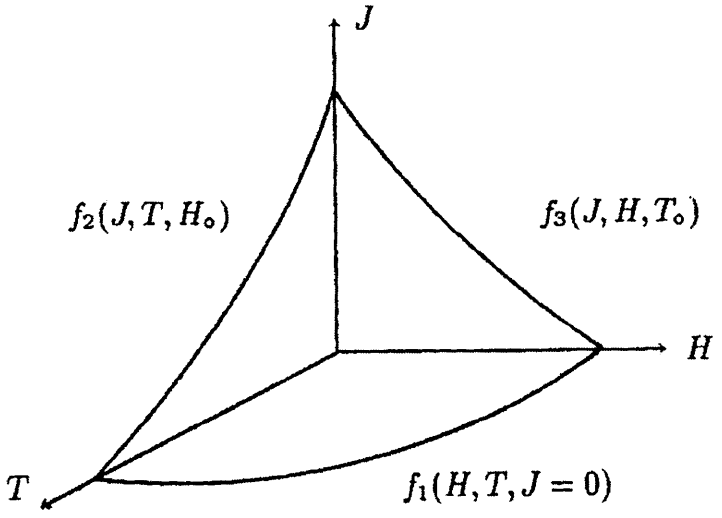

Figure 1.5 Critical surface of a typical superconductor.[15]

1.3.2 Meissner Effect

The sequence of pictures shown in Fig 1.6 and Fig 1.7 outlines the difference between perfect conductivity and perfect diamagnetism. The characteristic behavior of a perfect conductor is dB/dt = 0. Fig 1.6(a) and Fig 1.6(e) show a perfect conductor initially in the absence of an external magnetic field and in the presence of an external magnetic field at room temperature, respectively. In the absence of the magnetic field, the material is cooled and changes to a state of perfect conduction. Then a magnetic field is applied. Since the amount of flux enclosed within the perfect conductor cannot change, all the magnetic flux is expelled from the interior of the conductor and the material remains unmagnetized when the magnetic field is removed. Similarly, when the perfect conductor is exposed to a magnetic field at room temperature and then cooled to the perfect conducting state, the amount of magnetic flux enclosed within the conductor area remains constant. Therefore, the material remains magnetized when the magnetic field is removed. A surface current is induced in the perfect conductor to maintain the original flux distribution.

Fig 1.7(a) and Fig 1.7(e) show a superconductor initially in the absence of an external magnetic field and in the presence of an external magnetic field at room temperature, respectively. Unlike the perfect conductor, superconductors are diamagnetic materials. Perfect diamagnetism is characterized by B = 0 everywhere in the material. Surface supercurrents are induced after the transition to the superconducting state and completely screen the interior region of the bulk superconductor, regardless of the initial condition.

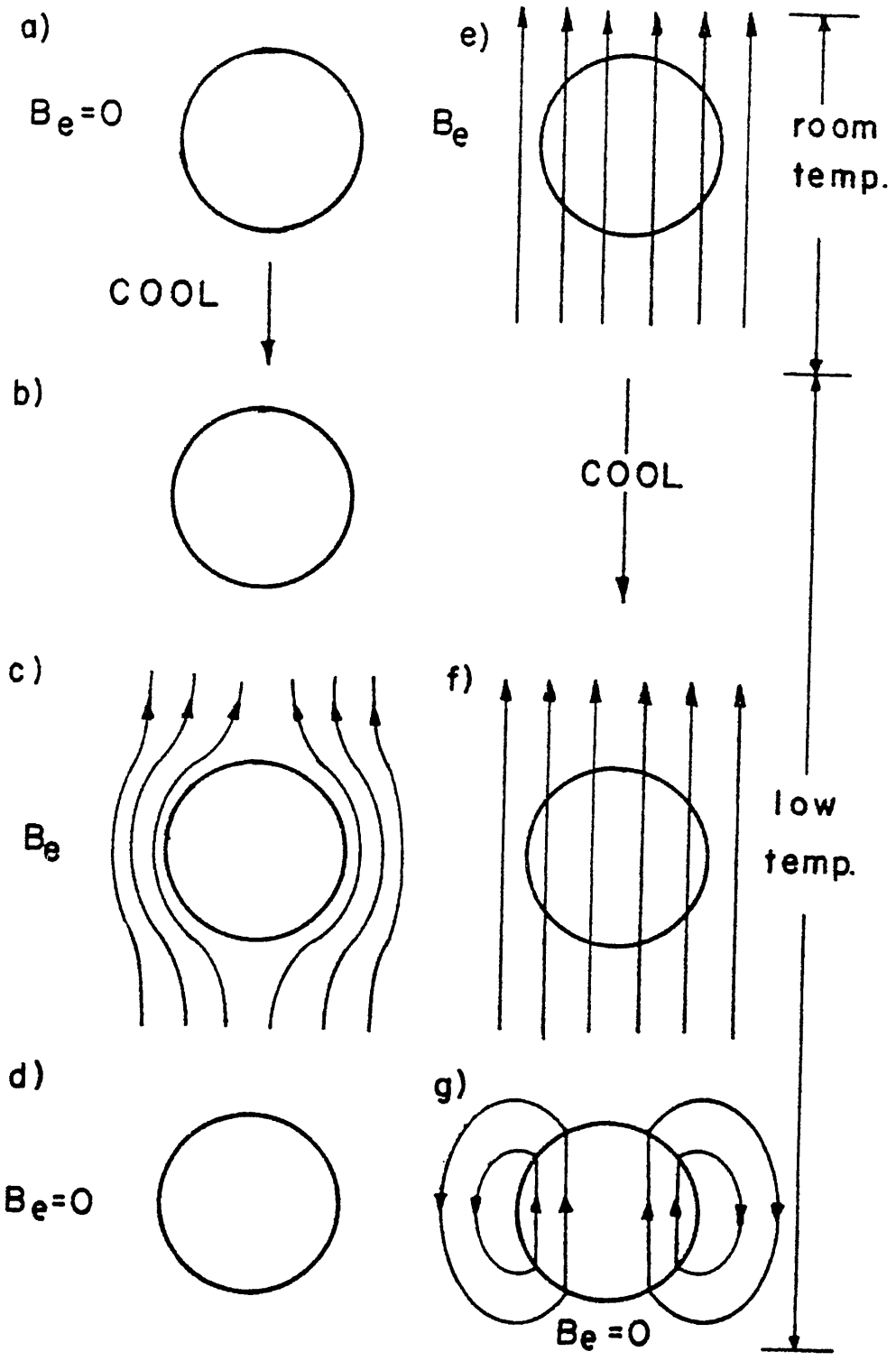

Figure 1.6 A perfect conductor exhibiting a magnetic behavior of dB/dt = 0.[1,3]

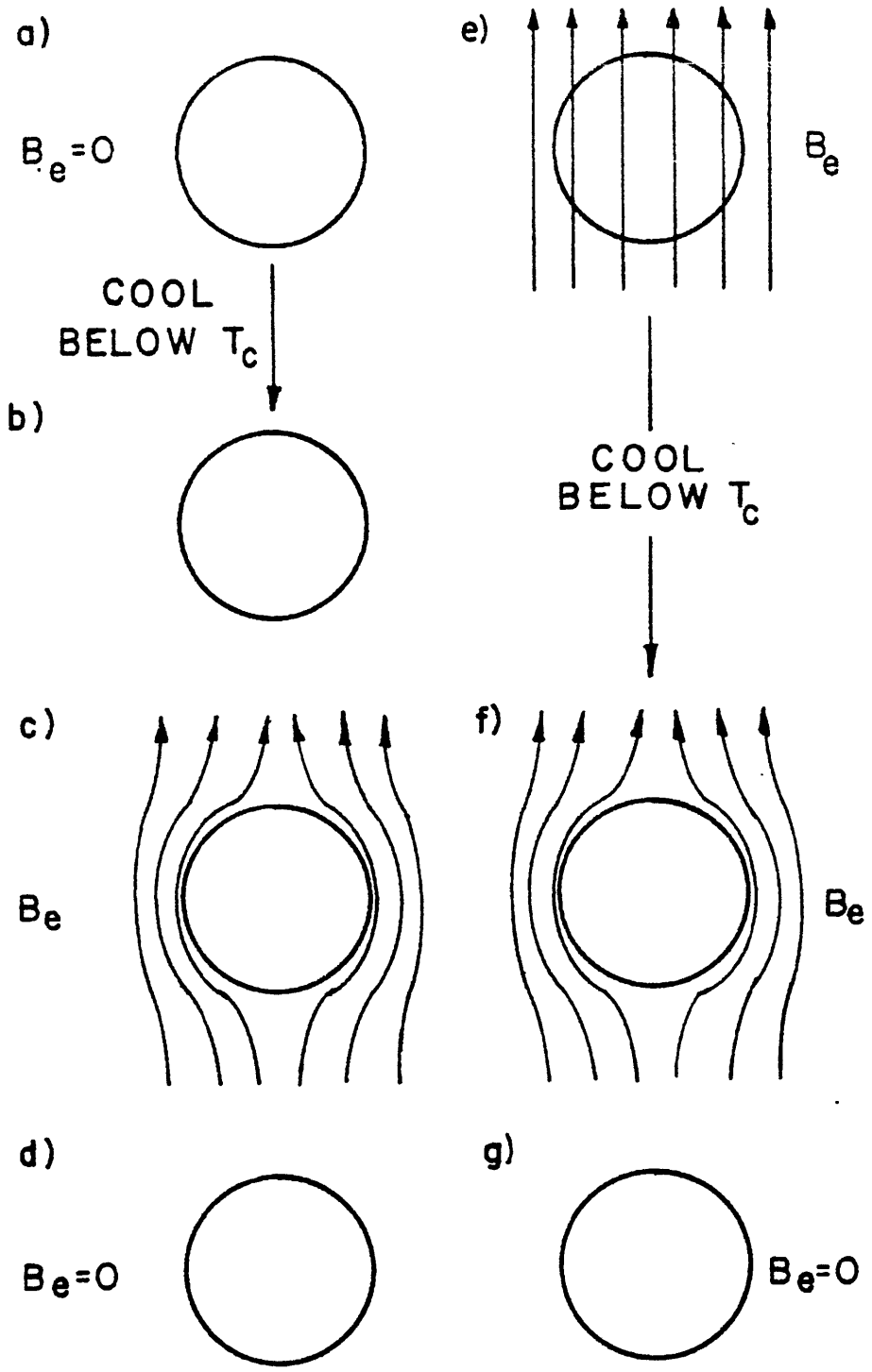

Figure 1.7 Superconductor exhibiting the magnetic property of diamagnetism, B = 0.[1,3]

Under steady state conditions, the superconductor has zero resistance and the screening currents persist indefinitely.

Fig 1.8 shows a demonstration of the Meissner effect. The figure shows a small permanent magnet next to the tip of a pencil levitated above a disk of the superconductor $YBa_2Cu_3O_7$ (YBCO) due to the superconductor's property of expelling magnetic flux. The surface supercurrents induced in the YBCO disk oppose the magnetic field from the permanent magnet. The force between the opposing magnetic fields is greater than the weight of the magnet, and, therefore, the permanent magnet floats above the superconductor.[1,3,4,15]

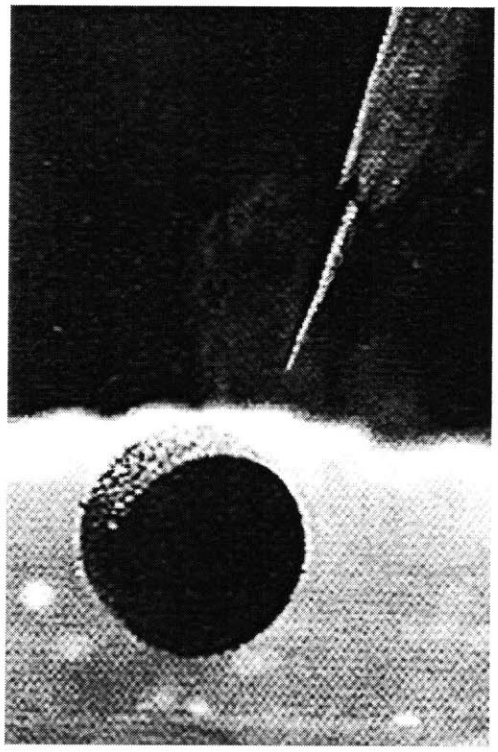

Figure 1.8 A small permanent magnet levitated above a disk of superconductor.[17]

1.3.3 London Penetration Depth

F. and H. London proposed a set of equations known as the London equations to describe the observed magnetic behavior of superconductors [18]. These equations are[1]

$$\mathbf{B} = -\frac{m}{n_s e^2}\nabla \times \mathbf{J} \tag{1.1}$$

and[1]

$$\frac{\partial \mathbf{J}}{\partial t} = \frac{n_s e^2}{m}\mathbf{E} \tag{1.2}$$

where n_s is the number of super electrons per unit volume, m is the electron mass, and e is the electric charge. Eq (1.1) and Eq (1.2) together describe the electrodynamics of the supercurrent. Eq (1.1) describes the diamagnetism, and Eq (1.2) describes the zero resistance property of a superconductor, namely there being no electric field unless the current is changing. Eq (1.1) can be rewritten using Maxwell's equations, $\nabla \times \frac{\mathbf{B}}{\mu_0} = \mathbf{J}$ and $\nabla \cdot \mathbf{B} = 0$. The expression is given in Eq (1.3) in the following form[1]

$$\nabla^2 \mathbf{B} = \frac{1}{\lambda_L^2}\mathbf{B} \tag{1.3}$$

where

$$\lambda_L^2 = \frac{m}{\mu_0 n_s e^2} \tag{1.4}$$

λ_L is the London penetration depth. This expression shows the interior is exponentially screened from the applied field and, therefore, agrees with the Meissner effect. For a one-dimensional slab in a uniform external magnetic field, Eq (1.3) can be written as[1]

$$\frac{\partial^2 B(x)}{\partial x^2} = \frac{1}{\lambda_L^2}B(x) \tag{1.5}$$

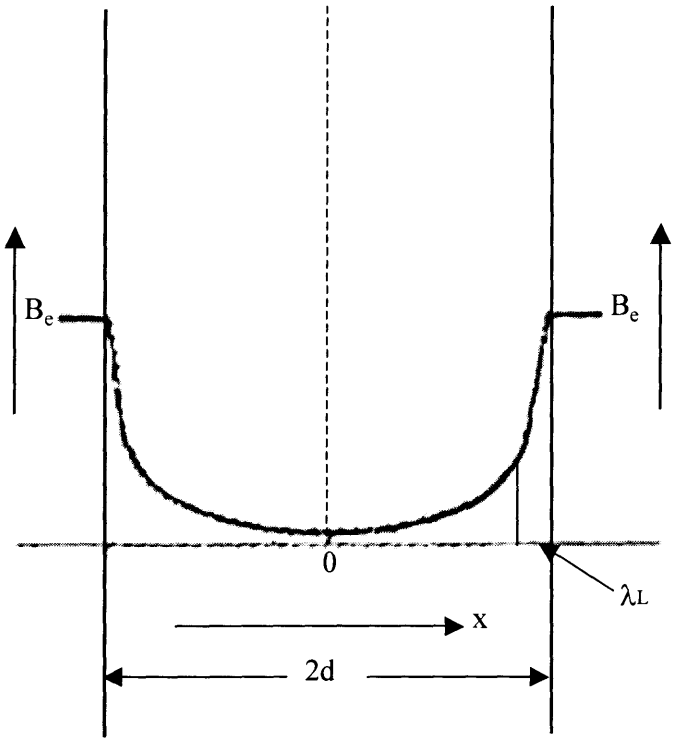

Figure 1.9 Magnetic field profile in a superconducting slab in a parallel applied magnetic field.

which has the solutions of the form[1]

$$B(x) = C_1 e^{\frac{x}{\lambda_L}} + C_2 e^{-\frac{x}{\lambda_L}} \tag{1.6}$$

For $B(\pm d) = B_e$, Eq (1.6) reduces to the following expression

$$B(x) = \frac{B_e}{\cosh\left(\frac{d}{\lambda_L}\right)} \cosh\left(\frac{x}{\lambda_L}\right) \tag{1.7}$$

Fig 1.9 shows the field profile in the slab superconductor calculated from Eq (1.7). Inserting the usual values of the electron mass and electric charge and taking n_s to be about $4 \times 10^{28}\,m^{-3}$, a typical value for the concentration of conduction electrons in metals, the London penetration depth is on the order of 10^{-5} mm. The London penetration depth

is based upon classical theory and is only qualitatively correct. However, the London parameter is good to within a factor of 2.[1]

1.4 Type I and Type II Superconductors

Superconductors are categorized into either a type-I or type-II conductor based on their magnetic properties. Fig 1.10 shows the H-T phase diagrams for both types of superconductors. As seen in Fig 1.10(a), type-I superconductors have a single critical external magnetic field, $H_c(T)$, when exposed to temperatures below the critical temperature, T_c. Type-I superconductors are in the Meissner state when the applied magnetic fields are less than H_c, and revert back to the normal or resistive state when $H_c(T)$ is exceeded.

Type-II superconductors behave a little differently when exposed to magnetic fields. Fig 1.10(b) shows that type-II superconductors have two critical fields, a lower critical field, $H_{c1}(T)$, and an upper critical field, $H_{c2}(T)$. Type-II superconductors at temperatures below T_c are in the Meissner state when the applied magnetic field is below $H_{c1}(T)$ and in the normal state when the applied magnetic field strength exceeds $H_{c2}(T)$, similar to type-I superconductors. When the magnetic field is between H_{c1} and H_{c2}, type-II superconductors are in what is called the mixed state.[1,3,4]

The mixed state occurs when regions of superconductivity coexist with the normal material. Fig 1.11 illustrates the magnetic flux penetration into an ideal type-II

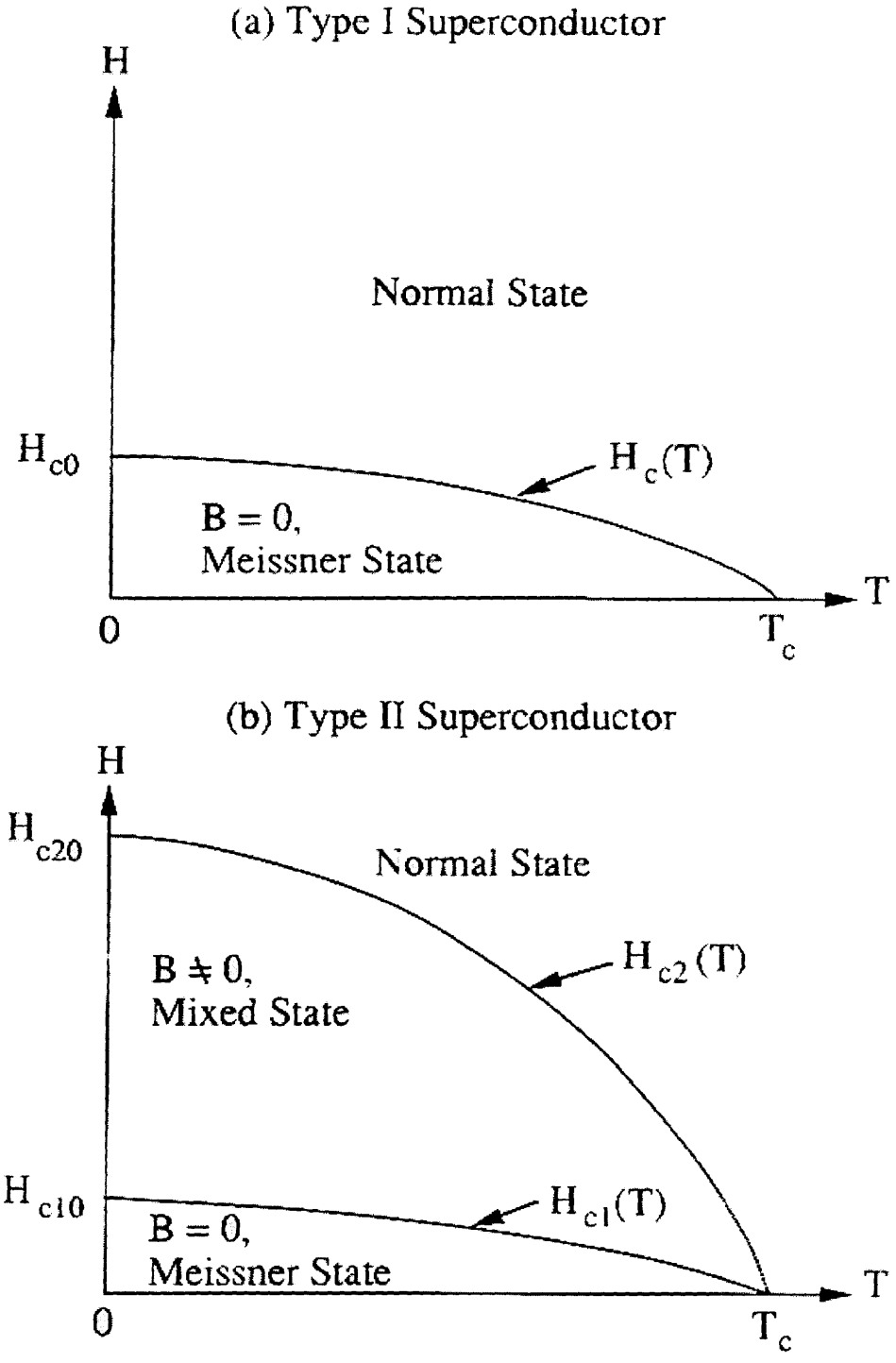

Figure 1.10 H-T phase diagrams of a) type-I superconductor and b) type-II superconductor illustrating the different states.[4]

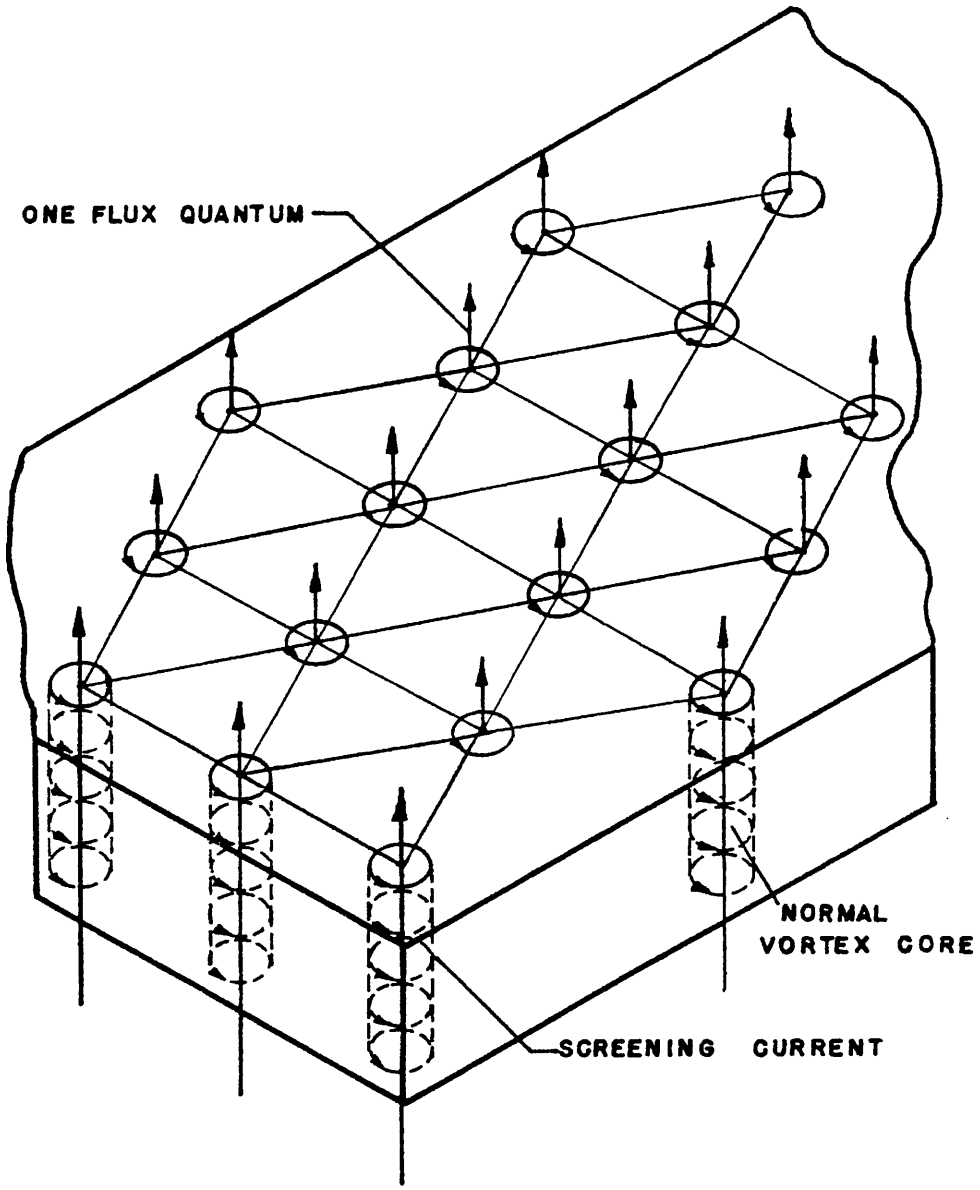

Figure 1.11 Flux penetration into an ideal type-II superconductor showing the individual normal vortices surrounded by the induced screening currents. A triangular lattice is formed to minimize the energy.[3]

superconductor in the mixed state. As the magnetic field is increased from zero to a value below $H_{c1}(T)$, the current and flux remain at the surface within the London penetration depth. When the magnetic field strength is increased above $H_{c1}(T)$ and below $H_{c2}(T)$, the flux enters the superconductor as quantized flux tubes or vortices with normal cores arranged in a regular array of triangles. The magnetic flux induces screening currents that circulate about each flux quantum. These screening currents oppose the external magnetic field and maintain the diamagnetic property of the superconductor. As the magnetic field increases, the vortices are packed in tighter and tighter until H_{c2} is reached and the normal cores of the vortices begin to overlap. Above H_{c2}, the superconductivity of the material is destroyed.[1,3,4]

In general, the critical fields for type-I superconductors and the lower critical field for type-II superconductors are on the order of a few hundred Gauss while the upper critical field is on the order of 10 T. Since type-II superconductors exhibit superconducting properties over such a large range of magnetic fields, they are the superconducting materials of technological importance. However, in an ideal type-II superconductor, there are no lattice defects or atom impurities and the flux vortices tend to be moved by the Lorentz force when the material is conducting current. The movement of the vortices causes an electric resistance called flux flow resistance and is proportional to the normal state resistance of the superconductor. The interaction between the current and the flux

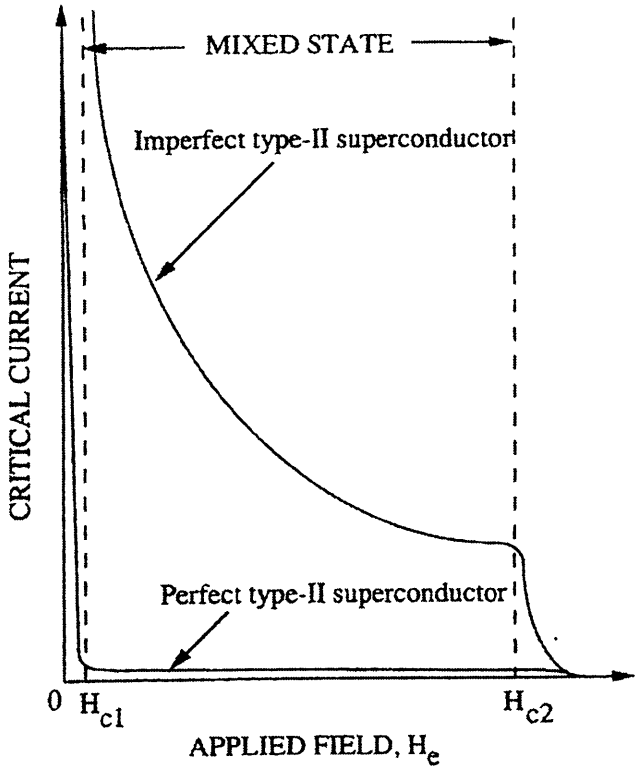

Figure 1.12 Difference between the critical currents of a highly perfect type-II superconductor and an imperfect type-II superconductor.[4]

flow resistance results in energy dissipation. Fortunately, there are no ideal superconductors and the movement of the vortices can be stopped by introducing imperfections and impurities into the conductor. Fig 1.12 shows the improvement to the critical current of an imperfect type-II superconductor compared to the critical current of a perfect type-II superconductor. Table 1.1 lists some type-I and type-II superconductors and also shows typical values for them.[1,3]

Table 1.1 Typical examples of type-I and type-II superconductors and their critical properties.[1,5]

Type-I Superconductors		
Material	T_c (K)	$\mu_0 H_c$ (T)
Al	1.2	9.93×10^{-3}
Hg	4.2	4.13×10^{-2}
Pb	7.2	8.03×10^{-2}

Type-II Superconductors			
Material	T_c (K)	$\mu_0 H_c$ (T)	J_c (A/mm^2)
NbTi	10	15	~ 650 – 700 @ 8 T, 4.2 K
Nb_3Sn	18	23	~ 1000 @ 12 T, 4.2 K

1.5 High Temperature Superconductors

1.5.1 Introduction

Materials with the highest transition temperatures are commonly called high temperature superconductors (HTS) or oxide superconductors. Since the discovery of superconductors and up to 1980, the discovery of materials with critical temperatures from 10 K to 20 K progressed in small steps over a course of decades. Then in 1987, a giant step was taken. The discovery of superconductivity at temperatures above 90 K! Fig 1.13 contains a plot of transition temperature versus time and shows the remarkable change in the field over a very short period of time.

HTS materials are conveniently divided into three classes. These classes are Class 0, Class 1, and Class 2 materials. Class 0 compounds do not possess remarkably high transition temperatures, usually around 13 K, and have relatively low

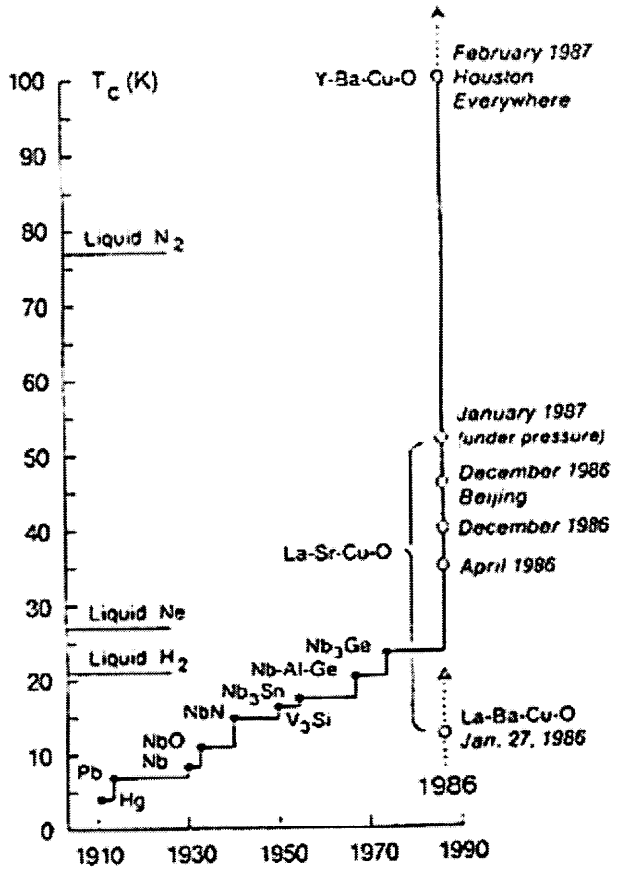

Figure 1.13 Evolution of the critical temperature up until the first discovery of high temperature superconductivity.[19]

concentrations of super electrons. An example of a Class O compound is $LiTi_2O_4$. Class 1 materials are those related to La-Ba-Cu-O. This material and other related compounds with the same crystal structure have transition temperatures that do not exceed 40 K. Class 2 materials have the highest transition temperatures. Y-Ba-Cu-O, the first superconductor with transition temperature above liquid nitrogen temperatures, remains in the superconducting state at temperatures up to 90 K. One of the most popular Class 2 superconductor is $Bi_2Sr_2Ca_2Cu_3O_{10}$ in a silver matrix (BSCCO-2223/Ag).[19] All calculations and experiments discussed in this thesis are performed for BSCCO-2223/Ag

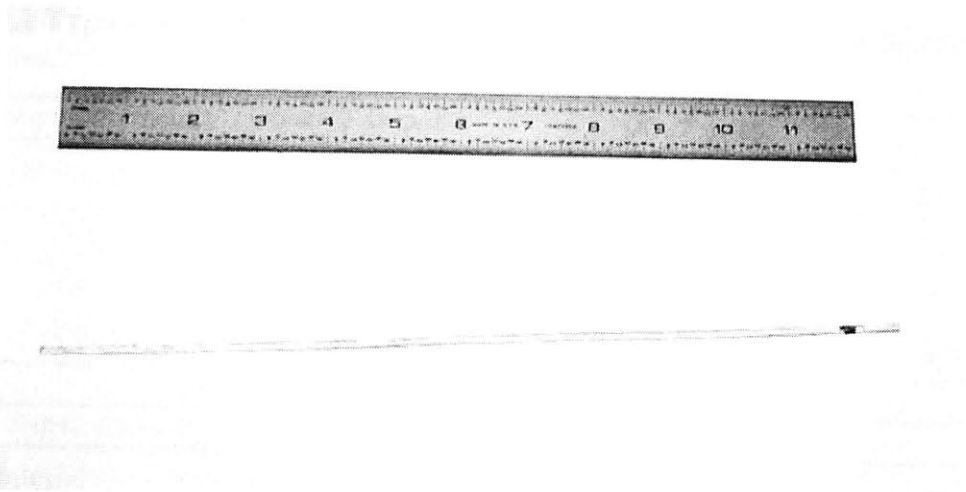

Figure 1.14 Short length of Ba2Sr2Ca2Cu3O10 superconductor in a silver matrix.

superconductor. Fig 1.14 shows a typical BSCCO-2223/Ag tape with a typical cross-section dimensions of 3.5 mm wide and 0.3 mm thick.

1.5.2 Crystal Structure Effects on Superconductivity

Since the relatively recent discovery of HTS, there have been two kinds of theoretical suggestions concerning the origin of the superconductivity. These two ideas initiated the exploration of whether the superconductivity at such high temperatures arises from the electron-phonon interactions as it does in low temperature superconductors or from the exchange of other bosonic excitations such as paramagnons, excitons, or plasmons. The topic is beyond the scope of this thesis, however, a brief summary is presented to give the reader a better understanding of the operation of superconductors. The relevant crystal structure characteristic of a Class 2 oxide is shown in Fig 1.15. The diagram illustrates a feature that is common to all HTS materials, a two-dimensional copper-oxygen plane that

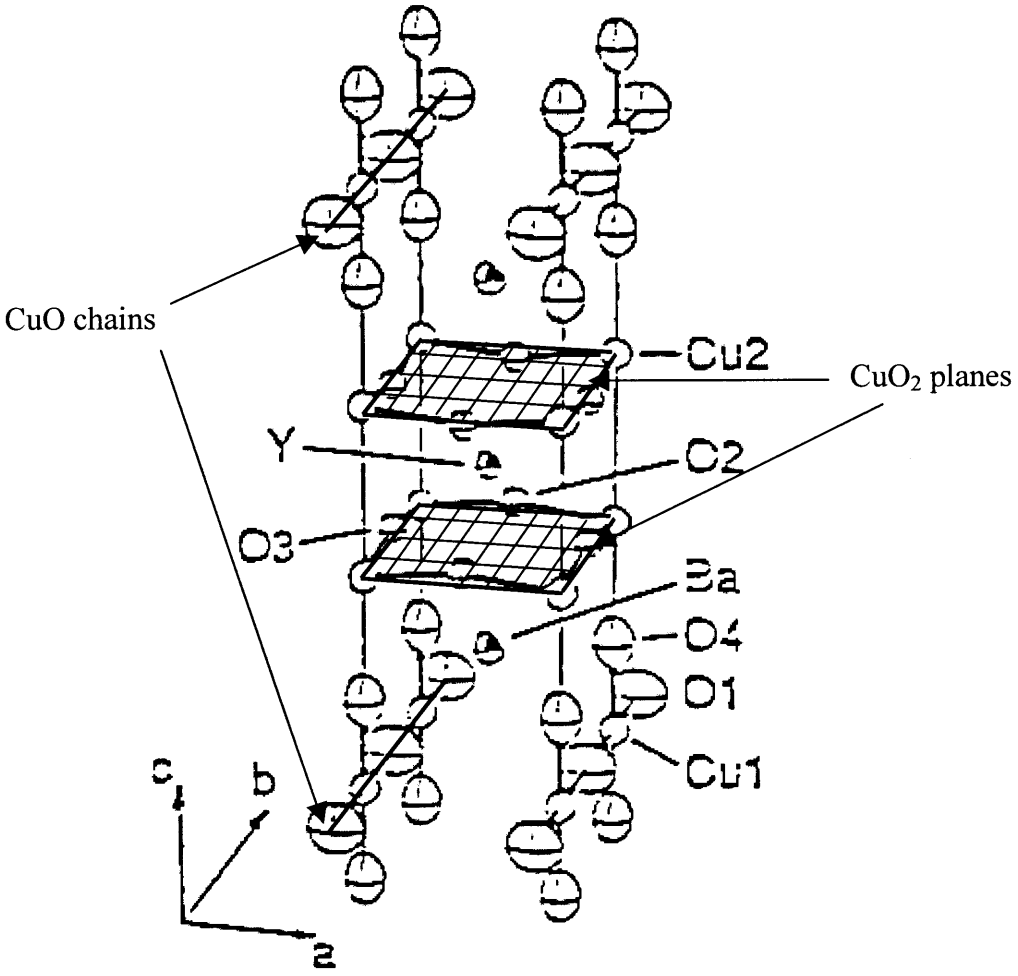

Figure 1.15 Crystal structure of a Class 2 oxide superconductor.[19]

is believed to be the main contributor to the conduction process. The crystal lattice is composed of two different types of layers loosely designated as chains and planes. The chains are made up of CuO and the planes are CuO_2. The planes of CuO_2 define the coordinate system used to describe HTS materials. The a- and b-axis are parallel to the CuO_2 plane while the c-axis is perpendicular to the CuO_2 plane. This crystal structure also leads to anisotropy effects. The resistivity in the direction perpendicular to the planes is usually an order of magnitude greater than the resistivity in the directions

parallel to the planes. Fig 1.16 shows how the resistivities differ with respect to temperature. This anisotropy is also demonstrated in the superconducting state. The critical currents are up to three times greater when exposed to magnetic fields that are perpendicular to the c-axis than when exposed to magnetic fields parallel to the c-axis.[17]

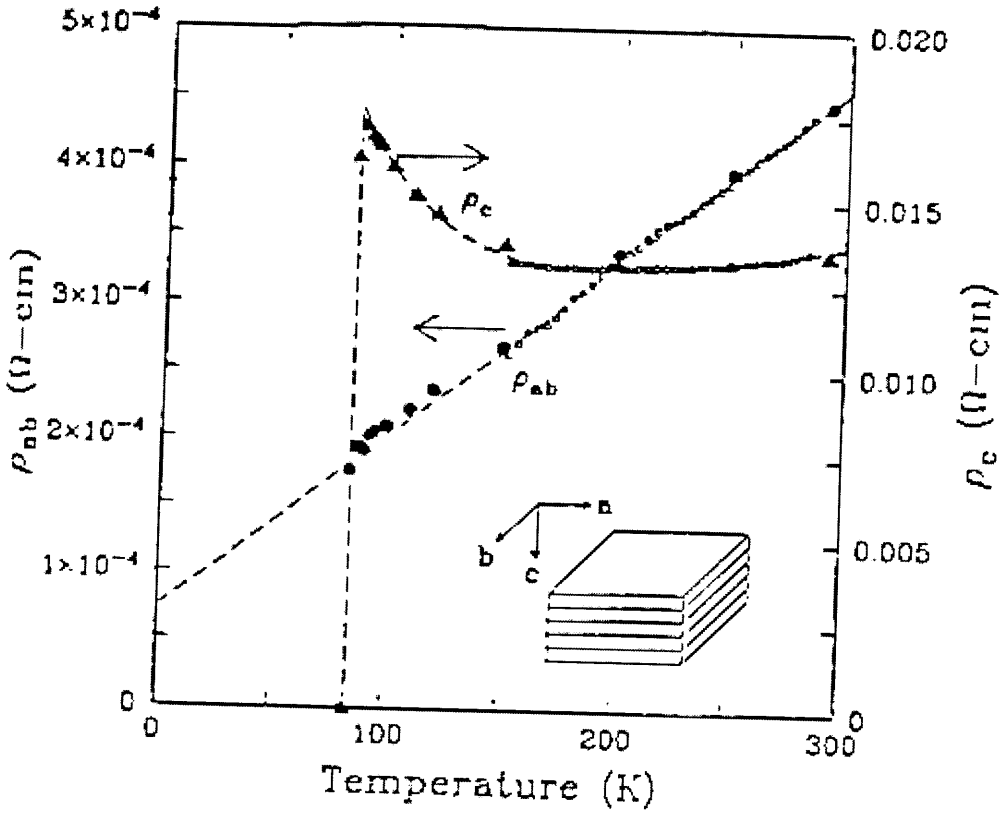

Figure 1.16 Resistivity tensor components perpendicular (ρ_{ab}) and parallel to the c-axis (ρ_c). The inset schematically illustrates the crystal directions with respect to the Cu-O planes, which dominate the conductivity.[19]

1.6 Introduction to AC Losses

A basic property of superconductors is the ability to carry a DC transport current with no resistance. Superconductors are subject to energy dissipation when exposed to an AC magnetic field, carry an AC current, or both. These losses are collectively known as AC losses and have a significant effect on the economics and operation of a superconducting system. The energy dissipation increases the temperature of the sample and causes two major effects. Local heating of the superconductor causes a reduction of the critical properties and can initiate an unwanted quench event. Also, the heat is an undesired load on the cryogenic system and has a major impact on the efficiency of the refrigeration system.[1,3]

This thesis concentrates on AC losses produced in BSSCO-2223/Ag sheathed conductor when exposed to an AC magnetic field and a DC transport current. At very low frequencies, the losses in the conductor are mostly hysteresis losses and these are the only losses investigated in this paper. A brief mention of other types of AC losses follows while the rest of the thesis contains a more complete explanation of hysteresis loss.

The most fundamental loss mode of type-II superconductors is hysteresis loss. Hysteresis loss occurs when the superconductor is in the mixed state and results from the irreversible magnetic flux motion driven by the changing field. The trapped flux leaves the conductor magnetized. The hysteresis loss is proportional to the magnetization. Methods to calculate the hysteresis loss are shown in Chapter 2. The models show that the hysteresis loss is directly proportional to the size of the superconducting filament. The

reduction of hysteresis loss is the main reason why very small filaments are used to manufacture superconductors.[1,3,15]

Superconducting filaments in a single strand are stabilized using a non-superconducting matrix, which gives the filaments the ability to withstand transient energy disturbances that could destroy the superconducting state. Usually, the matrix is a material with a high electrical conductivity. When the strand is subject to a time varying magnetic field, an electric field is produced in the matrix and drives closed loops of currents between the superconducting filaments. These currents are known as eddy currents. Since these current loops pass through the resistive matrix, energy is dissipated directly in the conductor. This loss is known as coupling current loss because of the effective coupling interaction between separate filaments. Long, untwisted filaments result in a large inductance, which leads to large coupling currents that decay with a long time constant and dissipate significant energy. The filaments are usually twisted to reduce this flux linkage. Twisting the filaments causes a reversal of the electric field every half twist and reduces the coupling losses significantly.[1,3,6,15]

1.7 Scope of Thesis

Hysteresis losses in HTS materials have a significant effect on the economics and design of any apparatus to be used in any power application. A majority of the previous work done for measuring the AC losses in high temperature superconductors has been done for low field power applications at 60 Hz since this is the area under most intensive development. It is the intent of this work to further contribute to measuring AC losses

and critical current densities in HTS materials at various temperatures under conditions similar to those found in fusion applications. In fusion magnet systems, AC losses usually occur under conditions of much larger field swings and at lower frequencies than those for electric power applications.

Suggestions for use of HTS materials in fusion devices are current leads and poloidal coils that are subjected to low frequency, high strength magnetic fields. However, current HTS materials available are not very uniform over long lengths of conductor. The current densities vary from section to section and the conductor is limited by the worst condition of the sample material.

This thesis concentrates on the development of an AC loss measurement device for short sample tests of high temperature superconductors with AC magnetic fields and AC/DC transport currents at low frequencies and various temperatures. The analysis of the data is based on existing models of AC losses in superconductors.

2 Theory of Superconductors

Superconductors have already proven useful in many applications and have expanded areas of research into regimes which were previously unobtainable. However, before superconductors can achieve their full potential, much advancement must still be made. This chapter presents a short discussion of selected models on superconductivity and methods for the quantitative analysis of superconductors. The theory and formulae presented in this chapter are the basis for this experiment and are used to obtain all theoretically calculated values. This thesis is primarily concerned with situations in which the magnetic field is in plane with the broad face of the tape and perpendicular to the current flow. Therefore, the following sections in this chapter are discussed in this context.

2.1 Critical Current

2.1.1 Introduction

It was discovered early that there is a maximum amount of current that can be carried along a superconductor if it is to remain resistanceless. This limit is called the critical current. In general, there are two contributions to the current flowing in a superconductor. These currents are called the transport current, I_T, and the screening current. Transport currents are currents supplied from some external source such as a battery or power supply. They are called transport currents because charge is effectively "transported" into and out of the superconductor. If the superconductor is exposed to an external magnetic field, screening currents are induced and circulate on the surface of the

conductor so as to cancel the flux inside. The transport current also creates a "self-field" which itself induces a screening current. These screening currents are superimposed on the transport current. The current density J, which is current per unit cross sectional area of superconductor, can be considered to be the sum of a component J_T due to the transport current and a component of J_H due to the screening currents and is expressed in the following relationship: [1]

$$J = J_T + J_H \tag{2.1}$$

It may be expected that the superconductivity will break down if the magnitude of the total current density J at any point exceeds the critical current density J_c.[1,3]

In early work on superconductors by London [18], it was shown that there is a relationship between the total super current density at any point and the magnetic flux density at that point. Hence, when a current flows in a superconductor, there will be a flux density, B, and a corresponding field strength, $H = \frac{B}{\mu_0}$, at the surface which is related to the surface current density, J. For a type-I superconductor, as the total current flowing on the superconductor surface increases, the current density at the surface approaches the critical value J_c and the associated magnetic field strength at the surface follows and approaches its critical value H_c. Conversely, a magnetic field of strength H_c at the surface is always associated with a surface current density at J_c. Therefore, a superconductor loses its zero resistance when the total magnetic field strength, due to the transport current and applied magnetic field, exceeds the critical field strength H_c. The maximum amount of transport current that can be carried without exceeding the critical field strength at the surface is called the critical current. Clearly, stronger applied

magnetic fields lead to lower critical current densities. Since the H_c for type I superconductors is very small, small applied magnetic fields decrease the ability to carry J_T. Thus, these materials are not useful for applications.[1,3]

Critical current density is more complicated in type-II superconductors, however, because the state of the conductor changes at two field strengths, H_{c1} and H_{c2}, instead of only one, H_c. Since type-II superconductors are completely in the superconducting state and behave as type-I superconductors below fields of strength H_{c1}, it is logical to extend the previous statement about type-I superconductors and critical current; i.e. the material will be resistanceless as long as the magnetic field strength generated by the transport current and the applied magnetic field at the surface is below the lower critical value H_{c1}. However, this has only been observed in the case of extremely perfect samples. Most samples are not extremely perfect and this actually improves the critical currents above and below H_{c1}. In fact, it has been shown that the critical current is almost completely controlled by the imperfection, the amount of chemical impurities and physical deformities, of the material when the superconductor is in the mixed state. The disparity between critical currents in the mixed state for perfect type-II superconductors and imperfect type-II superconductors is quite large. The self-field critical current density of a highly imperfect superconductor is on the order of 10^3 A/mm^2 while the self-field critical current density of a highly perfect superconductor is usually around 10^{-6} A/mm^2.[1,3]

2.1.2 Flux Flow Resistance

Flux flow resistance is an experimentally observed property of type-II superconductors that are subjected to an external magnetic field that lies somewhere between the upper and lower critical fields. A transport current is applied and the voltage across the superconductor is monitored as the current is increased. As long as the current stays below the critical value, no voltage is recorded. When the current is increased above the critical value, a voltage appears and approaches a linear increase with increasing current. This voltage is also far less than the voltage which would be observed if the conductor were in the normal state. Fig 2.1 shows the voltage-current characteristics of three wires of the same type-II superconductor that only vary in degrees of perfection measured at the same strength of applied magnetic field. The critical current of each sample is different as expected, but the slope of the characteristic is the same for all three specimens. Therefore, the rate at which voltage appears when the critical current is exceeded is an innate characteristic of the particular material while the critical current is dependent on the degree of perfection of the material.[1,3]

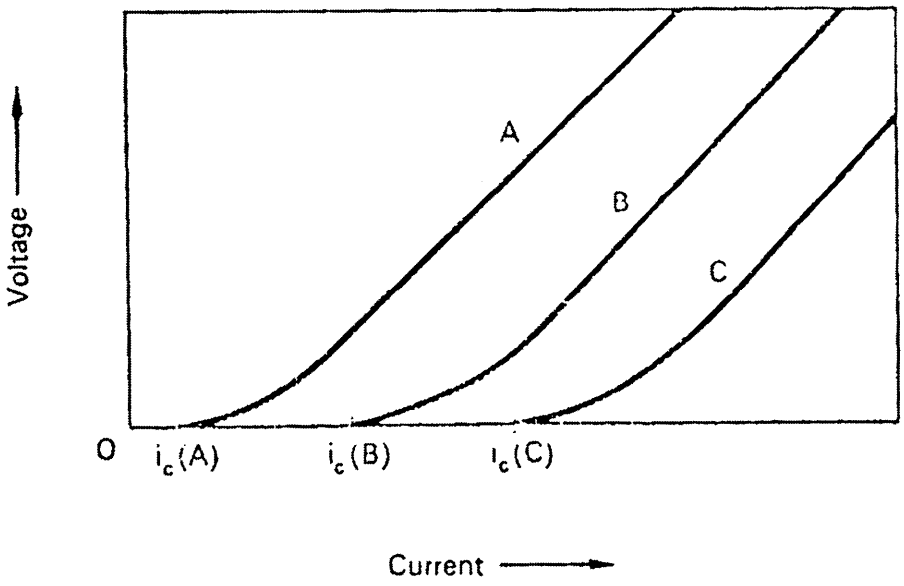

Figure 2.1 Voltage-current characteristics of three wires of the same type-II superconductor with varying degrees of purity in the same transverse applied magnetic field.[1]

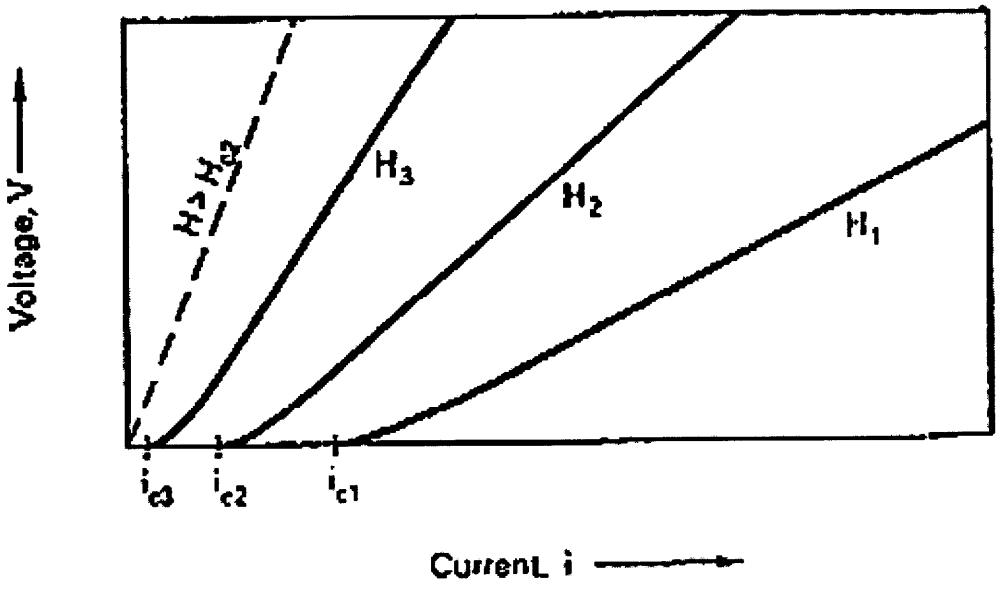

Figure 2.2 Effect of the applied magnetic field strength on the V-I characteristic of a type-II superconductor in the mixed state. $H_1 < H_2 < H_3 < H_{c2}$.[1]

The value of the slope $\frac{dV}{dI}$ which the characteristic approaches at currents well above I_c is known as flux flow resistance R' of the specimen. The flux flow resistivity ρ' of the material is defined by the following formula:[1]

$$R' = \frac{\rho' l}{A} \tag{2.2}$$

where l is the length of the specimen and A is the cross sectional area of the specimen. For a given strength of magnetic field, the flux flow resistivity is proportional to the resistivity of the material in the normal state and approaches this value as the magnetic field strength is increased to H_{c2} as seen in Fig 2.2.[1]

2.1.3 Impact of Flux Flow on Critical Current

The phenomena of flux motion and flux flow resistivity are the basic mechanisms which determine the magnitude of the critical current of a type-II superconductor operating in the mixed state and are the source of voltage that appears at currents greater than the critical current. Consider the case of a type-II superconductor, which is exposed to an applied magnetic field and operating in the mixed state, carrying a transport current as shown in Fig 2.3. Since it is in the mixed state, the superconductor will be threaded by the magnetic flux associated with the normal cores. The interaction between the flux and the transport current creates a Lorentz force on each flux vortex in the following form[3]

$$F = J \times \phi_0 \tag{2.3}$$

where F is the force per unit length on the flux vortex, J is the transport current and ϕ_0 is the quantum of flux in the vortex. In the special case where the magnetic field is perpendicular to the current, the force is just[1,3]

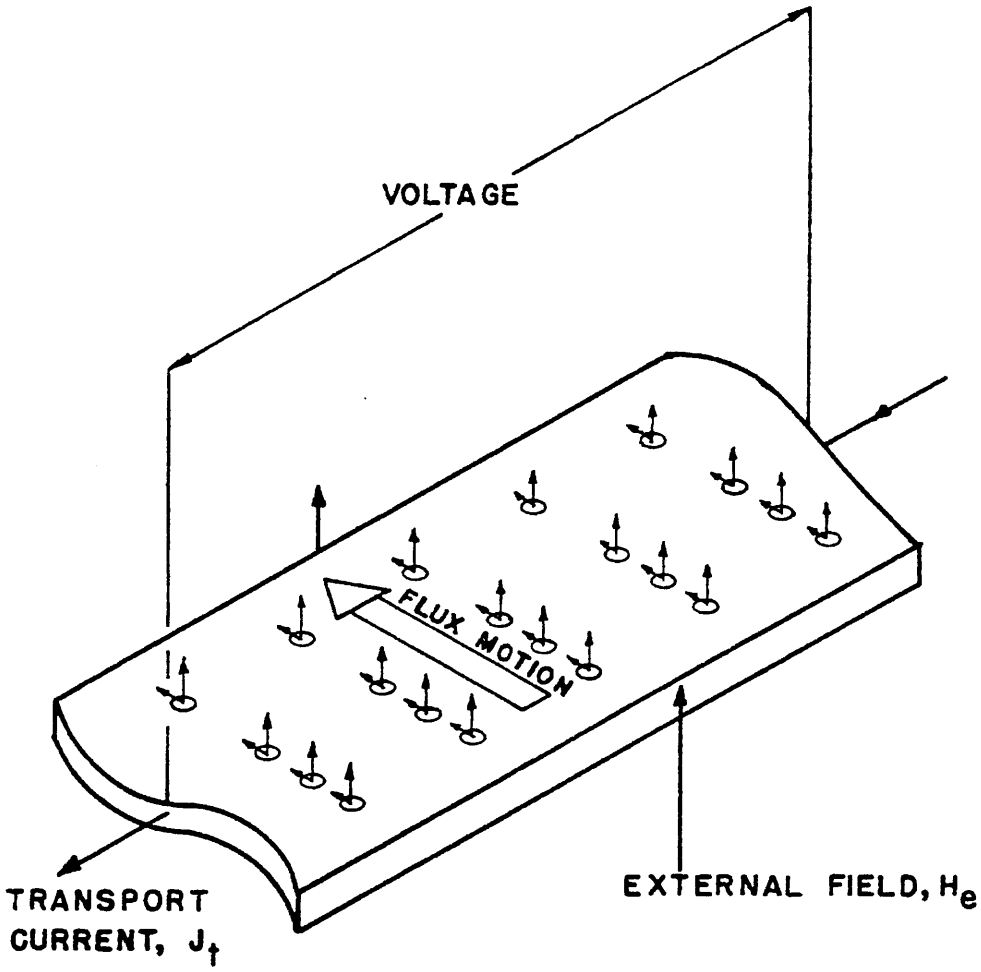

Figure 2.3 Ideal type-II superconductor in a uniform external magnetic field carrying a transport current.[3]

$$F = J\phi_0 \tag{2.4}$$

In an ideal type-II superconductor, there is no pinning force to balance the Lorentz force and the flux vortices are free to move across the conductor. The moving flux induces an electric field given by[1,3]

$$E = v_L \times B = v_L \times n\phi_0 \tag{2.5}$$

where v_L is the velocity of flux lines and n is the number of flux lines per unit area such that $B = n\phi_0$.

Since there is no apparent resistance to flux flow, the acceleration of the vortices and subsequent increase of electric field with time is a logical extension. However, the observed voltage indicates that the electric field is constant with time. Therefore, a drag force must exist to balance the Lorentz force. The corresponding force balance between the Lorentz force and the drag force is

$$F = \eta v_L = J \times \phi_0 \tag{2.6}$$

where η is a viscous damping constant. The damping force is dissipative and requires a power input $P = E \cdot J$ which is only available from the transport current power source. Combining Eq (2.5) and Eq (2.6), the flux flow resistivity is given by the following expression[1,3]

$$\rho' = \frac{E}{J} = \frac{B\phi_0}{\eta} \tag{2.7}$$

Experimental measurements of ρ' show that it is a function of temperature, and as T goes to zero, the flux flow resistivity is well-correlated by[1,3]

$$\rho' = \rho_n \frac{H}{H_{c2}} \tag{2.8}$$

where ρ_n is the resistivity of the normal material and $\frac{H}{H_{c2}}$ is the fraction of the normal core area. This result is very interesting because it implies that the dissipation is due to the transport current flowing through the normal cores of the moving flux vortices.

The flux flow resistivity is the basic dissipative mechanism that is responsible for the AC loss. However, the dissipation only occurs when the vortices are set in motion. Now that the dissipative mechanism is discovered and quantified, the behavior of type II superconductors can be explained. For example, the low values of critical current for ideal type II superconductors arise from the absence of pinning sites to restrain the flux motion. Since the vortices are unimpeded, the energy dissipation increases as the square of the current and excessively heats the sample above T_c, which destroys the superconductivity.[1,3]

Non-ideal superconductors contain atom impurities, crystal defects, and grain boundaries that act as pinning sites. While not all vortices are pinned, the mutual repulsion between the cores creates a rigid structure when only a few are pinned and prevents the vortices from moving. As the critical current increases to high values, the Lorentz force increases until it eventually exceeds the pinning force, the vortices begin to move, and, hence, the critical current is reached. An increase of imperfections or pinning sites increases the average pinning force per normal core and increases the critical current. Critical currents

are determined experimentally as the current associated with an electric field criterion of either 10 μV/m or 100 μV/m, depending on the application.[1,3]

2.1.4 Critical State Model

The critical state model applies to type-II superconductors in the mixed state and is the state where the Lorentz force is exactly equal to the pinning force. This is expressed by the following equation

$$F_p = J_c \phi_0 \tag{2.9}$$

where J_c is the critical current density. As before, flux flow and dissipation occur when the current is raised above the critical current. Kim, et al., [27] proposed a force balance between the drag or viscous force, the Lorentz force, and the pinning force in the following equation

$$\eta v_L = F_L - F_P = \phi_0 (J - J_c) \tag{2.10}$$

The induced electric field is of the same form as Eq (2.5). Therefore, combining Eq (2.5), Eq (2.7), Eq (2.8), and Eq (2.10), the electric field can be written as

$$E = \rho_n \frac{H}{H_{c2}} (J - J_c) \tag{2.11}$$

This equation is very useful for computing the energy loss of a superconducting filament carrying a transport current. The effect of H in Eq (2.11) is shown in Fig 2.2.[3]

It is not necessary to determine the flux flow resistivity explicitly in order to calculate the loss. The critical state model provides a convenient description of the hysteresis loss as a succession of quasi-static time steps between equilibrium distributions of magnetic field

and current within the specimen. Therefore, it is sufficient to compute the electric field, E and the current distribution, J, from the quasi-static Maxwell equations

$$\nabla \times H = J \tag{2.12}$$

and

$$\nabla \times E = -\frac{\partial B}{\partial t} \tag{2.13}$$

Use of these equations is valid as long as $\frac{\partial B}{\partial t} << \frac{B_P}{\tau_m}$ where B_p is the magnetic field required to fully penetrate the filament and τ_m is the time constant for magnetic flux to diffuse through the filament. For typical type-II superconductors, this condition should hold as long as the frequency of the changing magnetic field does not approach the gigahertz range.[3]

2.2 AC Losses

2.2.1 Introduction

This section deals with the macroscopic description of AC losses in superconductors and outlines the mathematical model from which the losses can be quantitatively computed. Before the model is presented, it is important to understand the conditions under which the superconductor is operated and how these conditions relate to the model. It is also important to acknowledge the underlying assumptions of the model. The type of superconductor, filament distribution, matrix material, conditions of magnetic field and transport current and their respective time dependence are all factors that determine the amount of loss that occur in a superconductor.

The multifilament composite conductor exhibits two independent loss mechanisms under the influence of a changing magnetic field. These loss mechanisms are coupling currents through the normal matrix material and hysteresis loss in the individual superconducting filaments. The relative contribution of these loss mechanisms depends on a variety of factors. These factors are listed as follows:[3]

1) Frequency of the alternating current or magnetic field,
2) Amplitude of the magnetic field change,
3) Amplitude of the transport current,
4) Current ramp rate,
5) Magnitude of background field,
6) Field orientation with respect to the conductor,
7) Conductor properties:
    a) Filament twist pitch
    b) Filament size
    c) Matrix to superconductor ratio
    d) Conductivity and permeability perpendicular to filaments
    e) Conductivity and permeability parallel to filaments

The following sections are intended to develop an understanding of the loss mechanisms within the bulk superconductor carrying a DC transport current in a changing external magnetic field. The mathematical treatment is based upon the macroscopic currents, magnetic fields, and electric fields, but the models are consistent with the microscopic phenomena discussed earlier.

2.2.2 Hysteresis Loss in One-Dimensional Slab

A one-dimensional slab of non-ideal type-II superconductor is often used as a simple example to illustrate the fundamentals of the critical state model. It is also directly applicable to the conditions set up by this experiment. Consider a slab as shown in Fig 2.4 to be of thickness 2a and infinite in length and exposed to a uniformly distributed

alternating external magnetic field, H_e, oriented parallel to the sides of the slab. The magnitude of the magnetic field is such that the superconductor is in the mixed state. The flux will penetrate the material to the point where the pinning force equals the Lorentz force of the flux bundles. Therefore, the condition is the critical state and the induced current density is at the critical value and can be solved by Eq (2.12) and Eq (2.13) with the boundary current $H = H_e$ at the surface. The exact form of the solution depends on the assumptions made to the critical current density, J_c. The Bean [29] model considers the critical current to be independent of the magnetic field while the Kim [28] model considers the critical current to be inversely proportional to the magnetic field.

2.2.2.1 Bean Model

If the critical current is assumed constant as according to the Bean Model, the solution to Eq (2.12) is of the form

$$H = H_e + J_c(x - a) \qquad x > 0 \tag{2.14}$$

Fig 2.5 shows the magnetic field and current distributions inside the superconductor that are consistent with the Bean model at selected steps as the magnetic field is swept over a complete cycle beginning with the virgin state. The field penetrates the slab to a point x_p proportional to the strength of the external magnetic field given by[3,15]

$$x_p = a - \frac{H_e}{J_c} \tag{2.15}$$

The slab is said to be fully penetrated when the external field, H_e, is equal to the penetration field, H_p. Therefore, Hp is defined as[3,15]

$$H_p = J_c a \tag{2.16}$$

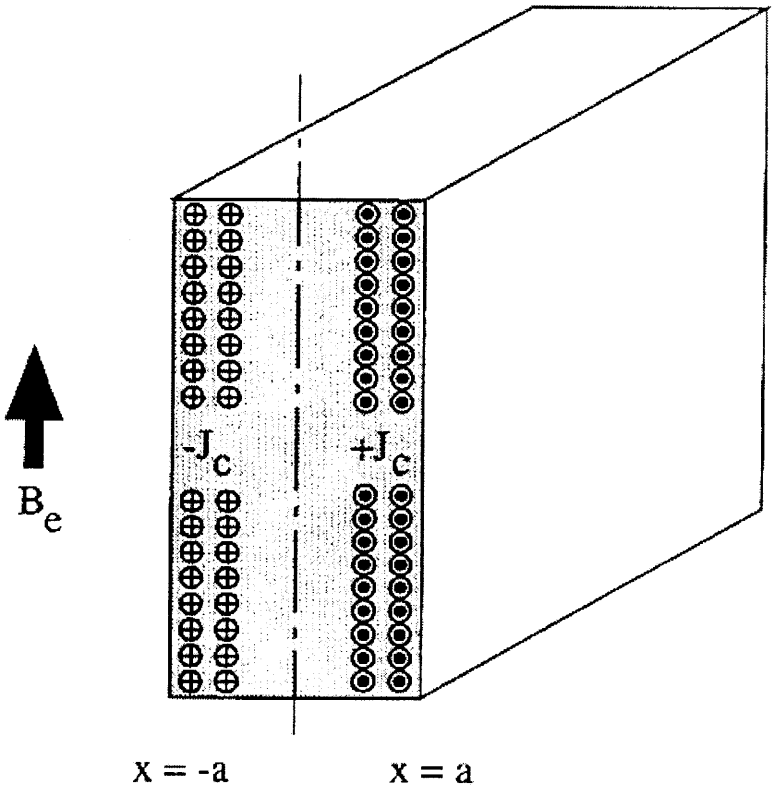

Figure 2.4 Type-II superconductor in an externally applied magnetic field showing the induced screening current pattern.[4]

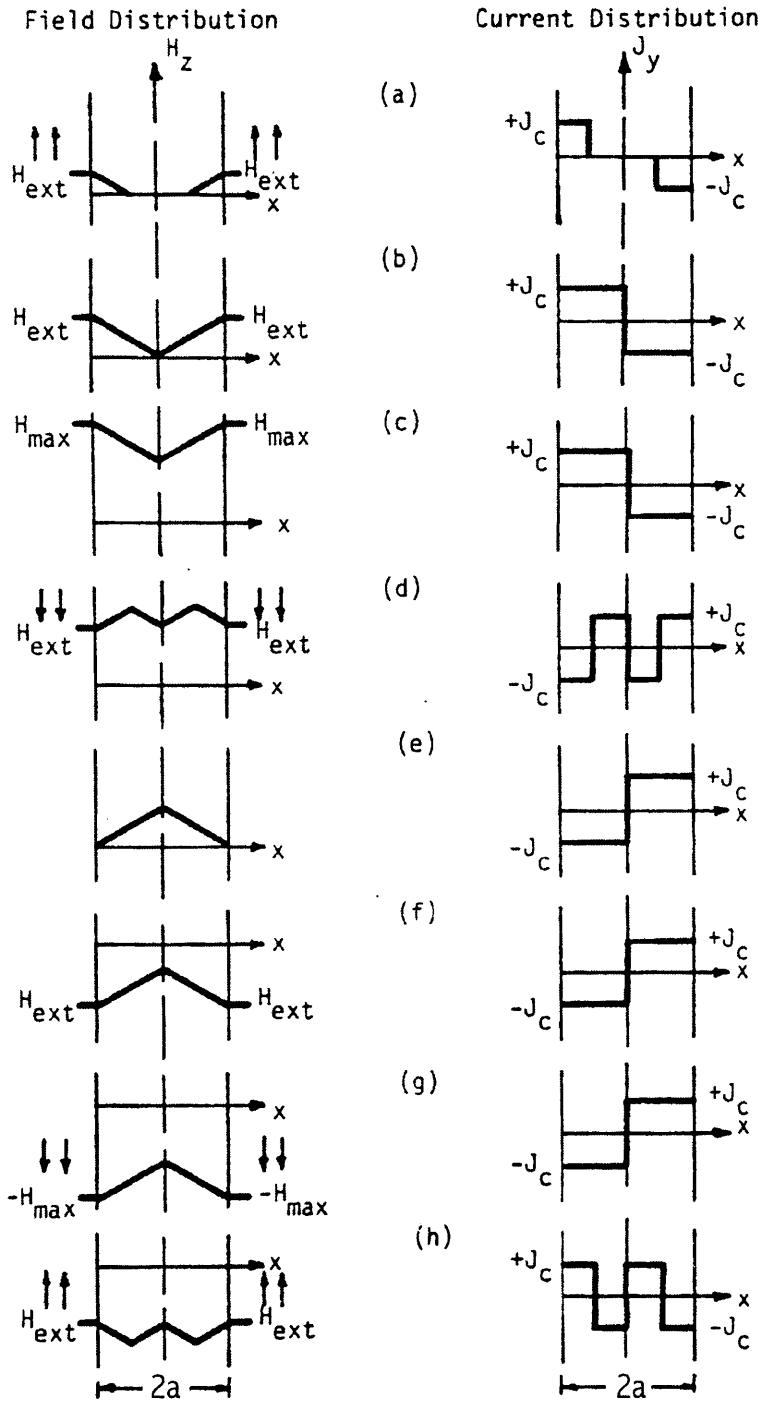

Figure 2.5 Current and magnetic field distributions inside a type-II superconductor in the mixed state with no transport current in an alternating magnetic field.[3]

As the magnetic field is reduced from its maximum value to zero, there remains some magnetic flux trapped within the slab as shown in Fig 2.5(e). This trapped flux is the hysteresis inherent in the superconductor. As the field swings around and begins to increase in Fig 2.5(h), the current flows in a direction to shield the inner regions of the superconductor to the changing magnetic field.[1,2,3,15]

The hysteresis loss can be calculated from the magnetization of the slab. The magnetization is calculated from[1,2,3,15]

$$M = H_e - \frac{1}{a}\int_0^a H dx \tag{2.17}$$

Fig 2.6 shows the magnetization curves for a full-cycle magnetic field sweep and for a half-cycle magnetic field sweep. The energy loss density per cycle is equal to the area under the magnetization curve and is given by[1,2,3,15]

$$Q_h = \oint_{cycle} \mu_0 M dH \tag{2.18}$$

When the integration is performed over the full cycle of magnetic field sweep, the results depend on the strength of the external magnetic field compared to the magnitude of the penetration field. The results are listed below[3,15]

$$Q = \frac{2}{3}\mu_0 H_p^2 \left(\frac{H_m}{H_p}\right)^3 \qquad H_m \le H_p \tag{2.19}$$

$$Q_h = \frac{2}{3}\mu_0 H_p^2 \left(\frac{H_m}{H_p}\right)\left(3 - 2\frac{H_p}{H_m}\right) \qquad H_m > H_p \tag{2.20}$$

$$Q_h = 2\mu_0 H_m H_p \qquad H_m >> H_p \tag{2.21}$$

where H_m is the maximum value of the external magnetic field.

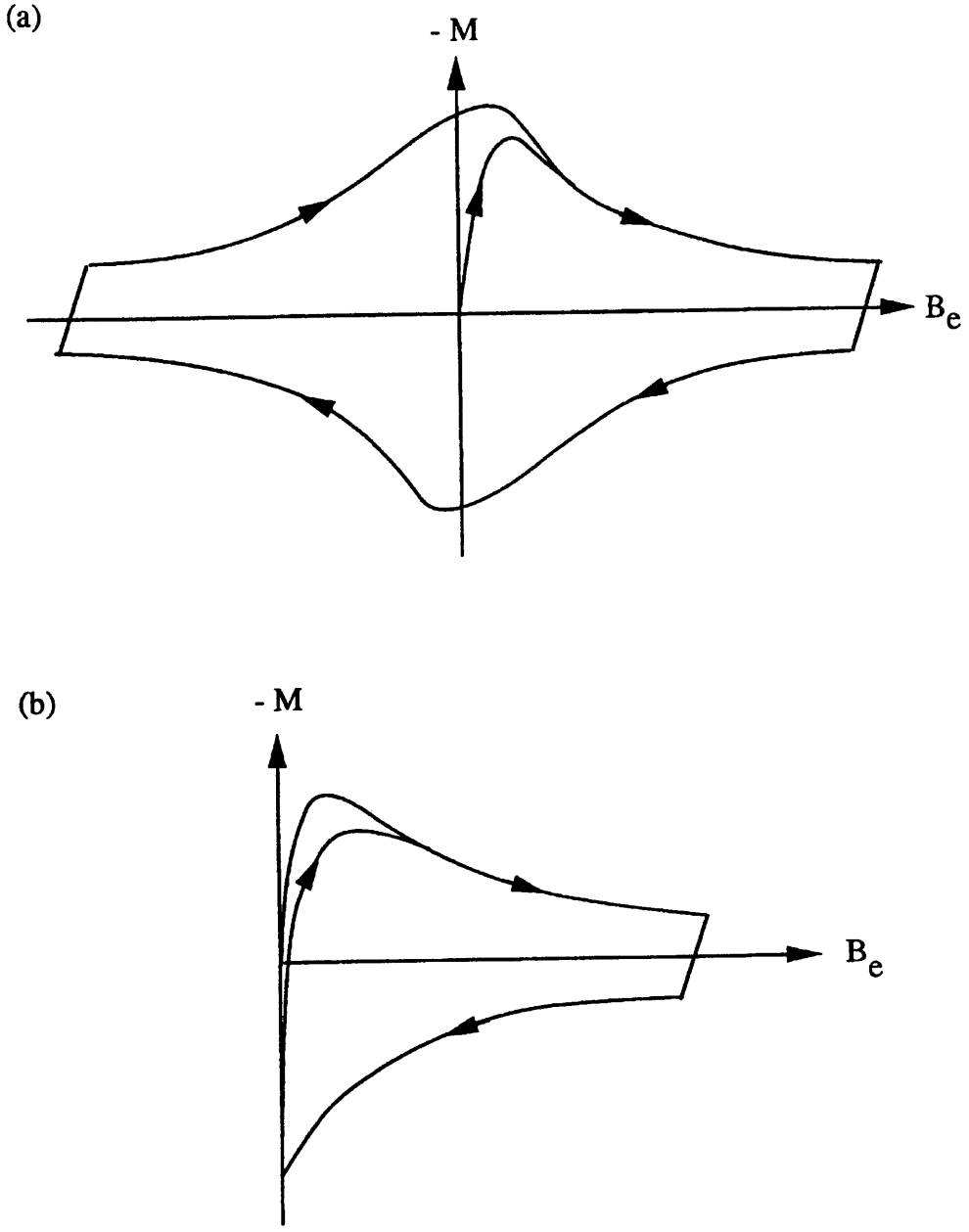

Figure 2.6 Magnetization loops for type-II superconductor for (a) full cycle magnetic field sweeps and (b) half-cycle magnetic field sweeps.[4]

2.2.2.2 Kim Model

The hysteresis loss is calculated from the Kim model by following a similar procedure as with the Bean model. Instead of assuming the critical current is constant with magnetic field, the Kim model assigns a functional dependency of the critical current density with the magnetic field given by the following expression[3,15]

$$J_c = \frac{J_0 H_0}{H + H_0} \tag{2.22}$$

where $J_0 = J_c$ at $H = 0$ and $H_0 = H_c$ at $J_c = \frac{J_0}{2}$. The field profile in the filaments calculated from Eq (2.12) becomes[3,15]

$$H = H_0 \left\{ \left[\left(1 + \frac{H_e}{H_0} \right)^2 - \frac{2J_0}{H_0} \left(x - \frac{a}{2} \right) \right]^{\frac{1}{2}} - 1 \right\} \qquad x > 0 \tag{2.23}$$

Fig 2.7 shows the field and current distributions calculated from the Kim model for various values of the external magnetic fields. The penetration depth of the magnetic field becomes

$$x_p = \frac{a}{2} - \frac{H_e}{H_0 J_0} \left(H_0 + \frac{H_e}{2} \right) \tag{2.24}$$

and full penetration occurs when $H_e = H_p$ where

$$H_P = H_0 \left(1 + \frac{J_0 a}{H_0} - a \right) \tag{2.25}$$

The hysteresis loss density per cycle calculated from Eq (2.18) when the magnetic field is cycled between H_m and $-H_m$ is[3,15]

$$Q_h = \mu_0 a J_0 H_0 \ln \left(\frac{H_0 + H_m}{H_0} \right) \tag{2.26}$$

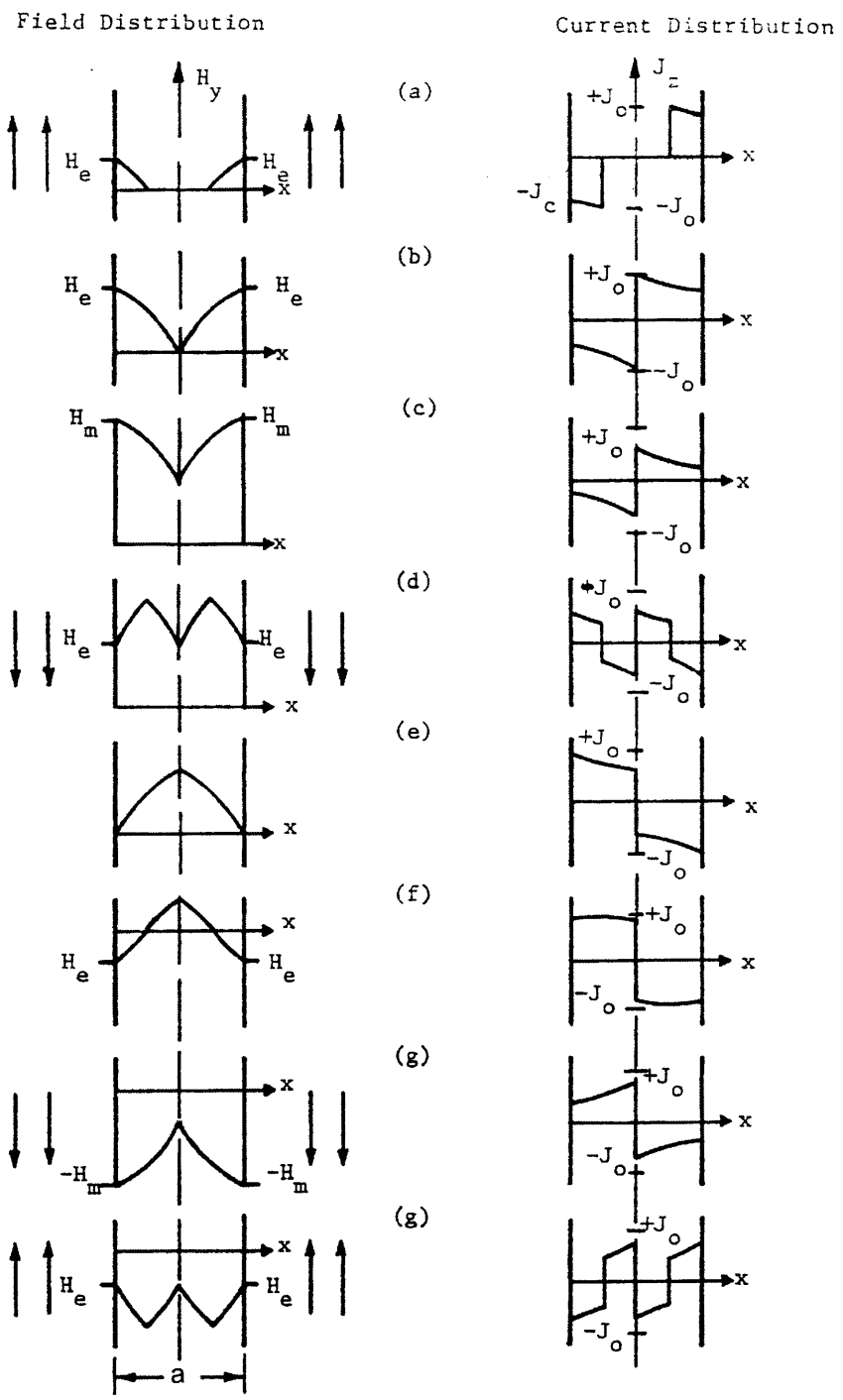

Figure 2.7 Magnetic field and current distributions in a type II superconducting slab of thickness a calculated using the Kim critical state model.[3]

2.2.3 *Effect of Transport Current on Hysteresis Loss*

The effect of transport current in the slab is modeled in a way similar to a slab with no transport current and is consistent with the critical state model. Consider a one-dimensional slab to be in a uniform external magnetic field carrying a transport current, I_t, which is smaller than the critical current, I_c. It is assumed that the transport current is maintained at a constant value by a power supply and the only the effect of the changing magnetic field is to alter the magnetization currents. The field and current distributions in the superconductor that correspond to the prescribed conditions at discrete time steps as the magnetic field is cycled through an amplitude of H_m are shown in Fig 2.8. The current flows everywhere in the cross section at the critical value and is considered constant as per the Bean model.

As the field goes through several cycles, it is apparent that the central region of the slab is occupied by the transport current and the field required to fully penetrate to the region with current is less than the field required to penetrate to the center of the slab when no transport current is present. The full penetration field depends on the size of the transport current region given by the following relationship[2]

$$H_p' = H_p(1-i) \tag{2.27}$$

where $i = \frac{I_t}{I_c}$. The magnetization determined from Eq (2.17) is given by the following equation[2,15]

$$-M' = \frac{H_p}{2}(1-i^2) \tag{2.28}.$$

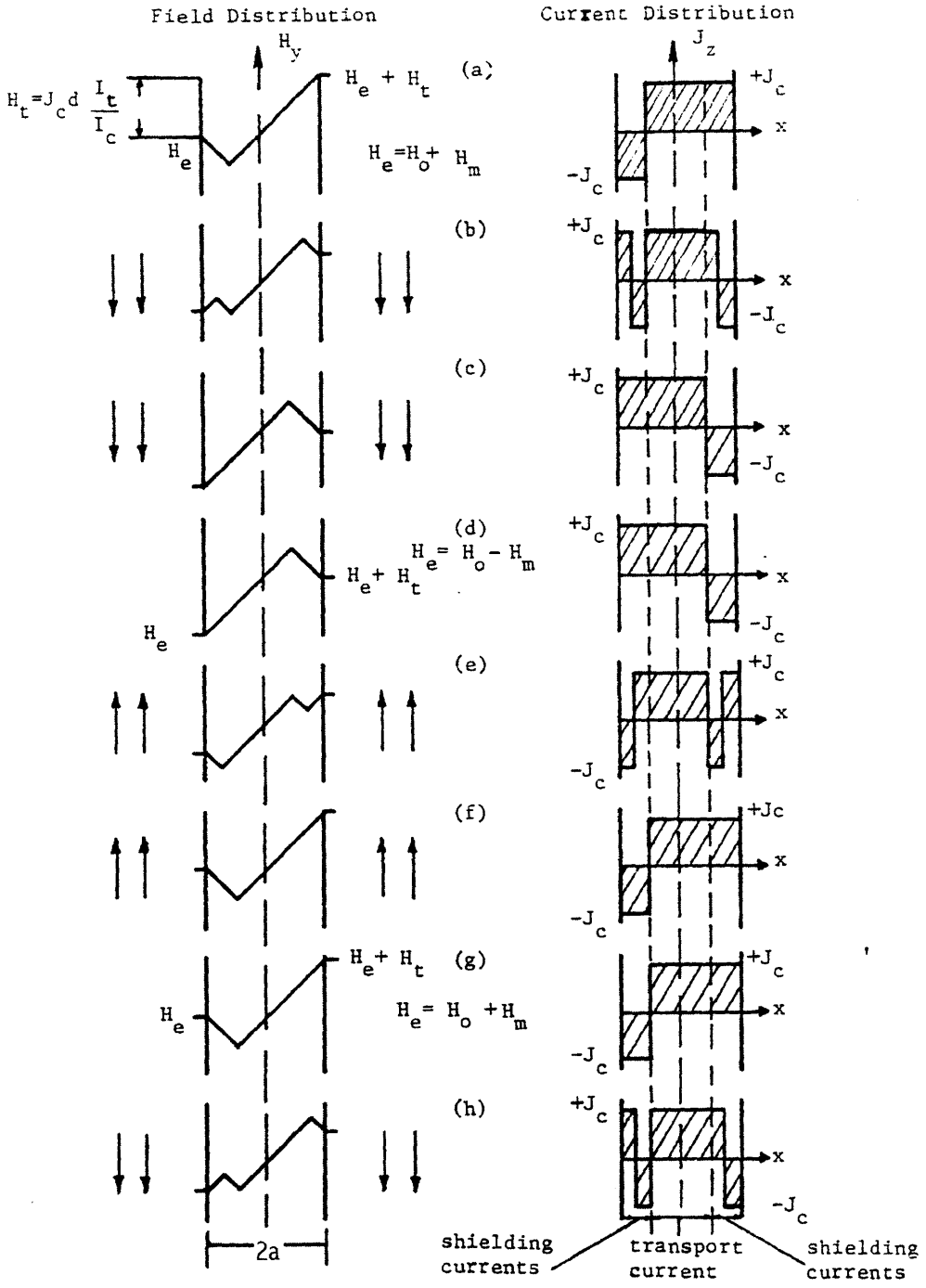

Figure 2.8 Current and magnetic field distributions inside a type-II superconductor carrying a transport current $\frac{I_T}{I_c} = 0.50$ in an alternating magnetic field.[3]

'he magnetization loss density, Q'_m, per cycle calculated from Eq (2.18) and Eq (2.27) is iven by the following equation[2.15]

$$Q'_m = \frac{\mu_0 H_m H_p}{2}\left(1 - i^2\right) \qquad H_m >> H'_p \qquad (2.29).$$

'he loss in a slab with transport current is very similar to the loss in a slab without 'ansport current modified by a term proportional to the transport current. It is also ıteresting to note that the hysteresis loss is totally unaffected by the transport current if I_m is less than H'_p.

he experimental technique developed in this thesis detects only the loss from the ıagnetization currents. However, it should be noted that the total losses of the ıperconductor actually increase by a factor of $\left(1 + i^2\right)$ while the magnetization loss ecreases by a factor of $\left(1 - i^2\right)$. This discrepancy is apparent when the total energy loss calculated using the Poynting Vector energy approach. The Poynting vector, **S**, is a ector quantity that describes both the magnitude and direction of the energy flow rate of ectromagnetic waves defined by the following expression[20]

$$\mathbf{S} = \mathbf{E} \times \mathbf{H} \qquad (2.30).$$

he magnitude of the Poynting vector gives the flow of energy through a cross-sectional 'ea perpendicular to the propagation direction of the wave per unit area and time. The ıtal energy flow per unit time or power out of any closed surface is given by the integral f the Poynting vector over the surface for one cycle, represented by the following ıuation[20]

$$P = \oint \mathbf{S} \cdot d\mathbf{A} \qquad (2.31).$$

The hysteresis loss density is given by the difference between the Poynting energy density and the magnetic energy density stored in the superconductor. Fig 2.9 shows the field distributions within a superconducting slab carrying a normalized transport current, I, according to the Bean model when the external magnetic field is increased from H_e to $H_e + \Delta H_e$. The electric field at x = 0 is directed into the paper and given by[15]

$$E_z(0) = -\mu_0 a(1-i)\frac{dH_e}{dt} \qquad (2.32).$$

The Poynting vector at x = 0, $\mathbf{S}(0) = \mathbf{E}(0) \times \mathbf{H}_e$, is directed into the slab because the magnetic field is pointed in the +y-direction and the electric field is pointed into the

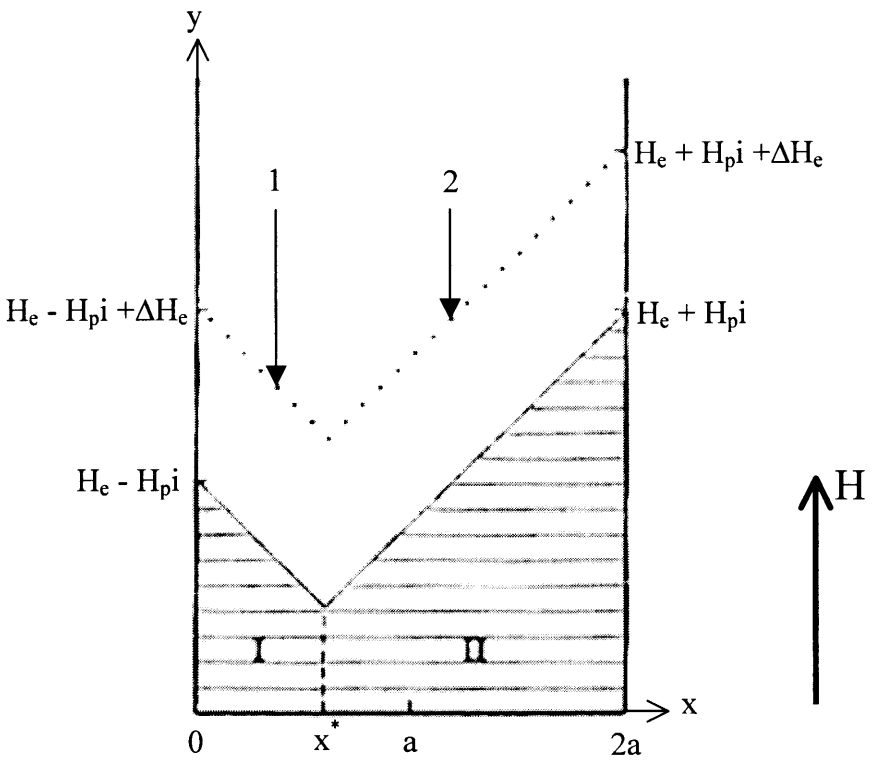

Figure 2.9 Magnetic field distribution in a superconducting slab carrying a transport current of i as predicted by the Bean model. The dotted lines show the field distribution after the field is increased by ΔH_e.

paper. The energy flux at x = 0, $\varepsilon_s(0)$, is calculated from the Poynting vector and given by the following expression[15]

$$\varepsilon_s(0) = \int |\mathbf{S}(0)| dt = a\mu_0 (1-i)(H_e - H_p i)\Delta H_e \tag{2.33}$$

The electric field at x = 2a is directed out of the paper and given by[15]

$$E_z(2a) = \mu_0 a(1+i)\frac{dH_e}{dt} \tag{2.34}$$

The Poynting vector at x = 2a, $\mathbf{S}(2a) = \mathbf{E}(2a) \times \mathbf{H}_e$, points in the –x-direction, into the slab, because the magnetic field is in the +y-direction and the electric field is out of the paper. The energy flux at x = 2a, $\varepsilon_s(2a)$, is given by the following expression[15]

$$\varepsilon_s(2a) = \int |\mathbf{S}(2a)| dt = a\mu_0 (1+i)(H_e + H_p i)\Delta H_e \tag{2.35}$$

The total Poynting input energy density, e_s, is determined by summing Eq (2.33) and Eq (2.35) and then dividing by the width of the slab, 2a. The total Poynting energy density is given by the following equation[15]

$$e_s = \frac{1}{2a}[\varepsilon_s(0) + \varepsilon_s(2a)] = \mu_0 (H_e + H_p i^2)\Delta H_e \tag{2.36}$$

The change in magnetic energy stored in the slab from the original state, H_e, to the new state, $H_e + \Delta H_e$, must be calculated next. The computation is divided into two regions where $x^* = (1\text{-}i)a$. Region I is the region of the slab where x falls between 0 and x^* and region II is the region of the slab where x falls between x^* and 2a. The change in magnetic energy stored in the slab for region I, $\Delta\varepsilon_{m1}$, is given by the following expression[15]

$$\Delta\varepsilon_{m1} = \frac{\mu_0}{2a}\int_0^{(1-i)a}\left[H_1'^2(x) - H_1^2(x)\right]dx \tag{2.37}$$

where $H_1'(x)$ is the magnetic field distribution of the new state and $H_1(x)$ is the magnetic field distribution of the original state. Solving Eq (2.37) gives the following expression for the change in stored magnetic field energy in region I[15]

$$\Delta\varepsilon_{m1} = a\mu_0\left[H_e(1-i) - \frac{H_p}{2}(1-i^2)\right]\Delta H_e \tag{2.38}$$

The change in magnetic energy stored in the slab for region II, $\Delta\varepsilon_{m2}$, is given by an expression similar to Eq (2.37)[15]

$$\Delta\varepsilon_{m2} = \frac{\mu_0}{2a}\int_{(1-i)a}^{2a}\left[H_2'^2(x) - H_2^2(x)\right]dx \tag{2.39}$$

where $H_2'(x)$ is the magnetic field distribution of the new state and $H_2(x)$ is the magnetic field distribution of the original state. Solving Eq (2.39) gives the following expression for the change in stored magnetic field energy in region II[15]

$$\Delta\varepsilon_{m2} = a\mu_0\left[H_e(1+i) - \frac{H_p}{2}(1-i^2)\right]\Delta H_e \tag{2.40}$$

The change in magnetic energy density stored in the slab, Δe_m, is now calculated by summing Eq (2.38) and Eq (2.40) and dividing by the width of the slab, 2a, or[15]

$$\Delta e_m = \frac{1}{2a}\left(\Delta\varepsilon_{m1} + \Delta\varepsilon_{m2}\right) = \mu_0\left[H_e - \frac{H_p}{2}(1-i^2)\right]\Delta H_e \tag{2.41}$$

The hysteresis energy density, Q_h', can now be calculated by subtracting Eq (2.41) from Eq (2.36), which gives the following expression[15]

$$Q'_h = \mu_0 \frac{H_p}{2}\left(1+i^2\right)\Delta H_e \qquad (2.42)$$

Eq (2.42) was developed for the case when the external magnetic field is much stronger than the modified penetration field, $H_e >> H_p(1\text{-}i)$. For the case when the field is increased from zero to H_m, Eq (2.42) becomes

$$Q'_h = \frac{\mu_0 H_m H_p}{2}\left(1+i^2\right) \qquad H_m >> H'_p \qquad (2.43)$$

The difference between Eq (2.43) and Eq (2.29) is given by the following expression[2]

$$Q_T = Q'_h - Q'_m = \frac{\mu_0 H_m H_p}{2} 2i^2 \qquad (2.44).$$

where Q_T is the transport loss density. The extra energy loss is supplied by the current source. As the external field increases, the transport current is driven to decrease and the power supply develops a voltage to maintain a constant current. Hence, the current source must do work to maintain a constant transport current in the presence of an alternating magnetic field. Therefore, the total hysteresis loss can be divided into a magnetization loss, Q'_m, that occurs from the magnetization currents and a transport loss, Q_T, that occurs from the transport current supply working to maintain a constant transport current.[2,15] In the interest of time, the magnetization loss was the only mode of dissipation investigated in this thesis.

2.2.4 Coupling Current Loss

Coupling currents flow within the matrix between superconducting filaments induced by a time-varying magnetic field or transport current. Since coupling currents flow in the

matrix, the mode of power dissipation is Joule heating in the normal material. However, the interaction between an array of superconducting filaments within the matrix is highly non-linear and the calculation of J and E is very complicated. The inter-filament currents are driven by the induced electric field described by Faraday's law and decay in a much more complicated way.

The power dissipated by the coupling currents is[15]

$$P = \frac{\left(\dot{B}L\right)^2}{\rho_t} \tag{2.45}$$

where ρ_t is the effective transverse resistivity of the strand, $\dot{B}$ is the changing external magnetic field, and L is the length of superconductor. Since the frequency of the magnetic field is small, the power dissipation due to coupling currents for this experiment is quite small when compared to the hysteresis loss.

The coupling currents have a more significant effect on the hysteresis loss of the conductor, however. As was shown in the earlier section, the hysteresis loss is proportional to the filament dimensions. The coupling currents electromagnetically link the filaments and the conductor behaves like a single core superconductor. The effective filament dimensions increase which in turn increases the hysteresis loss. A diffusion time constant defined by[15,22]

$$\tau = \frac{\mu_0}{2\rho_m}\left(\frac{L^2}{2}\right) \tag{2.46}$$

, where L is the length of the sample and ρ_m is the matrix resistivity, is used to predict the behavior of the superconductor. Long samples with a low effective matrix resistivity have long paths and long decay times for the coupling currents. The monofilament behavior has been observed at very low frequencies of only a couple of Hertz for tape superconductors with silver matrix. It has been reported that the total 50 Hz magnetic field losses are typically enhanced by a factor of 5-10 compared to the hysteresis losses of the individual filaments of HTS multifilament tape superconductors.[15,23,24]

3 Experimental Setup

3.1 Introduction

High temperature multifilament BSCCO-2223/Ag superconducting tape can now be fabricated in long lengths. However, the properties of the superconductor are not uniform over these long lengths. For technical and commercial success of high temperature superconductors, high quality wires with adequate critical currents and low levels of energy loss must be available. To improve the wires, it is important to have methods in place to measure and quantify the properties of the conductors. This experiment was designed to characterize the properties of BSCCO-2223/Ag tapes over a range of temperatures and subjected to conditions consistent with fusion applications.

3.2 Experimental Techniques

3.2.1 V-I Characteristic for J_c Measurement

The critical currents of BSCCO-2223/Ag-sheathed tapes were measured as a function of external magnetic field and temperature by directly monitoring the electric field through voltage taps on the conductor. The method for the critical current measurements was a typical four terminal method. Two voltage taps were soldered to the samples 0.1 m apart, and two copper current leads were soldered to ends of the tapes. The sample was placed in a uniform magnetic field either parallel or perpendicular to the ab-plane. The voltage across the sample was measured as the transport current in the sample was increased, which was controlled by an external power supply. While the sample was in the

superconducting state, no voltage was measured. As the current passed the critical value for the field and temperature conditions, the measured voltage increased. A computer and a chart recorder were used to record the voltage as a function of the transport current in the sample, generating the V-I characteristic curve. The critical currents of the samples were then determined from the V-I curves and electric field criteria. ITER reports critical currents that correspond with an electric field criterion of 10 μV/m while many groups working with HTS materials report critical currents that correspond to an electric field criterion of 100 μV/m. Since the voltage taps were placed 0.1 m apart for this experiment, the critical current was determined at a sample voltage either 1 μV or 10 μV.

It has been established, in a purely empirical way, that the voltage developed by a multifilamentary superconductor at currents close to the critical value behaves approximately as J^n where n is a characteristic value of the superconductor.[2] Higher values of n indicate a rapid increase of voltage across the sample as the current increases. An existing computer program was used to analyze the n value based on a two-point data set obtained from the V-I characteristic curve. The program calculated the n value using Eq (3.1),

$$\frac{V}{V_0} = \left(\frac{I}{I_0}\right)^n \tag{3.1}$$

where I_0 is the measured current associated with an electric field, V_0, of 10 μV/m while I is the measured current associated with an electric field, V, of 100 μV/m. The critical

currents and n value were compared to a curve-fitting analysis that calculated the n value from Eq (3.2),

$$\log(V) = \alpha + n\log(I) \tag{3.2}$$

where α is a fitting parameter. The critical current and n value determined from Eq (3.1) were compared to the critical current and n value determined from Eq (3.2). The data was accepted if the critical current and n values were similar for both calculations.

For the critical current test, several factors must be considered in order to record an accurate value of the critical current for specific conditions. One concern is the temperature of the sample. Since current leads are not superconducting, ohmic heating occurs in the resistive contacts and adds a thermal load to the sample. If the heat diffuses into the bulk, it can cause a significant reduction of the measured critical current and can even damage the sample. Therefore, it is important to keep the resistive power dissipation in the current leads and joints to a level which can be removed adequately by the available coolant to avoid an appreciable temperature rise in the sample.

Another concern is the sample support mechanism. Most critical current tests are performed with the current perpendicular to the magnetic field because this situation is very common in magnets. Therefore, the sample will experience a Lorentz force in the form of $F = J \times B$. This Lorentz force could cause the sample to move or bend during the test, which would damage or degrade the sample performance. Also, since the properties of HTS materials are highly anisotropic, the critical currents are very sensitive to the

magnetic field orientation. Therefore, proper support of the sample is essential to restrict the movement during the measurements.

Another factor that affects the critical current measurement is the ramp speed of the transport current during the test. The critical currents measured with current ramp speeds of 0.1 Amp/s are very different from the critical currents measured from pulsed experiments, where the current change can be as fast as 10^5 Amp/s. One reason for this difference in measurement results from the current ramp itself. Power dissipation occurs in the sample while the current is changing and increases as the ramp speed increases. This power dissipation causes a temperature rise in the sample which then affects the critical current measurement. A strict DC measurement of the V-I curve and critical current is impossible because the very definition of DC is that $\frac{dI}{dt} = 0$. Nevertheless, accurate results for the DC critical current can be obtained from the V-I curve when the current ramp rate is significantly slow. This is defined by a speed where the AC loss dissipation can be cooled by the surrounding fluid or conducted away to maintain the sample temperature constant.

The critical current of BSCCO-2223/Ag superconducting tapes was investigated under various conditions. The effects of magnetic field orientation and strength, temperature, and current ramp rate on the critical current were measured, and the results are reported in Chapter 4. The measurement technique was extended from previous work at the Plasma Science & Fusion Center of measuring the critical current in Nb_3Sn superconductors.

Fig 3.1 shows the instrumentation used for the critical current measurement. The HP 34420A nanovolt/micro-ohm meter was used to measure the voltage taps on the superconductor and the external magnetic field measured by the hall probe. The HP 34420A has two input channels and recorded the sample voltage and hall probe voltage simultaneously. The HP 3458A multimeter was used to measure the transport current in the superconductor by monitoring the voltage across the 100mV/100 A shunt of the transport current power supply, an HP 6260B. The sample voltage, current, and the external magnetic field were recorded on a Macintosh computer through a GPIB interface using LabVIEW software. The V-I curves were also recorded on a Goerz-Metrawatt SE780 chart recorder. The sample voltage was supplied by the analog output of the HP 34420A and was connected to channel Y of the chart recorder. The HP 6260B shunt voltage was connected directly to channel X of the chart recorder. The V-I characteristic was then recorded directly on the chart. The results of both measurement devices were then compared for accuracy.

The critical currents of BSCCO-2223/Ag-sheathed tape superconductors were measured at temperatures ranging from 77 K to 115 K with externally applied DC magnetic fields of strengths from zero to 0.4 T. The samples were first brought to the temperature of interest. Then, the DC magnetic field was applied. The V-I curve was obtained by slowly increasing the current in the superconducting sample and recording the voltage across the sample while the temperature and magnetic field remained constant. Eventually, the current reached the critical value, the Lorentz force on the flux vortices

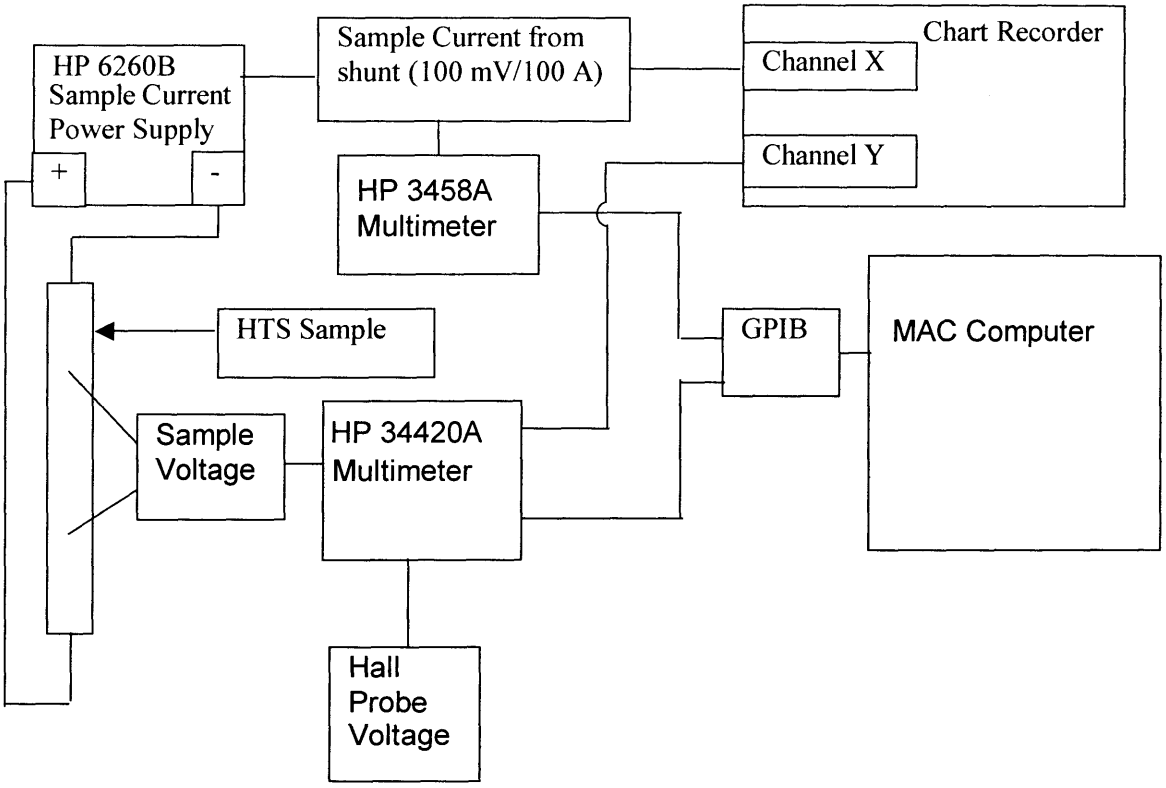

Figure 3.1 Circuit used to measure the critical current of BSCCO-2223/Ag tapes. The multimeters were connected to the computer through a GPIB connection.

was greater than the pinning force, flux flow occurred, and the voltage across the sample increased.

3.2.2 Magnetization Method for AC Loss Measurement

The losses in a superconductor are an unwanted heat load and affect the efficiency and economics of superconducting systems. Therefore, it is important to quantify the losses and improve the performance of the superconductor. The measurement technique used here is based on estimating the AC losses by integrating a Poynting Vector $(\mathbf{E} \times \mathbf{H})$ on a closed surface surrounding the sample over a cycle of the magnetic field.

The loss power density dissipated in the box shown in Fig 3.2 is given by the Poynting vector as follows

$$Q = -\frac{1}{V_{sc}} \int_T \int_A (\mathbf{E} \times \mathbf{H}) \cdot d\mathbf{A} dt \tag{3.3}$$

where V_{sc} is the volume of superconductor in the box, T is the period, A is the whole surface area of the box, **E** is the electric field, and **H** is the magnetic field. The surface integral of $(\mathbf{E} \times \mathbf{H})$ is zero everywhere except for the shaded region. Also, the contribution of each shaded region to the loss density is the same because of symmetry. Therefore, Eq (3.3) reduces to the following expression

$$Q = -\frac{2}{V_{sc}} \int_T \int_{A_1} (\mathbf{E}_1 \times \mathbf{H}) \cdot d\mathbf{A} dt \tag{3.4}.$$

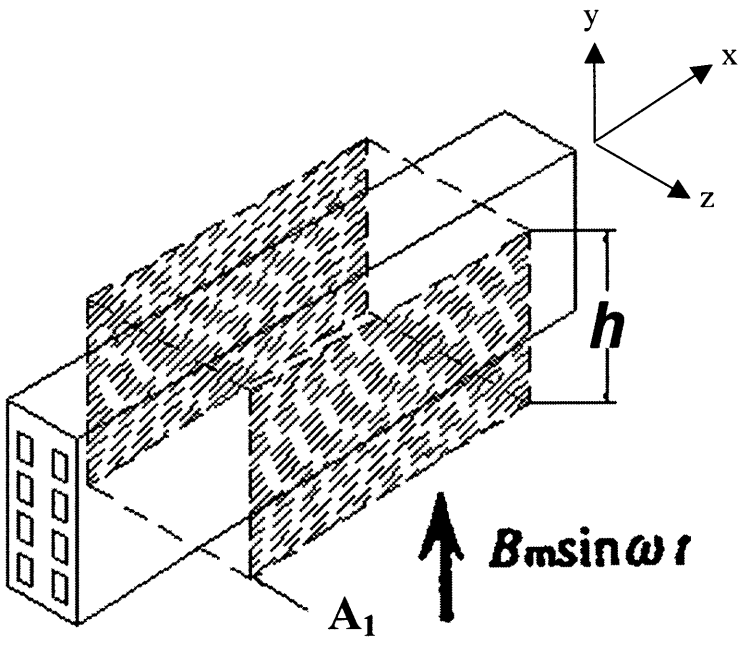

Figure 3.2 Drawing of BSCCO-2223 tape superconductor in an alternating external magnetic field. The box represents the boundaries over which the surface integral of the Poynting Vector was performed. The shaded region, A_1, represents the area of one side of the box with height, h, and 100 mm long.

Next, a pick up coil of N turns is assumed wound completely over the shaded region S in a direction parallel to the x-axis. The winding pattern for the pick up coil is located in section 3.4.3 of this thesis. The d**A** term is now given as

$$d\mathbf{A} = \frac{h d\mathbf{x}}{N} \tag{3.5}$$

where d**x** is a small line element along the pick up coil wire on the surface A_1. If the pick up coil is wound flat, then **E** is assumed to be in the plane A_1 and in the direction parallel to the pick up coil wires. Furthermore, if **H** is considered parallel to A_1, then **H** is perpendicular to **E** and the cross product becomes the product of the magnitudes of the vectors. Also, if the magnetic field and the electric field are assumed to be uniform over the shaded area, then the magnetic field and electric field are only functions of time. Combining these assumptions with Eq (3.4) and Eq (3.5) gives the following relationship

$$Q = \frac{2}{V_{sc}} \int_T \frac{hH(t)}{N} \left(\int E(t) dx \right) dt = \frac{2}{V_{sc}} \int_T \frac{hH(t)V(t)}{N} dt \tag{3.6}.$$

The definition $V(t) = \int E(t) dx$ where V(t) is the pick up coil voltage, E(t) is the electric field induced from the losses in the superconductor, and dx is a line element along the wire were used in simplifying Eq (3.6). The applied magnetic field has the form $H(t) = H_m \sin(\omega t)$. The pick up coil voltage will have the same form as the magnetic field, but the phase will be different. The phase is different because the pick up coil voltage has two components, an electric field component generated by the AC losses and an inductive component due to residual net flux linkage with the applied magnetic field. The electric field component is the quantity to be measured, and the inductive component is background noise for this experiment. The electric field component is in-phase with the magnetic field while the inductive voltage is 90° out-of-phase with the magnetic field.

The total phase shift of the pick up coil voltage is determined by the ratio of the electric field component and the inductive component. Therefore, the voltage will lag the magnetic field by a phase between 0° and 90° based on the ratio of the electric field component and the inductive component and has the form $V(t) = V_m \sin(\omega t - \phi)$. Substituting these forms for the magnetic field and pick up coil voltage into Eq (3.6) gives the following expression for the AC losses

$$Q = \frac{2h}{NV_{sc}} \int_T H_m \sin(\omega t) V_m \sin(\omega t - \phi) dt \tag{3.7}.$$

This integral can be solved using the trigonometric identity shown in Eq (3.8).

$$\sin A \sin B = \frac{1}{2}(\cos(A - B) - \cos(A + B)) \tag{3.8}$$

where A = ωt and B = ωt - ϕ. The lines following are the algebraic steps of combining Eq (3.7) and Eq (3.8) and reducing the following integral to a useful equation.

$$Q = \frac{2hH_m V_m}{NV_{sc}} \int_T \frac{1}{2}(\cos(\phi) - \cos(2\omega t - \phi)) dt$$

$$Q = \frac{hH_m V_m}{NV_{sc}} \left(T\cos(\phi) - \frac{1}{2\omega} \sin(2\omega t - \phi) \Big|_0^T \right)$$

$$Q = \frac{hH_m V_m}{NV_{sc}} \left(T\cos(\phi) - \frac{1}{2\omega} \sin(2\omega t - \phi) - \frac{1}{2\omega} \sin(\phi) \right)$$

$$Q = \frac{hH_m V_m}{NV_{sc}} \left(T\cos(\phi) - \frac{1}{2\omega} (\sin(2\omega T)\cos(\phi) - \cos(2\omega T)\sin(\phi)) - \frac{1}{2\omega} \sin(\phi) \right)$$

$$Q = \frac{hH_m V_m}{NV_{sc}} \left(\frac{1}{f} \cos(\phi) + \frac{1}{2\omega} \sin(\phi) - \frac{1}{2\omega} \sin(\phi) \right)$$

$$Q = \frac{hH_{rms} V_{rms}}{fNV_{sc}} \cos(\phi) \tag{3.9}$$

The following relationships were used in the previous derivation:

$$\frac{1}{T} = f = \frac{\omega}{2\pi} \tag{3.10}$$

$$H_m = \sqrt{2}H_{rms} \qquad V_m = \sqrt{2}V_{rms} \tag{3.11}$$

where T is the period in seconds, f is the frequency in hertz, and ω is the angular frequency in radians per second, and H_m and V_m are the maximum values for the magnetic field and pick up coil voltage and H_{rms} and V_{rms} are the root mean square of these quantities. In Eq (3.9), the quantities h, H_{rms}, f, N, and V_{sc} are all known quantities determined from the test set-up and are controlled by the experimenter. Therefore, only V_{rms} and ϕ are unknown, and the AC losses can be determined by measuring these quantities directly.

Fig 3.3 shows the instrumentation used to measure the AC losses in BSCCO-2223/Ag tape superconductors as a function of magnetic field frequency, magnetic field amplitude, and as a function of transport current. A pick up coil, referred to as the sample coil, was placed directly on a specimen inside an external magnetic field. A second pickup coil, referred to as the balancing coil, was placed in close proximity to the sample coil such that the external magnetic flux through both pick up coils was the same, but the balancing coil was far enough away to be unaffected by the flux produced by currents in the sample. The output voltages from the pick up coils were added so as to cancel most of the inductive background voltage induced by the changing magnetic field. The balancing coil was larger than the measurement coil by 5 turns so the summed output voltage of the pickup coils could be adjusted to zero through a potentiometer.

The lock-in amplifier used for this experiment was an EG&G Instruments 7265 DSP Lock-in amplifier with two inputs and sensitive to frequencies in the range of 0.001 Hz to 250 kHz and voltages in the range of 2 nV to 1 V full-scale.

One feature of this particular lock-in amplifier that greatly reduced the difficulty of the experiment was the differential input feature. With this feature, the sample pick up coil was connected to input A of the lock-in amplifier while the balancing pick up coil was connected through a reducing circuit, shown in Fig 3.4, to input B. The voltage signal from the balancing coil was reduced in magnitude according to the following relationship

$$V_{out} = \frac{R}{10^5} V_{in} \tag{3.12}$$

where V_{out} is the output voltage from the reducing circuit, R is the resistance set by the potentiometer, and V_{in} is the input voltage from the balancing pick up coil. The 10^5 factor in the denominator is the maximum value of the resistance for the particular potentiometer used in this experiment.

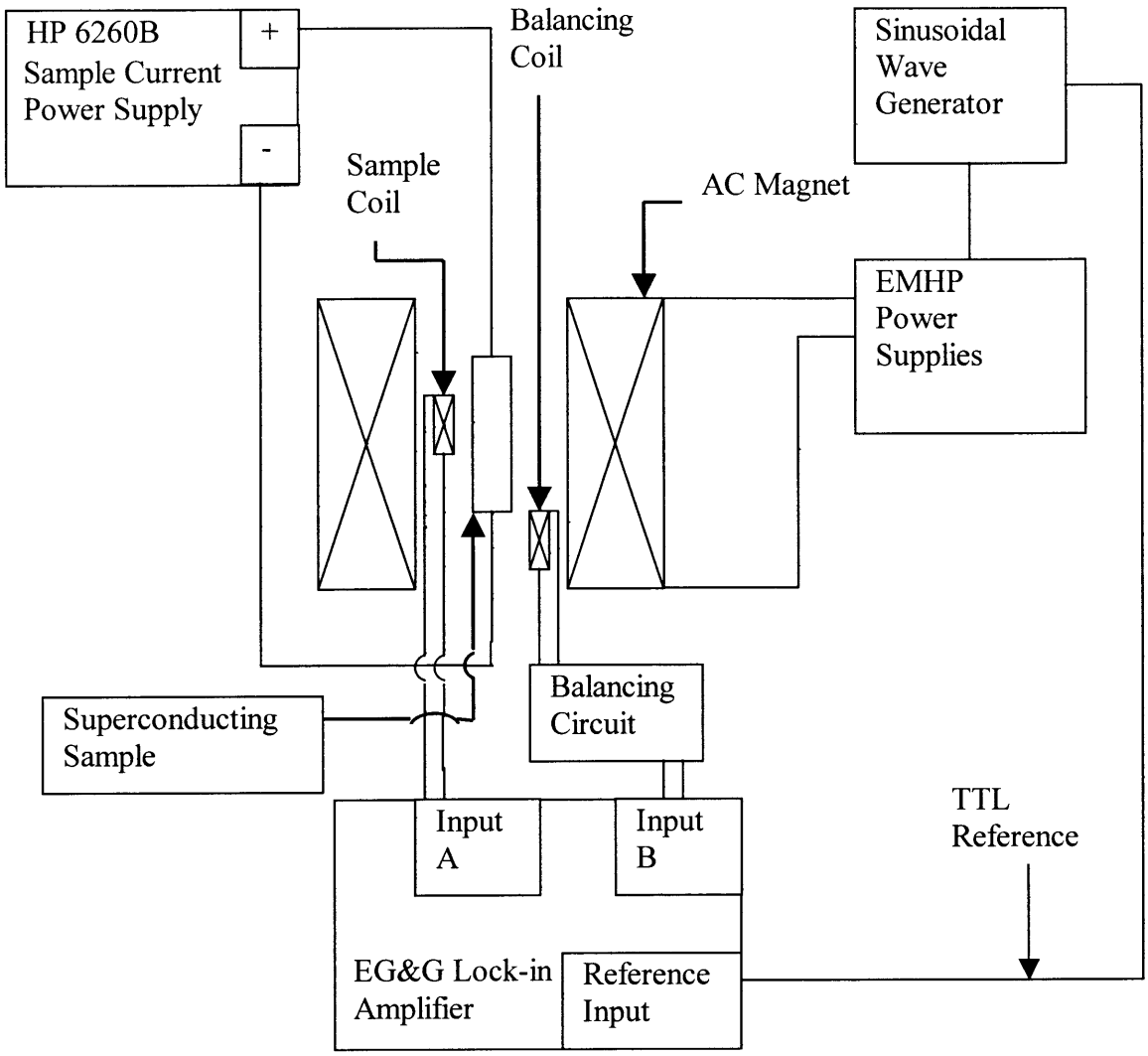

Figure 3.3 Schematic of the experimental setup for the AC loss measurements.

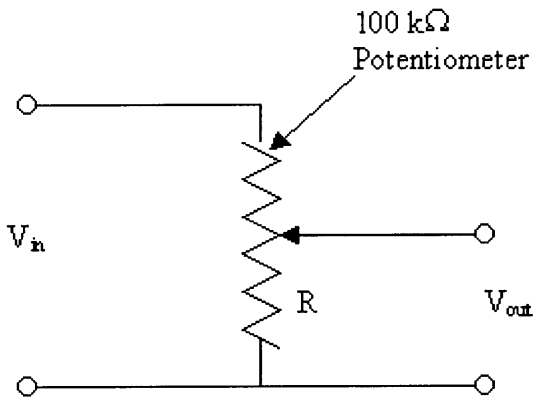

Figure 3.4 Schematic for the reducing circuit used to adjust the voltage measured from the balancing pick up coil.

The lock-in amplifier measured these voltages separately and then reported the difference between the signals as a single root mean square (rms) voltage, V_{rms}. The lock-in amplifier was also capable of displaying the component of the signal voltage that was in-phase with the magnetic field and the component 90° out-of-phase with the magnetic field simultaneously. Therefore, by adjusting the potentiometer in the reducing circuit, it was possible to approximately cancel the inductive voltage of the sample pick up coil with the inductive voltage of the balancing pick up coil. Reducing the inductive background noise increased the signal-to-noise ratio from approximately 1:250 to 1:1.

Another feature of the EG&G lock-in amplifier that significantly reduced the difficulty of the experiment was the ability to measure the in-phase component and the 90° inductive component of the pick up coil voltage directly and simultaneously. The phase of the magnetic field was measured from a hall probe positioned near the sample inside the dewar with respect to the TTL output of the function generator. The lock-in amplifier was then programmed to measure the components of the differential voltage signal from the pick up coils that had the same phase with respect to the TTL output as the magnetic field. For the in-phase component of the pick up coil voltage, the cos (ϕ) term in Eq (3.9) was equal to 1 and the equation for the experimental determination of the AC losses reduced to the following form

$$Q = \frac{hH_{rms}V'_{rms}}{fNV_{sc}} \qquad (3.13).$$

where V'_{rms} is the rms value of the voltage in-phase with the magnetic field.

This feature was also important for the balancing of the pick up coils. For experiments that utilize the magnetization method for AC loss measurements, the pickup coils are usually balanced in the absence of the sample. Then, the sample is inserted without disturbing the pick up coils and the measurements are taken. This experiment was performed differently because the experiments were performed at cryogenic temperatures and the sample could not be inserted after the pick up coils had been cooled and balanced. Therefore, it was necessary to balance the pick up coils with the sample in place. Assuming the balancing coil was placed far enough away from the sample so that the voltage signal was purely inductive, then the total inductive voltage signal measured by the lock-in amplifier could be minimized without affecting the in-phase electric field component by adjusting the potentiometer. Since the lock-in amplifier displayed the in-phase and inductive components separately, the assumption was confirmed experimentally and reducing the background noise was performed at 77 K.

The AC losses of BSCCO-2223/Ag sheathed tapes subjected to an AC magnetic field and no transport current were measured at 77 K as a function of magnetic field strength and magnetic field frequency. The effect of transport current on the AC losses at a fixed frequency and amplitude were also studied. The samples were cooled to 77 K using a liquid nitrogen bath. The AC magnetic field with the maximum field strength of 0.4 T and a frequency of 0.093 Hz was applied. Then, the potentiometer was adjusted to minimize the inductive background voltage. Now, the AC loss measurements could be performed.

The AC losses were measured as a function of magnetic field frequency for half-cycle sweeps, as shown in Fig 2.6(b), at constant maximum field strength. The applied magnetic field was an alternating sine wave, as shown in Fig 4.13, with a peak magnetic field of 0.375 T at frequencies of 0.057, 0.073, 0.093, 0.110, and 0.130 Hz. Frequencies that are multiples of 60 were avoided because of the uncertain interaction between the lock-in amplifier and the line signal from the building.

The AC losses were also measured as a function of the magnetic field amplitude for a constant sweep frequency of half-cycle sweeps. The applied magnetic field was a sine wave with a minimum of zero to maximum strengths of 0.1, 0.2, 0.25, 0.30, 0.35, and 0.375 T at a sweep frequency of 0.093 Hz. The effect of DC transport current on the AC losses was measured at a field frequency of 0.093 Hz and a maximum strength of 0.35 T. The DC transport current was increased in steps of 10 A from zero to a maximum of 100 A. The results and discussions of these experiments are listed in Chapter 4.

For each test, the sample was cooled to 77 K and the pick up coils were balanced as discussed in the previous section. Next, the magnetic field was adjusted to the desired conditions as listed above. Then, if the experiment conditions required transport current, the DC transport current was added. A time delay of approximately 5 minutes was allowed for the conditions to reach a steady state value before recording the data. The V_{rms} output of the lock-in amplifier was recorded on a Yokogawa chart recorder as a function of time. Each data point required at least 10 minutes before for an average value could be determined.

3.3 Copper Electromagnet

A large, water-cooled copper electromagnet was used to generate the DC magnetic fields necessary for the critical current measurements and to generate the AC magnetic fields necessary for the AC loss measurements. The electromagnet was comprised of a split solenoidal magnet pair with an iron yoke and two pole pieces, which concentrate the magnetic flux. Fig 3.5 shows a photograph of the magnet used for the experiments. The copper coils had a diameter and a thickness of approximately 0.91 m and 0.15 m, respectively. The pole pieces were 0.30 m in diameter and 38.1 mm thick. The south coil pole piece was removed to increase the gap to approximately 0.19 m to allow access for the dewar. A hall probe was used to measure the uniformity of the magnetic field generated between the coils. These measurements were used to determine the placement of the sample during the tests. Plots for the magnetic field uniformity and field saturation tests are given in Appendix A.

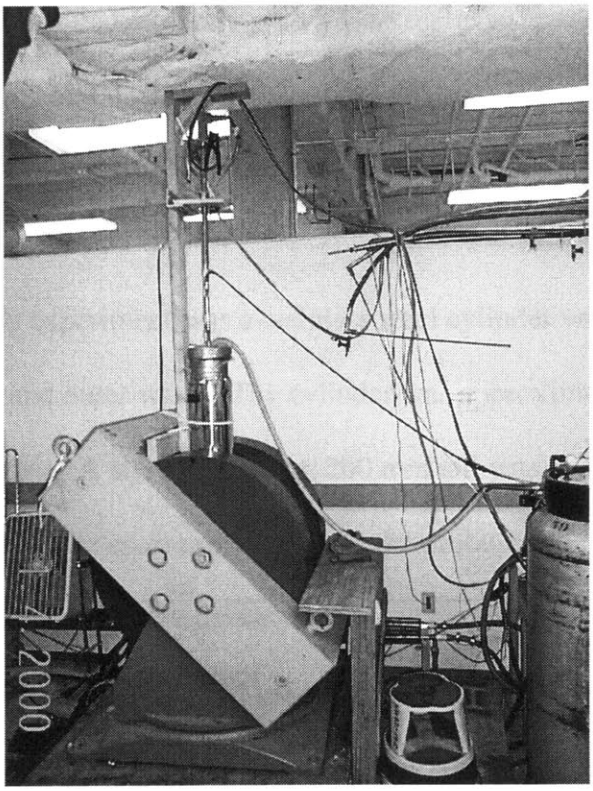

Figure 3.5 Picture of copper magnet used for all experiments performed for this thesis.

Since the copper magnet was a DC magnet and had a high inductance, distortion of the sine wave pattern of the alternating fields was expected. The distortion was measured by using the lock-in amplifier to observe the harmonics of the hall probe signal. The most distortion was expected to occur at the higher frequencies of magnetic field sweep. Therefore, the harmonics of the hall probe voltage in an alternating magnetic field at a frequency of 0.130 Hz and a maximum strength of 0.35 T were measured. Fig 3.6 shows a plot of the rms value for the hall probe voltages for the first five harmonics. The basic harmonic was over 10,000 times greater than the others, and, therefore, the distortion of the magnetic field was considered to be negligible at 0.130 Hz. Since all measurements

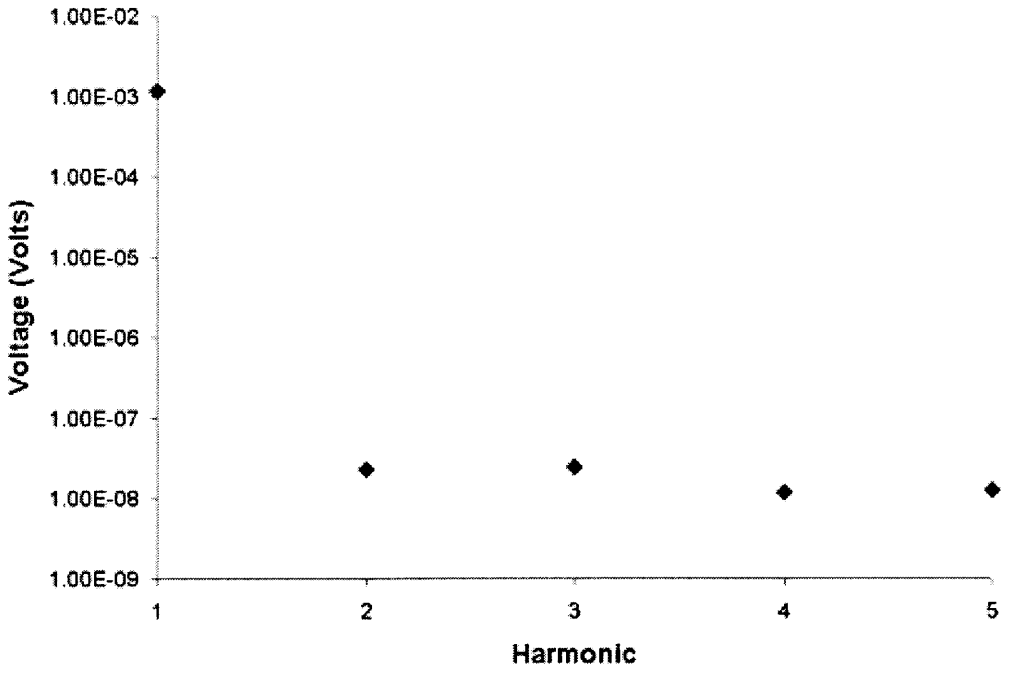

Figure 3.6 Harmonics of the hall probe rms voltage signal when the copper electromagnet is ramped to a maximum field strength of 0.4 T in a sine wave pattern at 0.130 Hz.

were done at frequencies equal to or lower than 0.130 Hz, the assumption of a pure sine wave was considered valid for all experiments.

3.3.1 Magnet Power supplies

Two EMHP 30 V/600 A power supplies were used to charge the copper magnet up to magnetic fields of 0.4 T. Two power supplies operated in series were needed to supply the volts necessary to drive the 100 A current, which induced the maximum magnetic field of 0.4 T. For the DC tests, the power supplies were controlled remotely by a HP 6282A DC power supply to maintain constant magnetic fields. For the AC tests, the

power supplies were controlled remotely with a low frequency sinusoidal wave generator to control the ramp speed and peak field magnitude.

3.3.2 Dewar

The dewar used for this experiment was a stainless steel cylinder with a 12.7 mm vacuum gap between the inner and outer walls. The cylinder was approximately 1 m tall with an inner diameter of 150 mm. A styro-foam plug 200 mm tall was constructed to isolate the interior of the dewar from the environment. Since the probe was fixed into place to hold the sample in the magnetic field, the dewar was placed on an adjustable stand so the liquid level relative to the probe could be controlled during the temperature dependency experiments. In order for the sample to reach temperatures higher than 77 K, cooling from the rising cryogen vapor was balanced by heating from the heating coil to maintain a constant temperature above 77 K. Since the dewar was on an adjustable stand, the sample could be immersed in the cryogen bath or removed completely out of the liquid without moving the sample relative to the magnetic field.

3.4 Design of Test Probe

3.4.1 Test Probe

A photograph of the test probe is shown in Fig 3.7. The design drawings for each probe piece are listed in Appendix B. The purpose of the probe was to provide support for the sample for magnetic fields oriented in-plane with the broad face of the tape, as well as perpendicular to it. The probe also provided a means to attach instrumentation, transport cryogens, and add transport current to the sample.

The test probe was designed under the constraints of environmental heat load, current lead contacts, and magnetic field. The following sections outline the effects these factors had on the design of the probe. The probe was also designed to fit inside the bore of a superconducting dipole magnet located in building NW-22 laboratory at the Plasma Science & Fusion Center at MIT. It was expected that the dipole magnet would be used during subsequent tests once the experimental technique was developed and understood using the copper electromagnet. However, these tests are beyond the scope of this thesis, and further experimentation in the superconducting dipole magnet is left for future work.

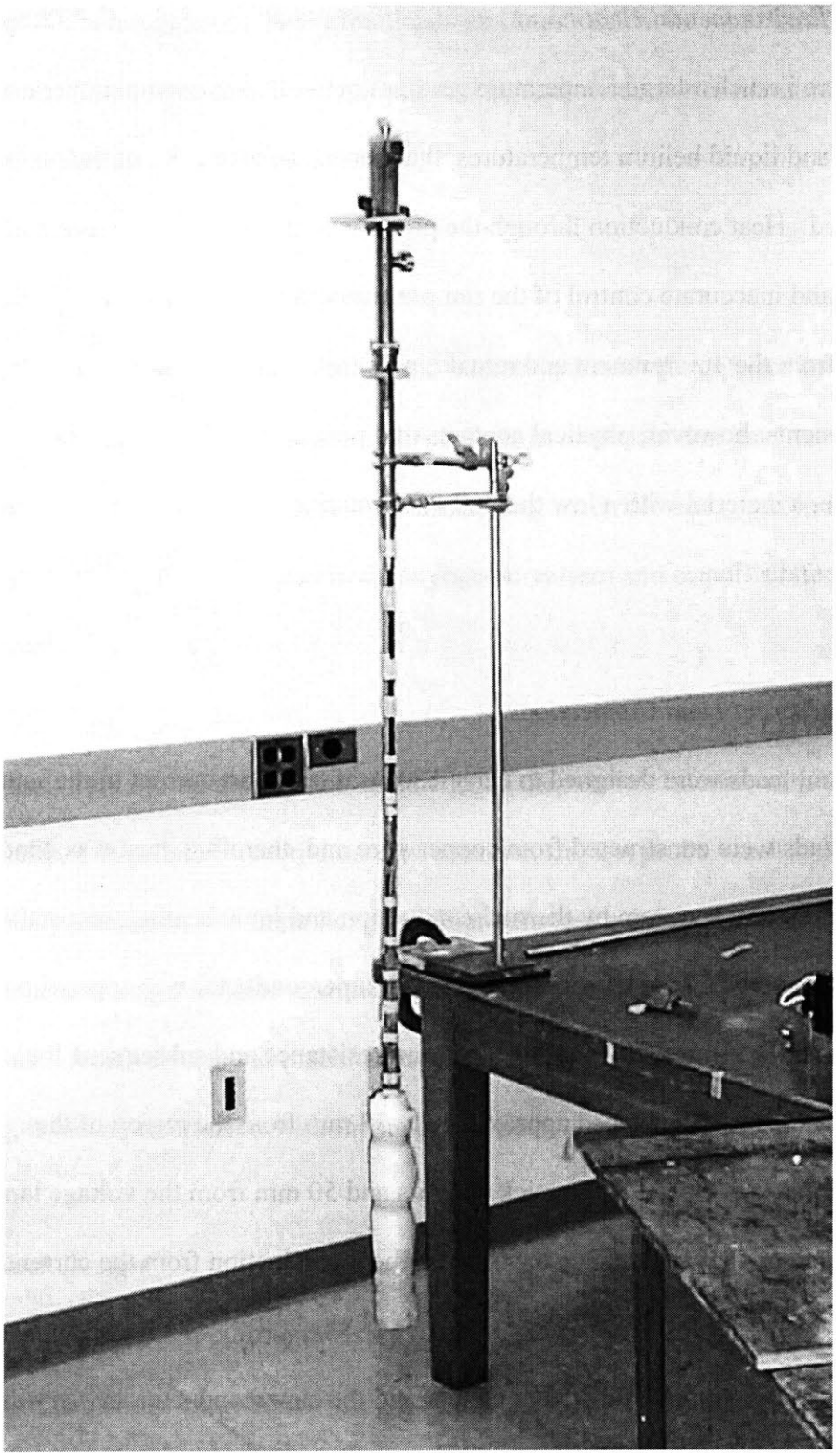

Figure 3.7 Test probe used for measurements. The sample area is insulated using styro-foam.

3.4.1.1 Environmental Heat Load

Since there is such a large temperature gradient between room temperature and liquid nitrogen and liquid helium temperatures, the thermal conductivity of the probe should be minimized. Heat conduction through the probe would result in excessive boil off of the cryogen and inaccurate control of the sample temperature. Ideally, the sample should be isolated from the environment and remain in an isothermal state during the measurements; however, physical contacts that penetrate the dewar were necessary. Therefore, a material with a low thermal conductivity, G-10, was used to minimize the thermal conduction.

3.4.1.2 Current Lead Connections

The current leads were designed to carry 100 A of transport current to the sample. The current leads were constructed from copper wire and, therefore, heat was conducted into or dissipated in the system by thermal conduction and joule heating, respectively. The contact area between the current leads and the superconductor was approximately 25 mm in length and 3.5 mm wide to reduce the joint resistance and subsequent Joule heating. The current leads were placed approximately 38 mm from the region of the superconductor enclosed by the pick up coils and 50 mm from the voltage taps soldered to the superconductor to reduce the effect of heat conduction from the current leads.

Thermal contraction coefficients of copper and the superconductor are very different over the temperature range from room temperature to cryogenic temperatures. Since strain affects the critical current of superconductors in an adverse way, the strain caused by the

different contraction lengths of the current leads and superconductor was considered. Flexible current leads were therefore attached to the superconductor to minimize the effect of strain due to thermal contraction.

3.4.1.3 Magnetic Field

The test probe should have no electromagnetic interactions with the external magnetic field. Changing magnetic fields induce eddy currents in materials that have low electrical conductivities. These eddy currents flow in conducting materials and result in Joule heating which could pose a heat load to the cryogenic system and can also affect the temperature of the sample.

The probe materials should also be non-magnetic, so they do not interact with the magnetic field. The primary material used to construct the test probe was G-10, which is a commercially available, non-metallic, glass fiber composite material that provides excellent structural support while minimizing thermal and electrical conduction. G-10 material is also relatively easy to machine, and, since it is non-magnetic and non-conducting, it has no interaction with the magnetic field.

3.4.2 Heater Design

A heater was designed and built to measure the critical current at temperatures ranging from 4.2 K to 120 K. In conjunction with the sample heater, the sample was held in the vapor above the cryogenic liquid to maintain a constant temperature. The convection cooling from the rising vapor was balanced by conduction heating from the externally

powered resistive heater coil. The heater coil was constructed from a 9 gauge stainless steel wire approximately 3.85 m long wrapped non-inductively around a thin G-10 plate that was 0.33 m long, 13 mm wide, and 1 mm thick. Notches were made approximately 3 mm apart along both sides of the G-10 plate to separate the coils and to provide support and insulation for the wire.

The coil was separated from the superconductor by a copper plate, which was necessary to distribute the thermal energy evenly over the sample. The heater coil and copper plate were secured in place using screws with the heater coil over the sample and the copper plate in between. Silicon grease was applied between the copper plate and the superconductor to increase the thermal conductivity. The heating power was controlled by a Lakeshore DRC-91C Controller. The controller monitored the temperature through two CGR sensors, one located between the heater coil and the copper plate and one located on the sample holder. The controller also regulated the power generated in the heater by controlling the current through the heater coil. The resistance of the CGR sensor was calibrated against a silicon diode temperature sensor. The measured calibration curve for CGR resistance versus temperature is given in Appendix A.

3.4.3 Pick up Coils

The pick up coils were wound from insulated low resistance 6 gauge copper wire. The geometry of the pickup coil is very important for the accuracy of the measurement. Fig 3.8 shows the pick up coil configuration relative to the magnetic field and the

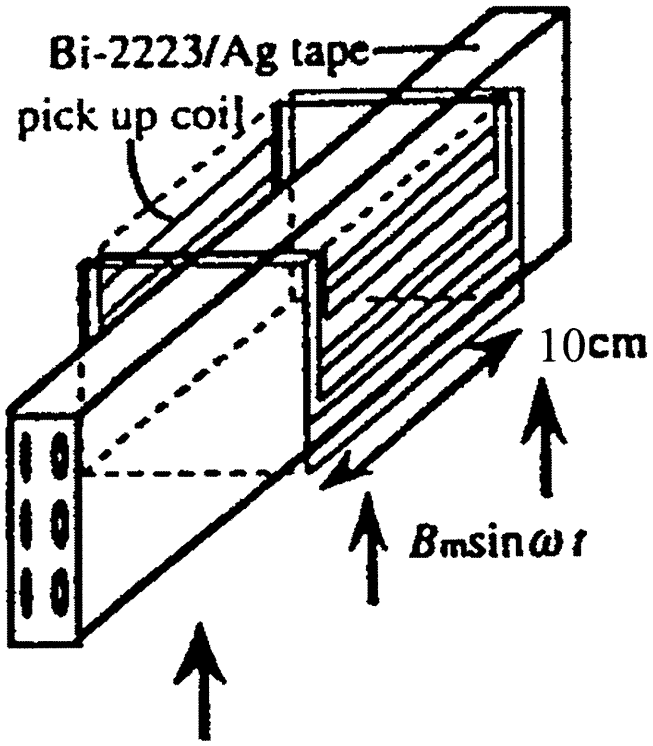

Figure 3.8 Pickup coil geometry for AC loss measurements.[22]

superconductor for the sample coil. The sample coil and the balancing coil should have the same geometry and configuration in the magnetic field in order to minimize the inductive background.

Fig 3.9 shows the winding pattern used for the pick up coils. First, four pins were placed on a wooden board in the four corners of a rectangle that was 5 mm tall and 100 mm long. Tape was placed with the sticky side up to hold the wire in place. The pick up coil winding started in the bottom left hand corner and proceeded clockwise around the rectangle. Great care was taken to ensure that the pick up coil wire was parallel to the rectangle sides and that there were no gaps between each turn. The sample coil was made with 20 turns of the copper wire, which gave it an h of 3.5 mm. The balancing coil

was made with 25 turns, which gave it an h of 4 mm. The extra length at the corners of the pick up coils was neglected and both coils are taken to have a length of 100 mm. When the pick up coils were finished and secured with tape, they were folded across the AD and BC lines to form the C-shape necessary for the measurements. Fig 3.10 shows a photograph of the sample coil mounted on a BSCCO-2223 sample and ready for measurements.

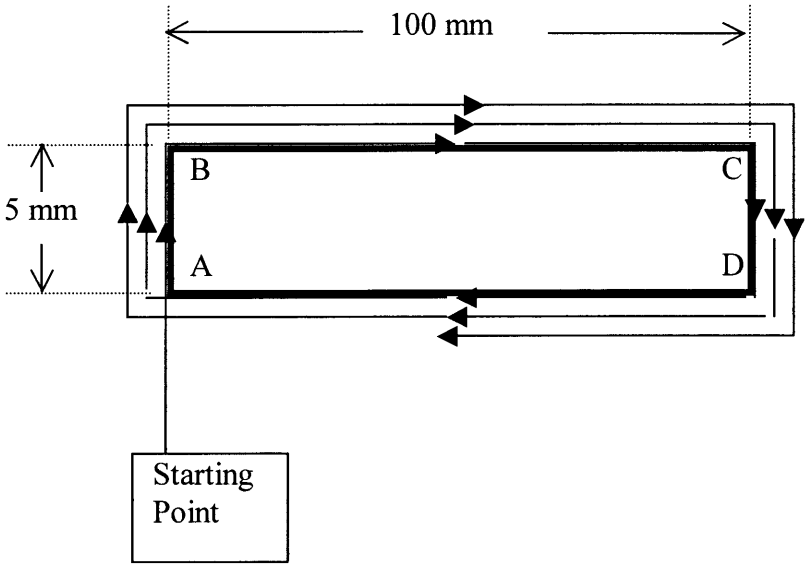

Figure 3.9 Winding pattern used for the pick up coil construction.

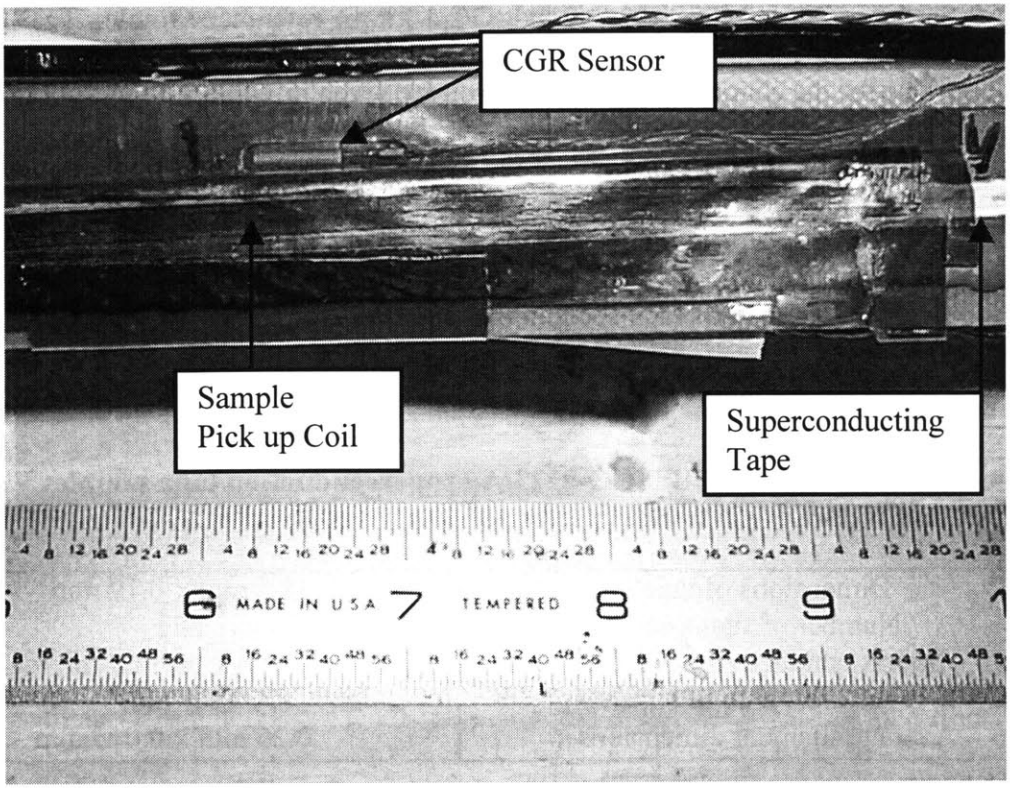

Figure 3.10 Sample pick up coil and sample mounted on the sample holder and ready for measurements.

3.5 Preparation of Sample

The HTS sample is the most important piece of the experiment as well as the most delicate. The samples were long lengths of BSCCO-2223/Ag sheathed tape superconductors. Two samples were provided by Vacuumschmelze GmbH (VAC) of Hanau, Germany. The two sample tapes had identical characteristics, but one was manufactured on an earlier date than the other. A reference sample manufactured by IGC was provided by Dr. M. Suenaga of Brookhaven National Laboratory (BNL). This sample is a reference sample because Suenaga has measured and reported properties of this conductor [24]. The samples are referred to as VAC-1 for the older VAC conductor,

VAC-2 for the newer VAC conductor, and IGC-1 for the reference sample. The specifications for the characteristics of the tapes are given in Table 3.1. Fig 3.11 is a photograph of the cross sectional view of the VAC-2 superconducting tape magnified 100 times. The BSCCO-2223 filaments suspended in the silver matrix are readily apparent and appear as the elongated black spots in the tape.

Table 3.1 Specifications of BSSCO-2223/Ag superconducting tape samples VAC-1, VAC-2, and IGC-1.

Dimensions of tape	3.5 mm x 0.19 mm
Number of filaments	56
Matrix conductivity at 77 K	$2.6 \times 10^{-9}\ \Omega \cdot m$
Total Cross sectional area of superconductor	$0.21\ mm^2$
Average filament dimensions	0.26 mm x 0.015 mm

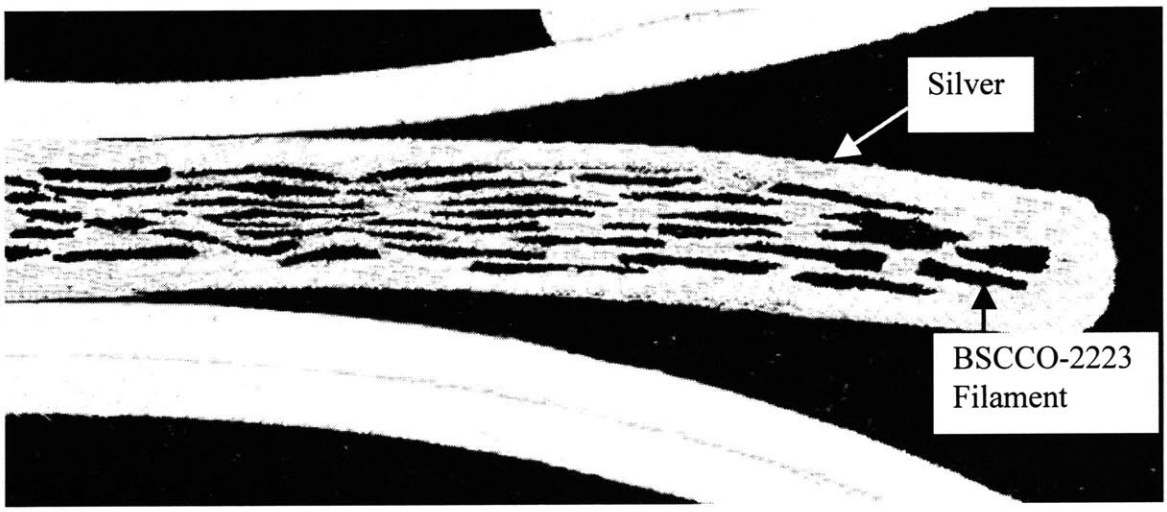

Figure 3.11 Cross sectional view of BSCCO-2223/Ag sheathed superconducting tape magnified 100 times.

The samples were cut into 300 mm lengths and Sty-cast® epoxy was used to glue the superconductor to 1 mm thick sheets of G-10. After the Sty-cast® cured, the superconductor was securely attached to the G-10 plate, which prevented it from moving. The effect of the Sty-cast® on the critical current was measured and compared to the critical current of a sample secured only by an adhesive tape. Since the critical currents were the same for both cases, it was concluded that the Sty-cast® did not affect the sample cooling or the critical current measurement by thermal strain. Therefore, all samples were glued to G-10 plates using Sty-cast®.

Copper voltage taps and current leads were soldered to the sample using 60% Sn/40% Pb solder. A photograph of the voltage taps connected to a sample is shown in Fig 3.12. The voltage taps were placed 100 mm apart over the middle of the sample and at least 38 mm from the nearest current lead. As explained earlier, a good connection between the sample and the current leads and voltage taps is important to reduce the contact resistance and heating at these locations. Therefore, the surface of the superconductor was cleaned using a razor in the areas where the voltage taps and current leads were connected. These areas were pre-tinned separately as were the current leads and voltage taps. The connection areas were kept clean to ensure a good connection and reduce any effects from the joint resistance.

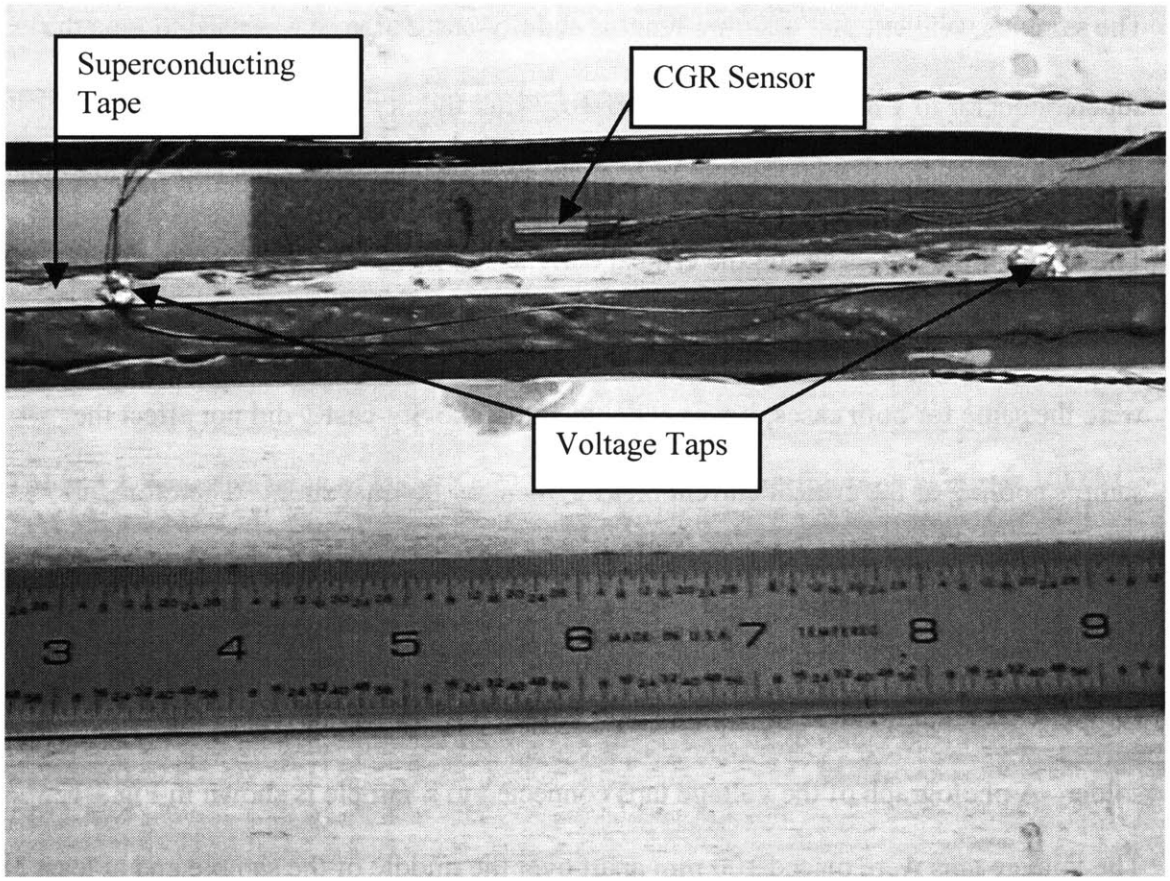

Figure 3.12 Prepared sample tape of BSCCO-2223/Ag tape mounted on the sample holder and ready for critical current measurements.

4 Results and Discussions

4.1 Critical Current Measurements

4.1.1 Magnetic Field Strength Effect

The critical current and n value as a function of magnetic field strength at 77 K for the VAC-1 and VAC-2 superconductors are shown in Fig 4.1 and Fig 4.2 for two different electric field criteria. The critical currents listed in Fig 4.1 were determined from an electric field criterion of 10 μV/m while the critical currents plotted in Fig 4.2 were determined from an electric field criterion of 100 μV/m. The magnetic field was oriented in-plane with the broad face of the tape. The data illustrates that the critical current is greatly reduced in the presence of an external magnetic field. The experimental data are fairly well described by a generalized Kim-like critical state model expressed in the following equation[26]

$$I_c(B) = \frac{I_c(0)}{\left[1+\left(\frac{B}{B_k}\right)^{\beta}\right]} \tag{4.1}$$

where $I_c(0)$ is the self-field critical current, and B_k and β are material parameters. The critical current measurements were corrected for self-field effects from the transport current by adding the magnetic field induced from the transport current to the external magnetic field. The magnitude of the magnetic field induced by the transport current was determined to be[16]

$$B = \frac{\mu_0 I}{2\pi a} \tag{4.2}$$

where B is the magnetic field, I is the transport current, and a is the distance from the current to the measurement point. The distance, a, was approximated by measuring the distance from the center of the cross-section to the outer surface of superconducting filaments. The distance was determined to be approximately 0.2 mm. Table 4.1 lists the values of $I_c(0)$, B_k, and β used in Eq (4.1) to develop a best fit to the measured data shown in Fig 4.1 and Fig 4.2.

The trend-lines of the critical current as a function of the external magnetic field strength developed from Eq (4.1) are accurate to within 5% of the experimentally determined critical currents. Substituting $\beta = 1$ into Eq (4.1) and multiplying the right-hand side of the equation by $\frac{B_k}{B_k}$ gives a form of the Kim model for critical current as a function of magnetic field which is very similar to Eq (2.22). This leads to the conclusion that

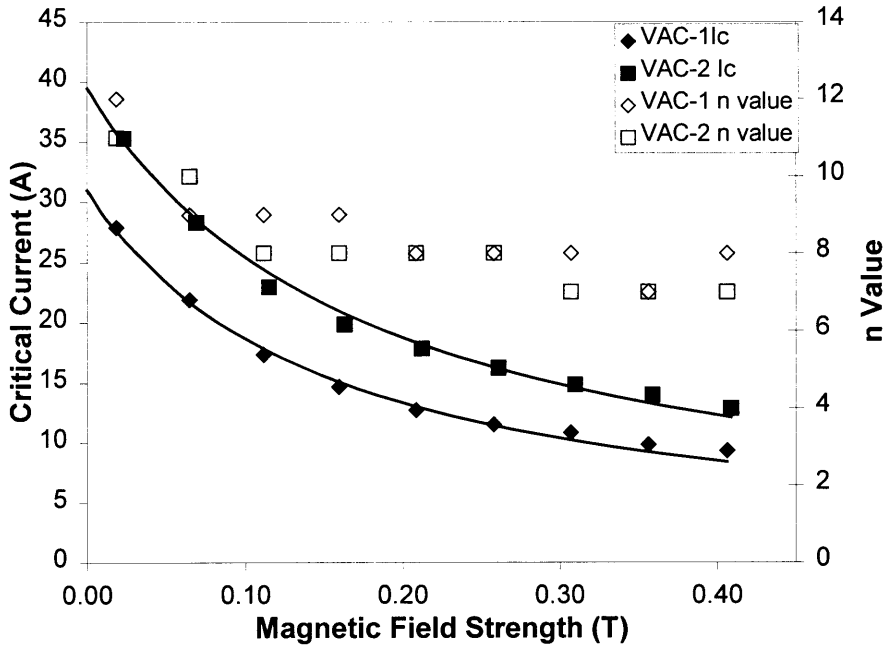

Figure 4.1 Critical current measurements of VAC-1 and VAC-2 samples as a function of magnetic field strength at 77 K determined from an electric field criterion of 10 μV/m. The magnetic field was oriented in-plane with the broad surface of the tape and perpendicular to the transport current flow.

$B_k = \frac{H_0}{\mu_0}$ and is the magnetic field strength that corresponds to the critical current that is approximately half of the self-field critical current. Fig 4.1 and Fig 4.2 show that the B_k parameters determined from the critical current measurements is indeed the approximate value of the magnetic field strength that corresponds with a critical current that is half of the self-field critical current.

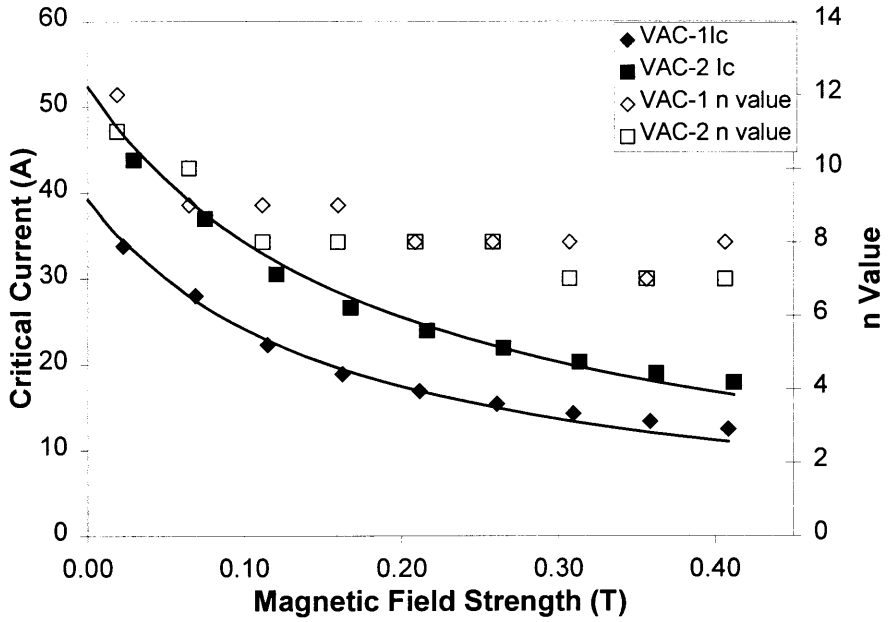

Figure 4.2 Critical current measurements of VAC-1 and VAC-2 samples as a function of magnetic field strength at 77 K determined from an electric field criterion of 100 μV/m. The magnetic field was oriented in-plane with the broad surface of the tape and perpendicular to the transport current flow.

Fig 4.1 and Fig 4.2 also illustrate the effect the electric field criterion has on the critical current measurements. The basic trend for each data set has the same experimental value for β, regardless of the electric field criteria used to determine the critical current. The B_k parameter differs by approximately 15% for the VAC-2 sample and 20% for the VAC-1 sample when the results from the different electric field criteria are considered, but this parameter does not affect the general trend of the critical current dependence on the magnetic field strength. Therefore, the electric field criterion only affects the magnitude of the measured critical current and does not affect the critical current reduction trend with increasing magnetic field.

Table 4.1 Parameters of the VAC-1 and VAC-2 tape superconductors determined from the measured critical currents as a function of in-plane magnetic field at 77 K.

Electric Field Criteria (μV/m)	Sample	$I_c(0)$ (A)	B_k (T)	β
10	VAC-1	31.0	0.15	1
10	VAC-2	39.5	0.18	1
100	VAC-1	39.2	0.16	1
100	VAC-2	52.3	0.19	1

The n value of the VAC samples is also shown in Fig 4.1 and Fig 4.2. The n value did not depend on the electric field criteria as it is related to the rate at which voltage appears as the current increases after the transition to the normal state. The n value changed approximately 30% from the self-field value to the n value measured at 0.4 T, which indicates a less rapid increase of voltage with increasing current at higher magnetic fields. The self-field n values for these BSCCO-2223 samples were on the order of 10 at liquid nitrogen temperatures. The higher n values reflect a rapid increase of the voltage as the current increases after the transition to the normal state.

It is also important to note that the upper critical magnetic field at 77 K for these samples was not determined from these experiments. The samples are still in the mixed state when the external magnetic field is at 0.4 T as seen in Fig 4.1 and Fig 4.2. It is impossible to determine the upper critical field mathematically from Eq (4.1) and, therefore, must be measured experimentally. The magnetic field strength of this particular experiment was limited to 0.4 T by limits on the voltage across the magnet power supplies. The EMHP power supplies had a safety feature that shut down the power supplies if the voltage exceeded 30 V. The resistance and inductance of the copper magnet induced a voltage large enough to trip and shut down the power supplies

as the magnetic field was charged to values barely above 0.4 T. Since the value was out of the range available for study, determining the upper critical magnetic field at 77 K was not in the scope of this experiment.

4.1.2 Magnetic Field Orientation Effect

The critical currents of the VAC-1 and VAC-2 wires were measured as a function of the orientation of the applied external magnetic field at 77 K. The external field was rotated in the range of 0 to ±90 degrees with respect to the broad face of the tape while keeping the magnitude at a constant 0.2 T. Fig 4.3 shows a diagram of the magnetic field orientation relative to the tape. The magnetic field was parallel to the broad face of the tape at an angle of 0° and perpendicular to the broad face at ±90°. The magnetic field was perpendicular to the transport current flow in all cases. All critical currents were determined using an electric field criterion of 10 μV/m. The results of this experiment

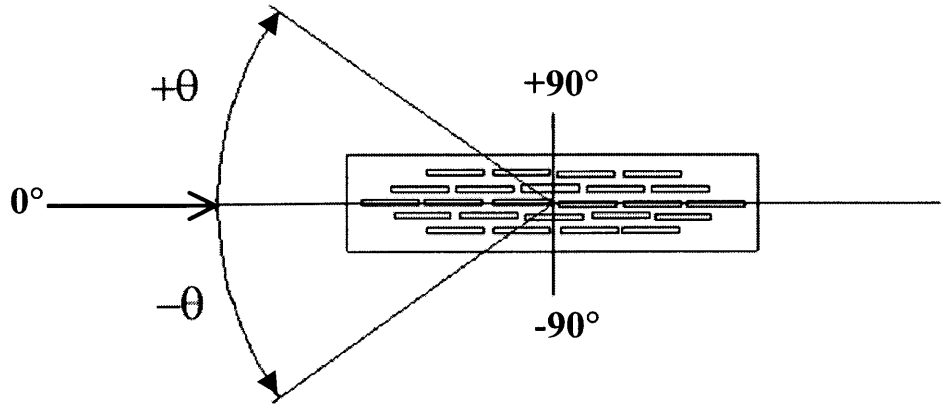

Figure 4.3 Angle labels for magnetic field orientation relative to the sample. 0° degrees corresponds to the magnetic field oriented in-plane with the broad tape face.

are shown in Fig 4.4. The anisotropic behavior of the BSCCO-2223 is readily apparent. The critical currents are at a maximum when the magnetic field is applied in-plane to the broad face of the tape. The critical current decreased by approximately 25% for each sample as the magnetic field angle deviated 15° from the in-plane orientation. When the magnetic field was perpendicular to the broad face, the critical current for each sample was at a minimum value, which was 75% lower than the in-plane measurement.

The n value was also sensitive to the magnetic field orientation. The n value was at a maximum value when the magnetic field was in-plane with the tape face and a minimum when the magnetic field was oriented perpendicular to the tape face. The n value decreased by approximately 50% from the maximum value for each sample.

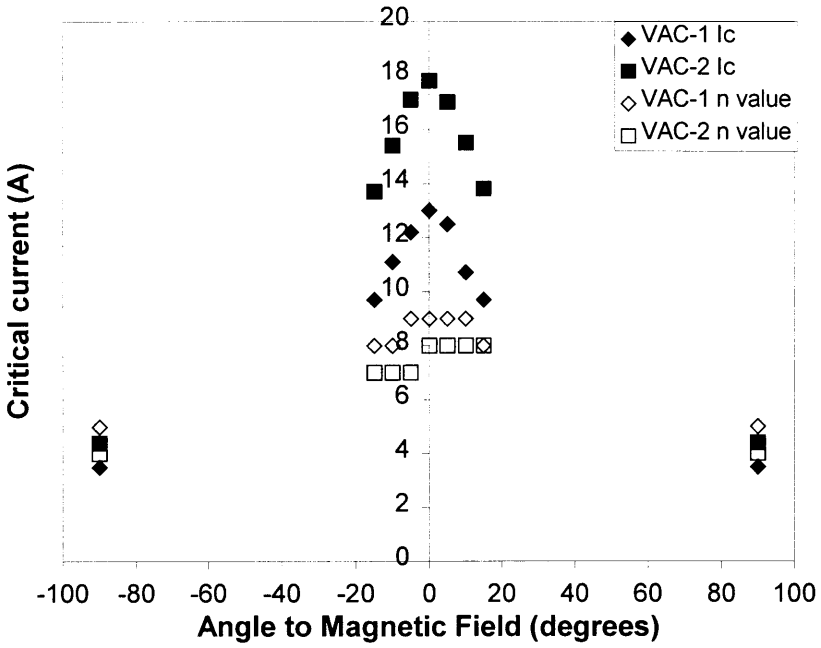

Figure 4.4 Critical current and n value as a function of magnetic field orientation at a constant strength of 0.2 T for VAC-1 and VAC-2 samples at 77 K. 0° corresponds to the magnetic field parallel with the broad face of the tape.

Fig 4.5 shows the critical current as a function of magnetic field strength with the magnetic field perpendicular to the tape face. The tests were performed at 77 K and the transport current flow was perpendicular to the external magnetic field at all times. All critical currents were determined using a 10μV/m electric field criterion. A curve fitting procedure utilizing Eq (4.1) gave the parameters for the samples listed in Table 4.2. The model is accurate within 5% for magnetic fields less than 0.2 T. However, as the magnetic field increases, the measured critical current decreases quicker than the model predicts.

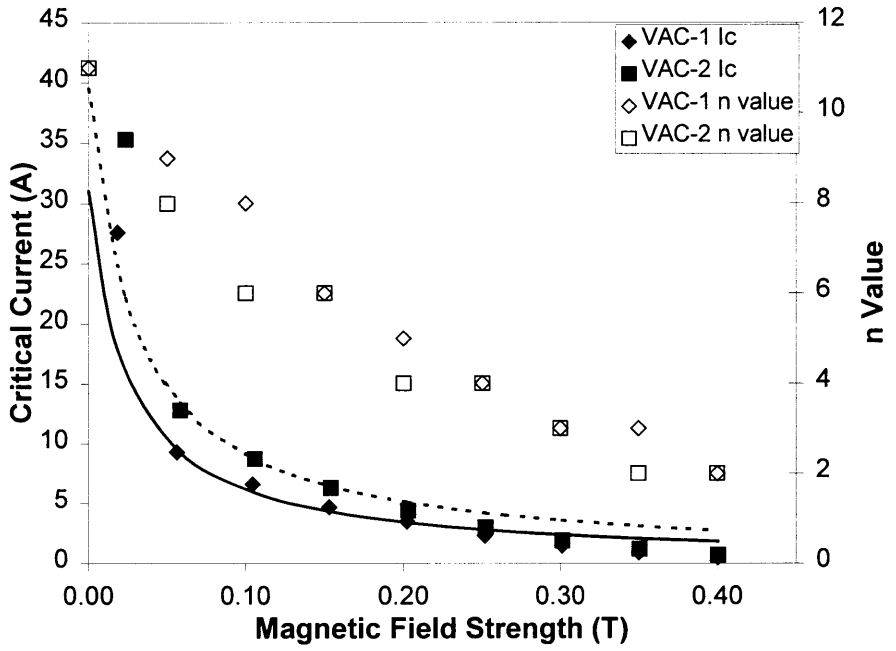

Figure 4.5 Critical current and n value as a function of magnetic field strength for VAC-1 and VAC-2 samples at 77 K with the magnetic field perpendicular to the broad face of the tape.

Fig 4.1 and Fig 4.5 illustrate the critical current as a function of magnetic field strength for the VAC-1 and VAC-2 samples subjected to similar conditions with the magnetic field oriented parallel and perpendicular to the tape face, respectively. The difference in the initial drop of the critical current is readily observed when comparing these plots. When the magnetic field is in-plane with the tape face, the critical current decreases smoothly until the critical field is reached and the superconductivity destroyed.

However, the critical current experiences a drastic initial drop at small magnetic field strengths when the magnetic field is perpendicular to the tape face. The difference is also apparent in the B_k property determined from the curve fitting procedure. The B_k values

Table 4.2 Parameters of the VAC-1 and VAC-2 tape superconductors determined from the measured critical currents as a function of magnetic field oriented perpendicular to the tape face at 77 K.

Electric Field Criteria (μV/m)	Sample	$I_c(0)$ (A)	B_k (T)	β
10	VAC-1	31.0	0.025	1
10	VAC-2	39.5	0.030	1

for the in-plane case are 10 times greater than the B_k values determined from the perpendicular case. The anisotropic behavior suggests the average pinning force per normal vortex is greater when the magnetic field is parallel to the broad face of the tape than when the magnetic field is perpendicular to the tape face. This behavior also suggests a weak link network as the dominant mechanism in transporting current. Therefore, the superconductivity is destroyed when the weakest pinned vortex begins to move.

The n value also decreased much more quickly when the magnetic field was oriented perpendicular to the tape face than when the magnetic field was oriented parallel with the tape face. The n values decreased by 30% when the magnetic field was increased from zero to 0.4 T and in-plane with the broad face of the tape while the n value decreased by almost 85% over the same magnetic field range with the magnetic field perpendicular to the tape face.

4.1.3 Temperature Effect

The effect of the sample temperature on the critical current was measured. Fig 4.6 and Fig 4.8 plot the critical current as a function of magnetic field strengths, and Fig 4.7 and Fig 4.9 plot the corresponding n values for the VAC-1 and VAC-2 samples over a temperature range from 77 K to 110 K. The magnetic field was oriented in-plane with the tape face and held constant over the measurement period. The critical currents were determined using an electric field criterion of 10 μV/m. Eq (4.1) was used to develop the solid lines in the figures, which determined the material parameters shown in Table 4.3. The curve fitting describes the data very well. The values calculated using Eq (4.1) are within 5% of the measured critical currents.

It is interesting to note that the basic relationship between the critical current and the magnetic field stays constant and only the magnitude decreases as the temperature increases. The B_k parameter of the material decreases as the temperature increases while the β parameter stays constant.

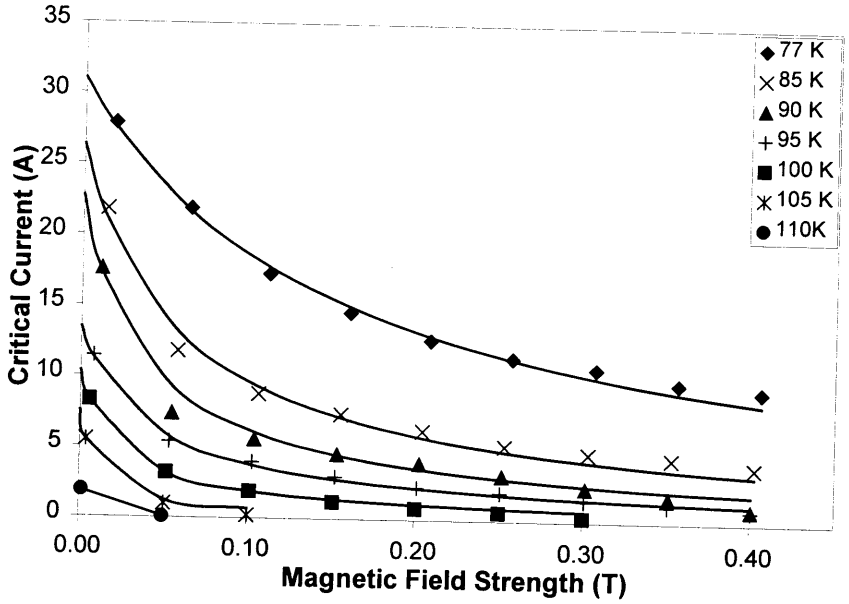

Figure 4.6 Critical current measurements as a function of magnetic field strength for the VAC-1 sample at varying temperatures. The magnetic field was in-plane with the tape face and the electric field criterion was 10 μV/m.

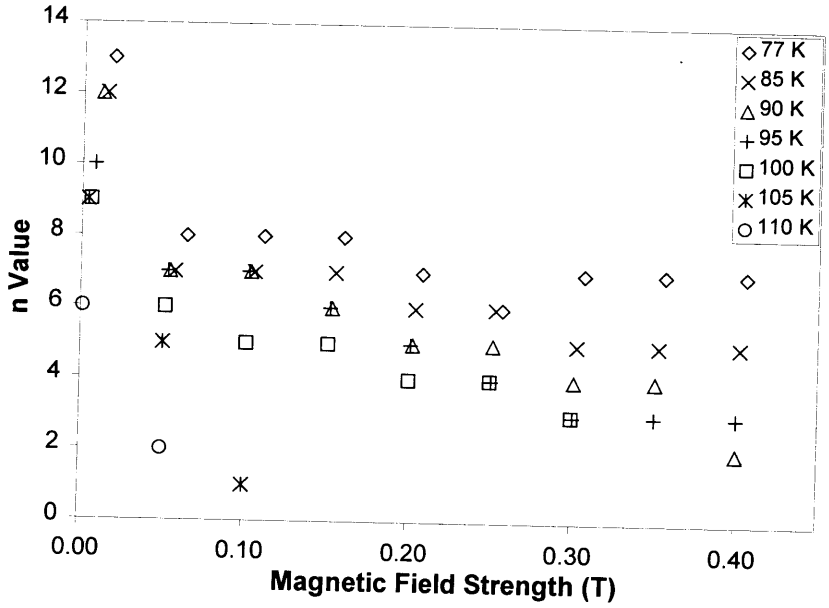

Figure 4.7 The n values as a function of magnetic field strength for the VAC-1 sample at various temperatures. The magnetic field was parallel to the tape face and the electric field criterion was 10 μV/m. These n values correspond to the critical currents plotted in Fig 4.5.

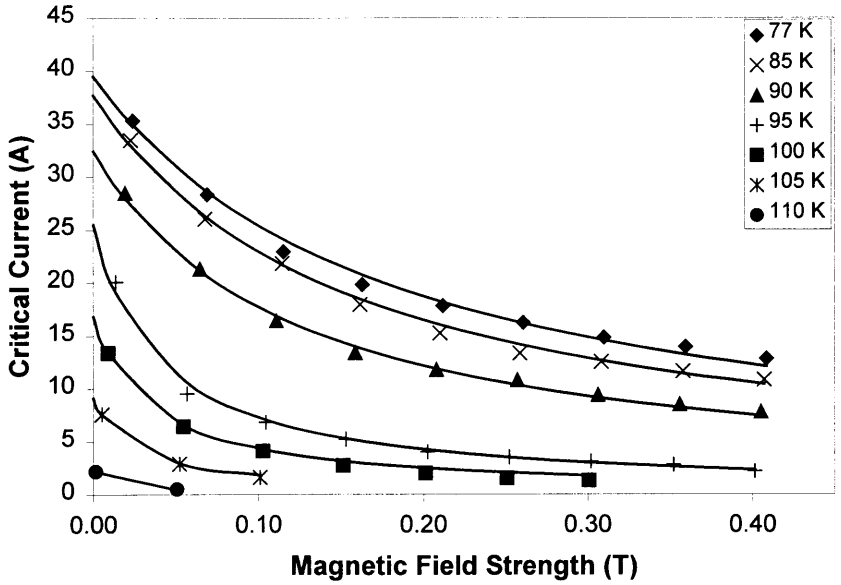

Figure 4.8 Critical current as a function of magnetic field strength for the VAC-2 sample at various temperatures. The magnetic field was in-plane with the tape face and the electric field criterion used to determine the critical current was 10 μV/m.

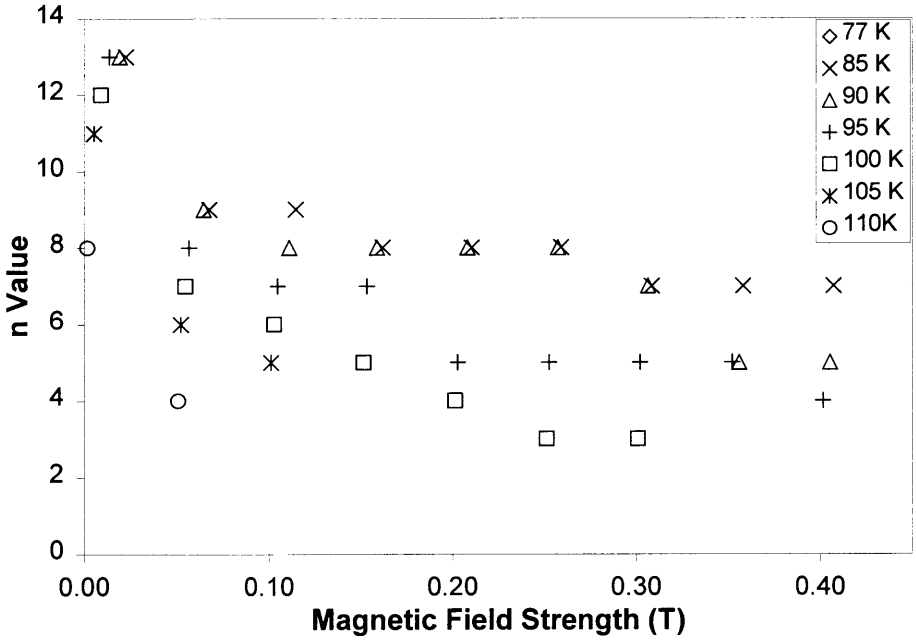

Figure 4.9 The n values as a function of magnetic field strength for the VAC-2 sample at various temperatures. The magnetic field was parallel to the tape face and the electric field criterion was 10 μV/m. These n values correspond to the critical currents plotted in Fig 4.7.

Table 4.3 Parameters of the VAC-1 and VAC-2 tape superconductors as a function of temperature. The parameters were determined from the measured critical currents as a function of the in-plane magnetic field strength at each temperature.

Temperature (K)	VAC-1			VAC-2		
	$I_c(0)$ (A)	B_k (T)	β	$I_c(0)$ (A)	B_k (T)	β
77	31.0	0.150	1	39.5	0.180	1
85	26.3	0.058	1	37.7	0.155	1
90	22.7	0.040	1	32.4	0.120	1
95	13.4	0.038	1	25.5	0.040	1
100	10.3	0.023	1	16.8	0.035	1
105	7.5	0.010	1	9.1	0.025	1
110	4.2	0.001	1	2.5	0.010	1

A comparison of the VAC-1 critical currents to the VAC-2 critical currents immediately leads to the observation of the superior critical currents of the VAC-2 conductor to the critical currents of the VAC-1 conductor at all magnetic fields over the temperature range, but the critical temperature of both samples was the same value at approximately 113 K. The higher values of the critical current are reflected in the higher B_k parameters of the VAC-2 conductor. Also, the critical currents drop off with increasing magnetic field at the same rate over the temperature range. This is reflected in the constant value of β for each measurement.

Also, the critical currents of the VAC-2 superconductor do not degrade with temperature as quickly as the VAC-1 superconductor. The B_k property for the VAC-1 superconductor changes over 60% from 77 K to 85 K. This drastic decrease in B_k correlates to a 20% decrease in the critical currents for the VAC-1 sample for this temperature step. By contrast, the B_k parameter of the VAC-2 superconductor does not decrease more than 60% until the temperature reaches 95 K. The self-field critical current of the VAC-2

superconductor decreased 43% from 77 K to 95 K while the self-field critical current of the VAC-1 superconductor decreased almost 60% over the same temperature step.

The critical surfaces of the VAC-1 and VAC-2 samples were constructed using this data. The plots of the surfaces are shown in Fig 4.10 for the VAC-1 sample and Fig 4.11 for the VAC-2 samples. The critical currents were determined for magnetic fields oriented parallel to the broad face of the tape at an electric field criterion of 10 μV/m. The surface represents the boundary between the normal state and the superconducting state. When the temperature and magnetic field fall underneath the curve, the sample is in the superconducting state. It is easily seen that the VAC-2 critical values are approximately 20% larger than the critical values of the VAC-1 conductor. Material degradation over time, non-uniformity over conductor length, and improved conductor manufacturing are all possible reasons for the improved properties of the VAC-2 superconductor as compared to the VAC-1 superconductor.

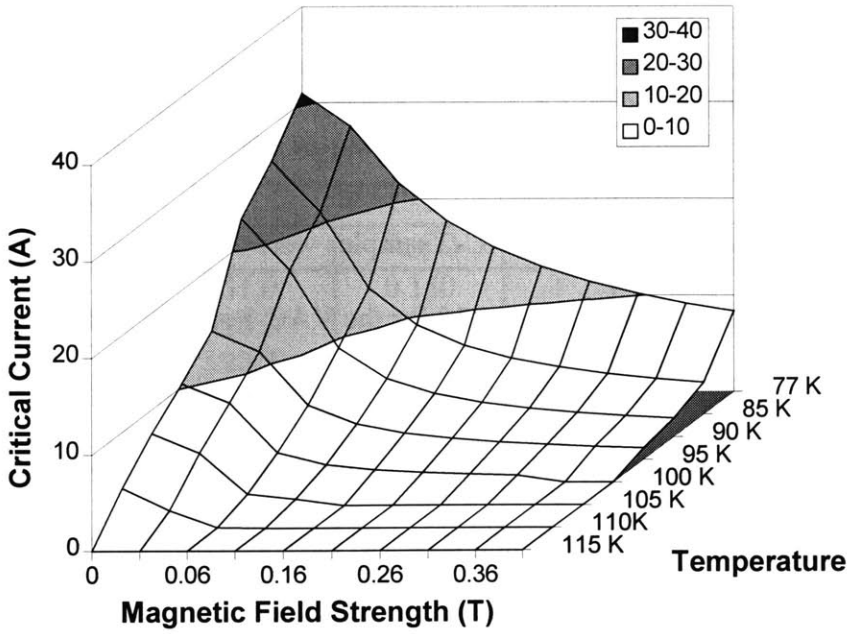

Figure 4.10 Critical surface for the VAC-1 conductor for the magnetic field oriented in-plane with the tape face at E = 10 μV/m.

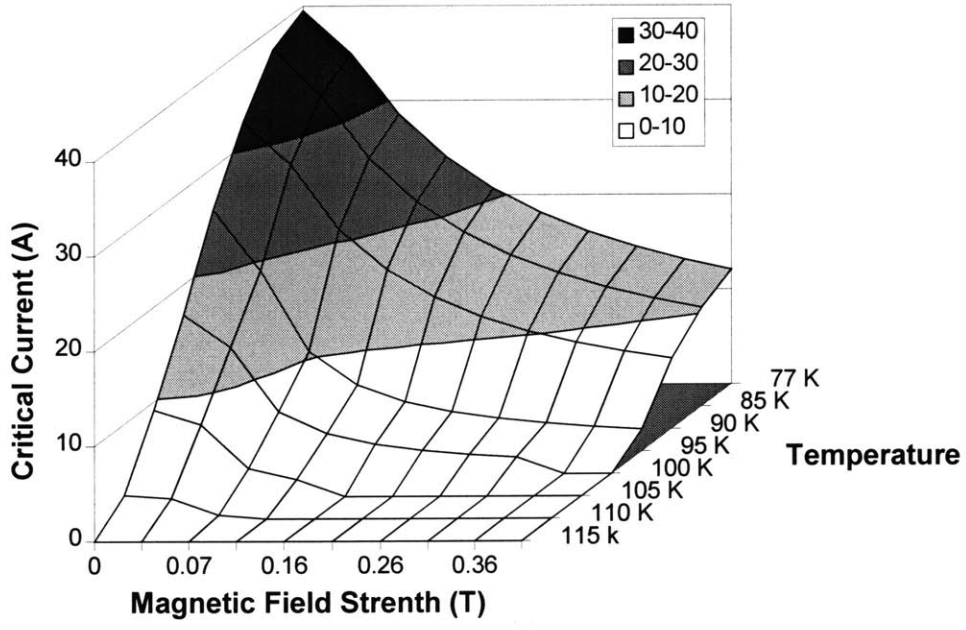

Figure 4.11 Critical surface for the VAC-2 conductor for the magnetic field oriented in-plane with the tape face at E = 10 μV/m.

4.1.4 Current Ramp Speed Effect

The effect of the transport current ramp speed on the critical current measurement was investigated. The critical current of the VAC-1 and VAC-2 superconductors was measured over a range of 6 A/min to 120 A/min without an external magnetic field and in the presence of an external DC magnetic field of 0.2 T. The magnetic field was in-plane with the tape face, and the sample temperature was 77 K for all tests. The critical currents were determined using an electric field criterion of 10 μV/m. Fig 4.12 shows the critical currents as a function of the transport current ramp speed for the VAC-1 and VAC-2 samples. The critical currents are within 2% of the initial measurement for each case. Therefore, it was assumed that the transport current ramp speeds typical of these experiments had no effect on the critical current measurements.

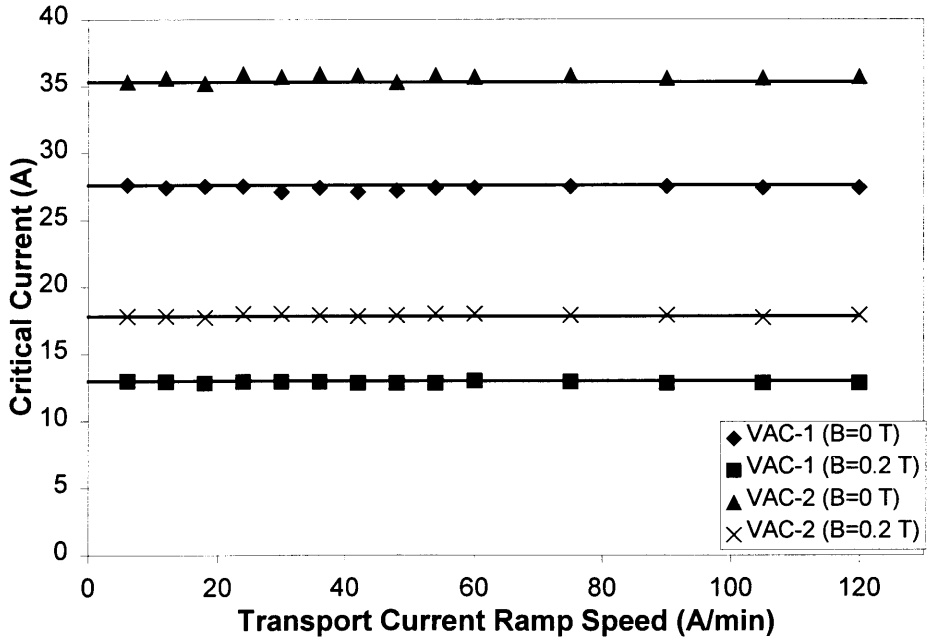

Figure 4.12 Effect of current ramp speed on the critical current measurements for the VAC-1 and VAC-2 samples at 77 K. The experiments were performed in the absence of a magnetic field as well as with an external DC magnetic field of 0.2 T oriented in-plane with the tape face.

4.2 AC Losses

4.2.1 Effect of Magnetic Field Amplitude

The AC losses as a function of the amplitude of the peak magnetic field were measured for two superconductors. The AC loss is the energy dissipated per unit volume of total superconductor volume per cycle. All tests were performed at 77 K, and the magnetic field was oriented parallel to the broad face of the tape. Fig 4.13 shows a trace of the alternating external magnetic field used for all the AC loss experiments. The period, T, was related to the frequency as shown in Eq (3.10).

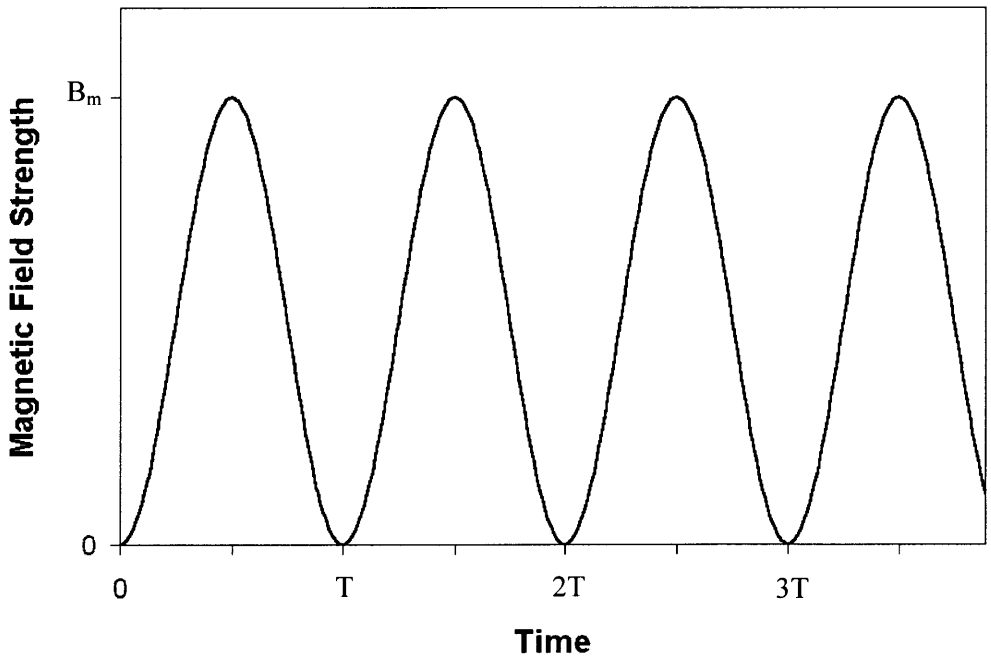

Figure 4.13 Magnetic field profile of the external magnetic field applied to the superconductor for the AC loss measurements.

To investigate the effect of increasing magnetic field on the AC losses, the peak magnetic field, B_m, was set to values of 0.10, 0.15, 0.20, 0.25, 0.30, 0.35, and 0.38 T and oscillated at a frequency of 0.093 Hz. The AC losses were measured using the pick up coil technique and plotted with the theoretical calculations of the AC loss estimates based on the critical current measurements for the VAC-2 sample. The critical current as a function of magnetic field and AC losses as a function of peak magnetic field for the IGC-1 sample at a magnetic field sweep frequency of 60 Hz were previously measured by Dr. M. Suenaga at the Brookhaven National Laboratory [24]. The $I_c(0)$ and B_k parameters for the IGC-1 sample determined by Dr. Suenaga were the values used for the theoretical calculations from the AC loss models. The parameters for the IGC-1 sample are given in Table 4.4.

The theoretical calculations were performed using the measured $I_c(0)$ values to determined the critical current density of each sample. Then the hysteresis loss density was calculated using Eq (2.21) and Eq (2.26) for two cases. The first case assumed the superconducting filaments were completely uncoupled and is called the multifilament case. The second case assumed complete electromagnetic coupling of the

Table 4.4 $I_c(0)$ and B_k parameters at 77 K for the IGC-1 sample that were determined by Dr. Suenaga.[22]

Sample Name	$I_c(0)$ (A)	B_k (T)
IGC-1	25	0.100

superconducting filaments and is called the single core case. The significance of the coupled filaments to uncoupled filaments appeared in the half-thickness of the slab, a.

For the multifilament case, each filament was assumed to act independently with respect to the magnetic field. Therefore, the filaments were assumed to be unshielded from the magnetic field and the half-thickness of the slab was taken as the half-thickness of a single filament. For the single core case, the filaments were assumed to be completely coupled due to the alternating magnetic field and were assumed to behave as a monofilament superconductor. The dimensions of the monofilament were determined by assuming all the matrix within the outermost filament bundle was negligible and then measuring the physical dimensions. Fig 4.14(a) and (b) show conceptual drawings for the multifilament and single core cases. Table 4.5 lists the effective dimensions for the superconducting slab used to determine the penetration field for the multifilament and single core cases.

Table 4.5 Effective slab dimensions for the mulifilament case and the single core case.

Case	d (mm)	2a (μm)
Multifilament	0.26	15
Single Core	3.20	7.5

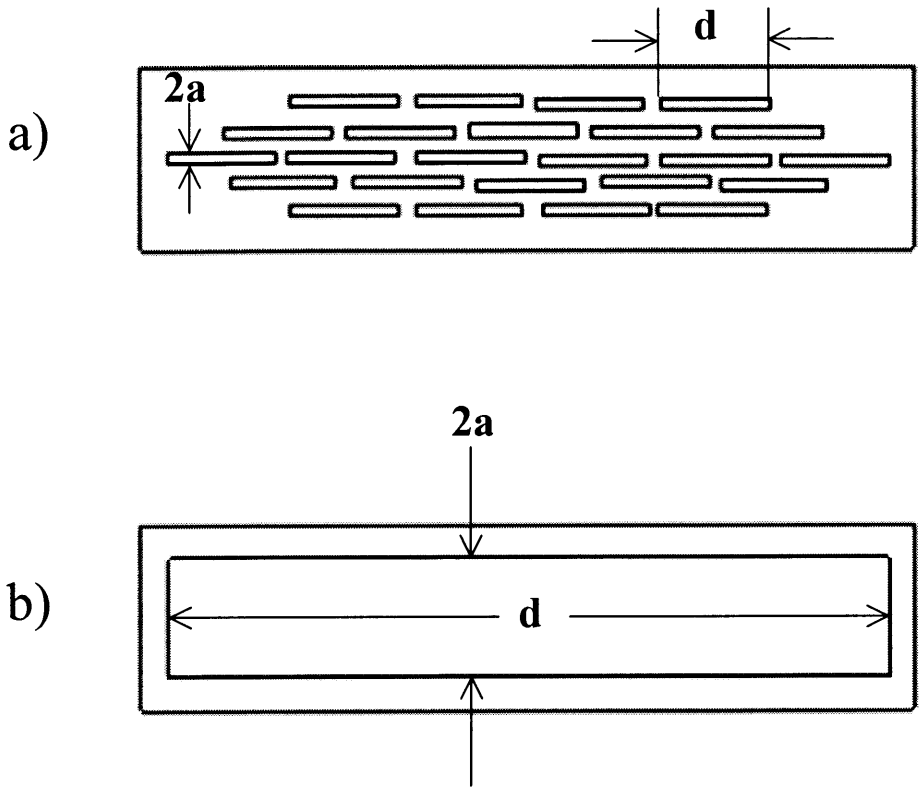

Figure 4.14 Illustration of the change in slab thickness between the multifilament case and the single core case.

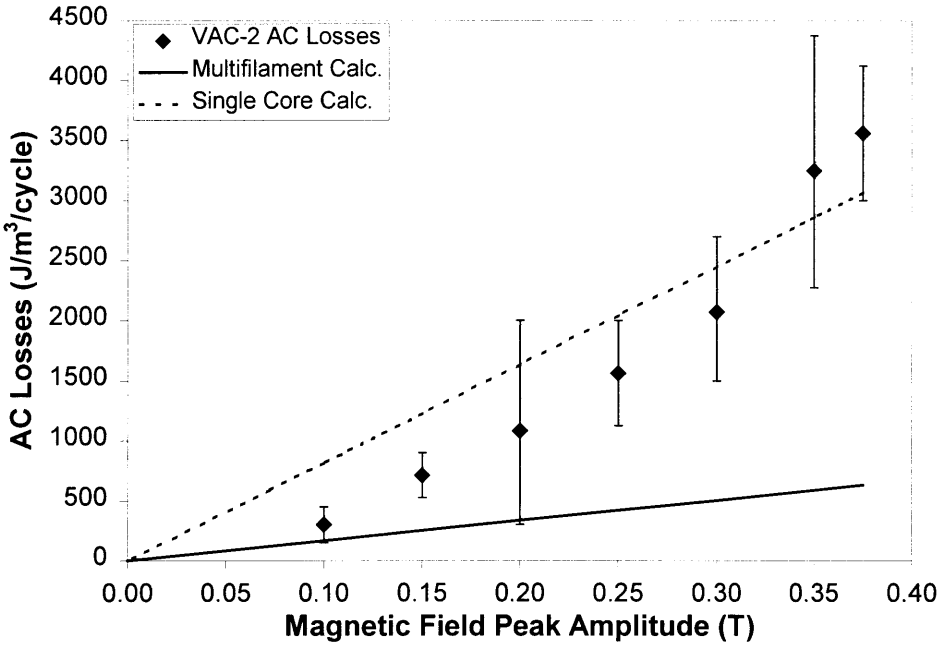

Figure 4.15 AC losses as a function of magnetic field amplitude at a frequency of 0.093 Hz at 77 K for the VAC-2 sample. The magnetic field was parallel to the tape face.

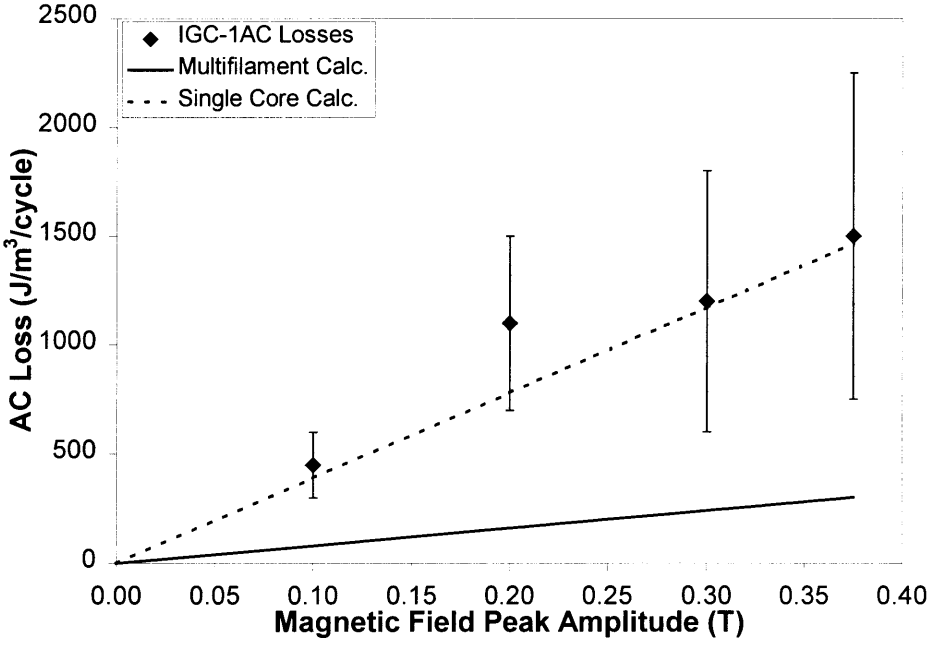

Figure 4.16 AC losses measured as a function of magnetic field amplitude at a frequency of 0.093 Hz at 77 K for the ICG-1 sample.

According to the Bean model and Eq (2.21), the AC losses increase linearly with increasing peak magnetic field after the superconductor is fully penetrated. Fig 4.15 plots the AC losses measured for the VAC-2 superconductor as a function of the peak magnetic field, and Fig 4.16 plots the AC losses as a function of the peak magnetic field for the IGC-1 sample. The theoretical calculations determined from the critical current measurements and Eq (2.21) are also shown for both cases.

The Bean model approximation for the single core case for the VAC-2 sample was within 20% of the measurements made at magnetic field strengths of 0.30 T and greater while the measurements below 0.30 T were more than 30% lower than the values calculated. The Bean model approximation for the multifilament case, however, was only within 50% of the theoretical model for the 0.10 T measurement while the rest of the measurements were greater than 60% less than the theoretical value. The theoretical values calculated for the IGC-1 sample for the single core filament case were all within 30% of the measured AC losses. The 0.30 T and the 0.40 T measurements were within 2% of the theoretical calculations determined from the Bean model for this case. The multifilament case for the IGC-1 sample was not as accurate as the single core case as all the measurements were more than 80% less than the measured losses. The Bean model was more accurate when the peak magnetic field was greater. The increased accuracy is a result of the critical current dependency of the magnetic field. As seen in the critical current data plots, the critical current is relatively constant at fields greater than 0.20 T. As the magnetic field was increased to higher peak values, the sample was subjected to a longer time span in the magnetic field regime where the critical current is relatively flat

compared to the initial drop in critical current. Thus, the Bean model approximation is more accurate when the assumption of constant critical current density holds, which occurs at higher magnetic fields.

The Kim model predicted that the AC losses increased with the natural log of increasing peak magnetic field. Fig 4.17 shows a plot of the AC losses as a function of peak magnetic field measured for the VAC-2 superconductor with the theoretical calculations for both cases determined from the critical current measurements and Eq (2.26). Fig 4.18 shows a plot of the AC losses as a function of peak magnetic field with the theoretical calculations for both cases determined from the critical current measurements by Suenaga and Eq (2.26).

The Kim model approximation for the single core case was within 15% for the measured AC losses at 0.25 T and below for the VAC-2 sample. At higher fields, the percent difference between the measured losses and the Kim approximation increased to 30% at 0.30 T and 50% for magnetic fields higher than 0.30 T. The measured AC losses for the IGC-1 sample, however, were more than 40% less than the single core Kim model approximation. The Kim model approximation for the multifilament case was between 50 and 90% less than the measured losses for the VAC-2 superconductor and was approximately 90% less then the measured losses for the IGC-1 sample. As seen in the plots, the Kim model was more accurate at the lower magnetic fields when the critical current was greatly reduced by small increases in the magnetic field, but the shape of the experimental data is not the same as that predicted by the Kim model.

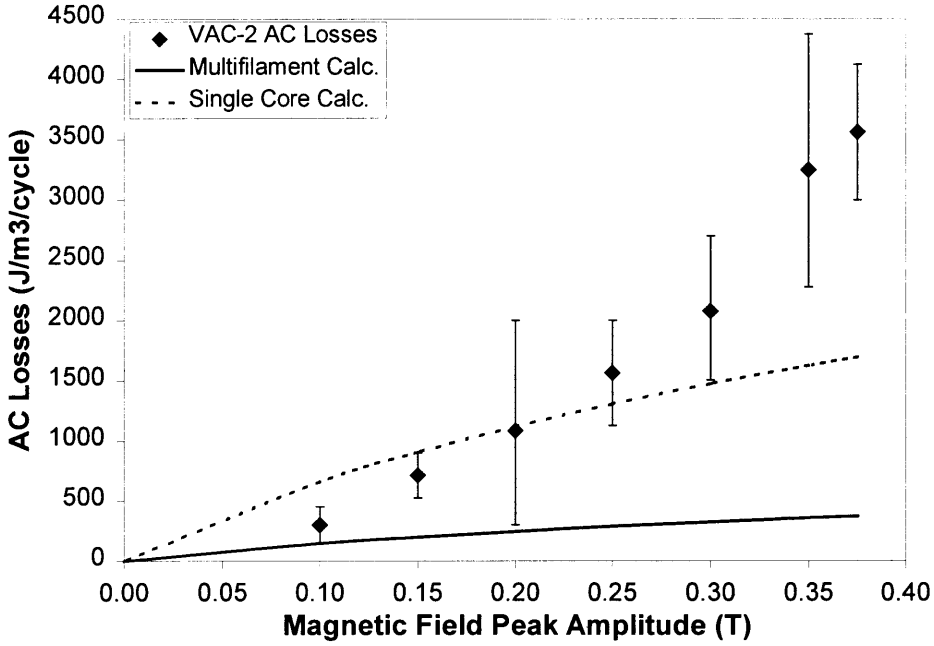

Figure 4.17 AC losses as a function of magnetic field amplitude at a frequency of 0.093 Hz at 77 K for the VAC-2 sample. The magnetic field was parallel to the tape face.

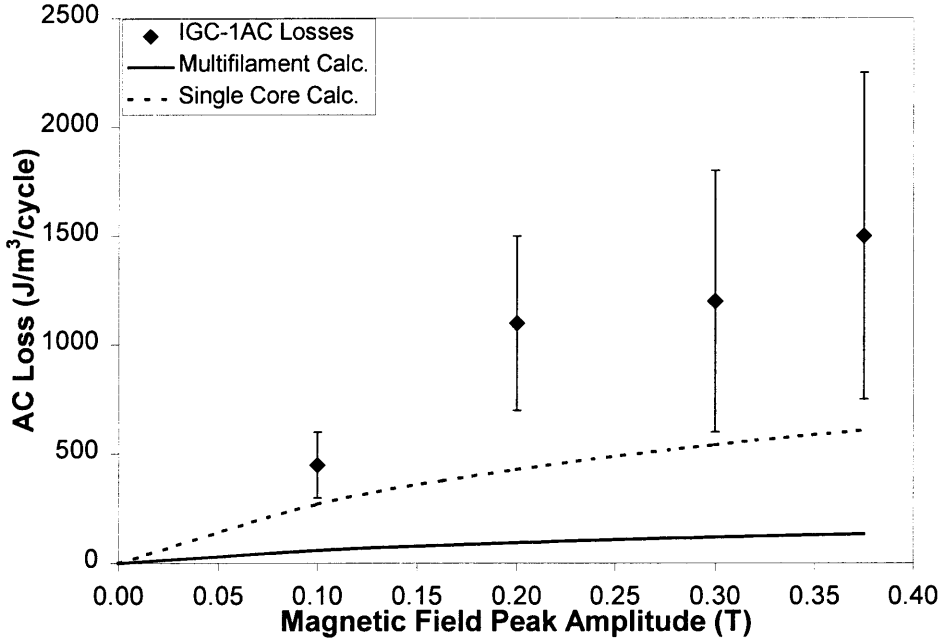

Figure 4.18 AC losses measured as a function of magnetic field amplitude at a frequency of 0.093 Hz at 77 K for the ICG-1 sample.

Both the Bean model and Kim model displayed a higher degree of accuracy when the calculations were performed assuming that the filaments were electromagnetically coupled and behaved as a monofilament core. However, the differences between the theoretical models and the measured values were not only attributed to the effect of the electromagnetic coupling of the filaments on the slab thickness. Kwasnitza, et al, [23] and Suenaga [24] have observed a factor of 2 difference between the critical currents measured from a typical four terminal method, such as the method presented in this thesis, and the critical current determined from AC loss measurements. This discrepancy is well documented for samples at 15 Hz and 60 Hz and is believed to originate from two sources.

One source is the effect of the perpendicular component of the magnetic field on the critical current measurements. During the critical current measurements, a transport current is passed through the sample and increased until the critical current is reached and exceeded. This transport current induces a magnetic field. The induced magnetic field has a component perpendicular to the tape face. This component strongly influences the critical current as shown in Fig 4.5. The AC loss measurements were performed without transport current and the external magnetic field was oriented parallel to the tape face. Therefore, the currents in the samples were magnetically induced from the alternating magnetic field and there was no component perpendicular to the tape face. The critical current measurements do not reflect the true value of the critical current in a purely parallel magnetic field as in the case of the AC loss measurements. It has been shown by

Suenaga, et al [24], and by Spreafico, et al [26], that the self-field critical current is 1.5 times greater when the perpendicular component of the self-field is minimized.

The second source of the critical current discrepancies comes from the behavior of the superconducting filaments. For long samples, the filaments of a multifilamentary superconductor tape are electro-magnetically coupled at low frequencies and act as a monofilament.[22,23] From Eq (2.26), the time constant for the decay of the coupling currents increases with the square of the length of the filaments and is on the order of 1000 s for the samples used in this experiment. Thus, the cracks and other physical damage from bending to the superconducting filaments do not strongly influence the AC loss measurements as they do the critical current measurements. The effect of the coupling currents on the hysteresis loss measurement has been investigated by Kwasnitza, et al [23]. They have shown that twisting the filaments is insufficient to effectively de-couple the filaments in high temperature superconductors and reduce the losses at frequencies of 50 Hz to a tolerable level. Twisting the filaments also reduces filament bridging and long paths of superconductivity cannot be manufactured. However, introducing a high-resistive barrier between the superconducting filaments and the silver matrix increases the effective matrix resistivity. The increased resistivity decreases the coupling current decay time and, hence, reduces the AC losses of the sample.[22,23]

4.2.2 Effect of Frequency

The AC losses as a function of the magnetic field sweep frequency at 77 K were measured for the VAC-2 and IGC-1 samples. The external magnetic field was alternating as shown in Fig 4.13 and oriented parallel with the broad face of the tape. The peak magnetic field was set at 0.35 T while the frequency was adjusted to values of 0.057, 0.073, 0.093, 0.110, and 0.130 Hz. Fig 4.19 plots the AC losses measured for the VAC-2 superconductor as a function of the magnetic field sweep frequency with the Bean model approximation for both cases, and Fig 4.20 plots the AC losses as a function of the magnetic field sweep frequency for the IGC-1 sample with the Bean model approximation for both cases. Fig 4.21 and Fig 4.22 show the plots of the AC losses as a function of the magnetic field sweep with the Kim model approximation for the VAC-2 and IGC-1 superconductors, respectively.

The theory states that the hysteresis loss per cycle is not a function of the sweep frequency, and, therefore, the measured losses should be a constant value for each frequency. Both models predict a straight line for the AC losses for each sample. The Bean model for the single core case was within 30% of the measured AC loss values for both the VAC-2 and the IGC-1 samples while the multifilament case underestimated the losses by about 80% for both samples. The Kim model for the single core case was more than 50% less than the measured values while the multifilament case Kim model was about 90% less than the measured values for the VAC-2 sample. For the IGC-1 sample, the Kim model for the single core case was more than 60% less than the measured values

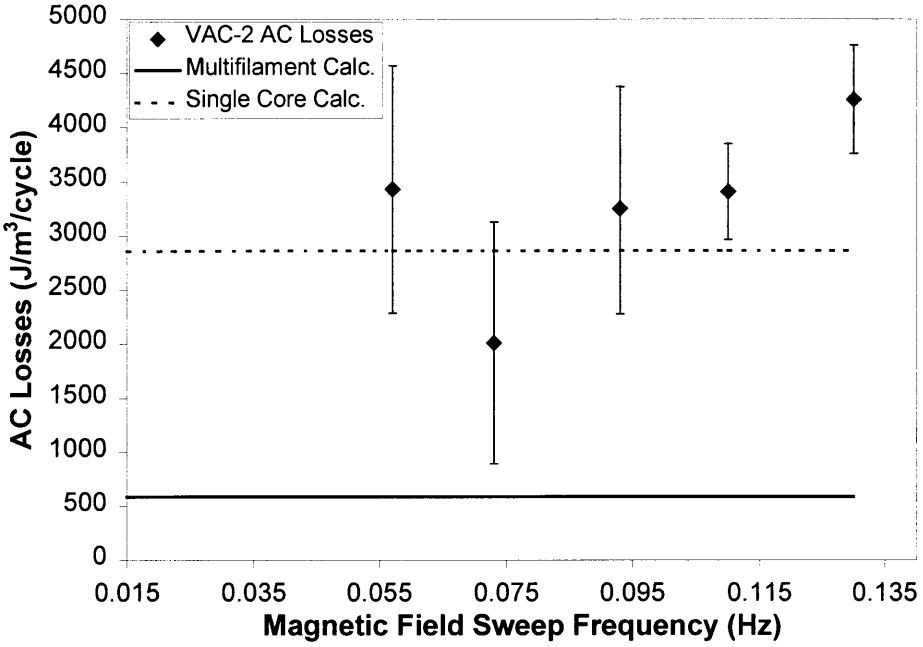

Figure 4.19 AC losses versus frequency of external AC magnetic field oriented in-plane with the tape face with a maximum peak field of 0.35 T at 77 K for the VAC-2 sample with Bean model approximation.

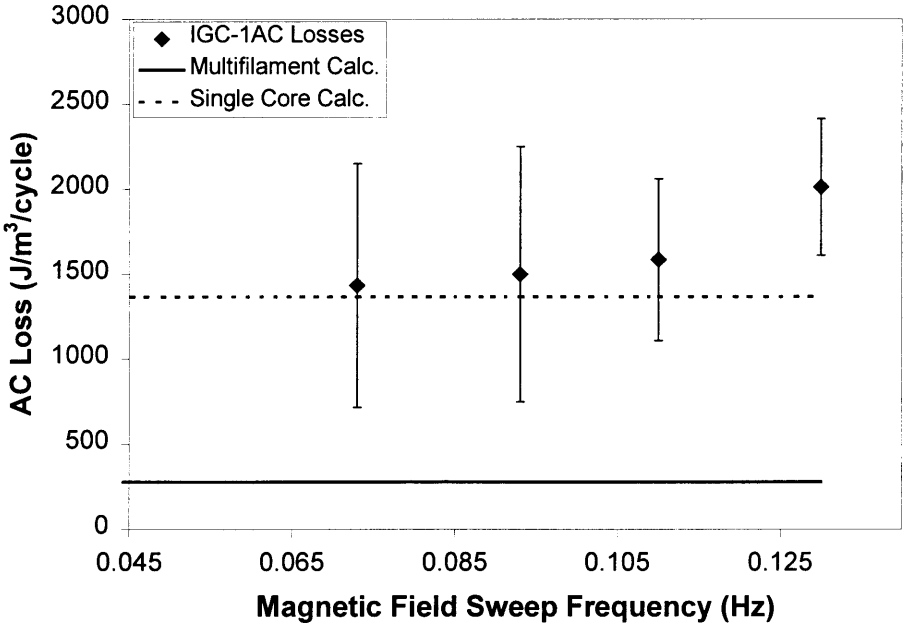

Figure 4.20 AC losses versus frequency of external AC magnetic field oriented in-plane with the tape face with a maximum peak field of 0.35 T at 77 K for the IGC-1 sample with Bean model approximation.

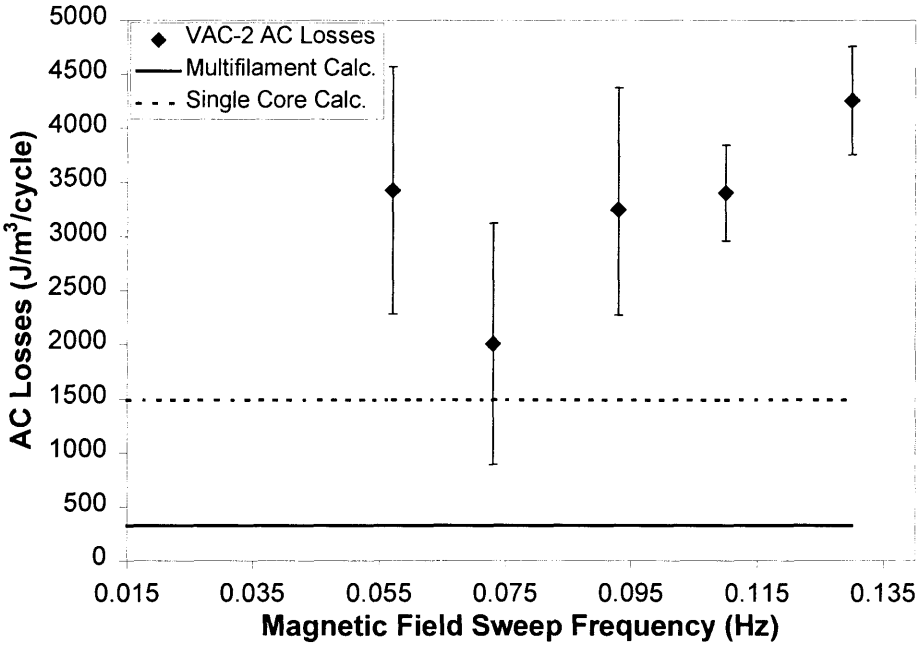

Figure 4.21 AC losses versus frequency of external AC magnetic field oriented in-plane with the tape face with a maximum peak field of 0.35 T at 77 K for the VAC-2 sample with Kim model approximation.

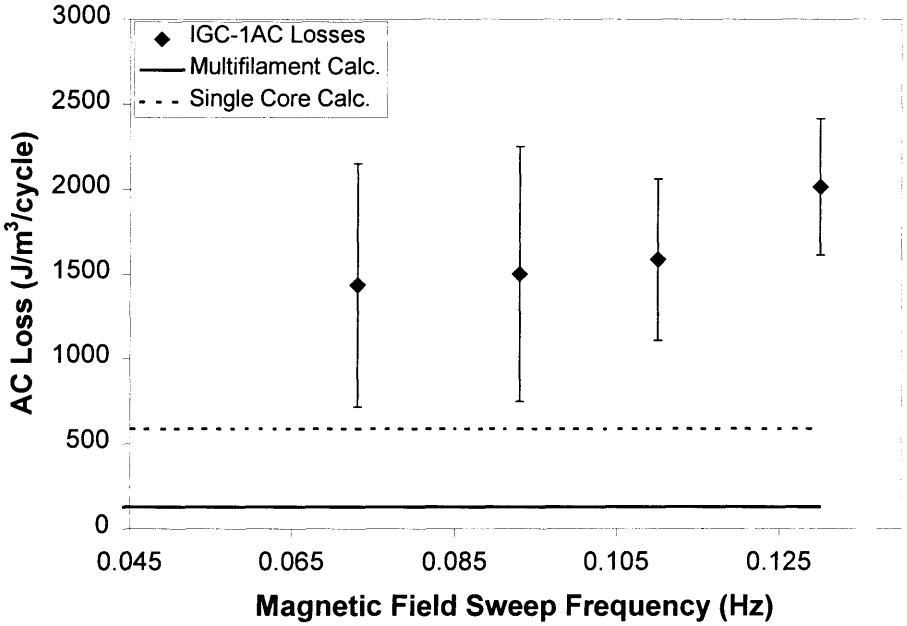

Figure 4.22 AC losses versus frequency of external AC magnetic field oriented in-plane with the tape face with a maximum peak field of 0.35 T at 77 K for the IGC-1 sample with Kim model approximation.

while the multifilament case Kim model was about 90% less than the measured values for the VAC-2 sample. The result of the single core Bean model case as the most accurate was consistent with the results of the previous section since all AC loss measurements were performed with a peak magnetic field of 0.35 T, which is in the regime of relatively constant critical current.

4.2.3 Effect of Transport Current

The effect of DC transport current on the AC losses was measured for a fixed magnetic field sweep frequency and peak magnetic field amplitude. The magnetic field was alternated as shown in Fig 4.13 and was oriented in-plane with the broad face of the tape. The peak magnetic field was 0.35 T, and the frequency was 0.093 Hz while the transport current was increased from 0 to 90 A in 10 A increments. The temperature was 77 K.

Fig 4.23 shows a plot of the AC losses as a function of transport current for the VAC-2 sample in an alternating magnetic field with a peak of 0.35 T and a sweep frequency of 0.093 Hz at 77 K. Using Eq (2.29), a curve was fit to the experimental data using an I_c of 52.3 A for both the multifilament case and the single core case. The multifilament case underestimates the AC losses by about 80% at the best place, 0 A, and about 98% at the worst place, 40 A. For the single core case, however, the AC loss measurements are within 15% for the measurements between 0 A and 20 A. The percent difference between the measured losses and the calculated values increases to 30% at 30 A, 62% at 40 A, and 88% at 50 A. The measured losses are practically constant and close to zero for transport currents of 60 A and higher. The disappearance of the AC losses at currents

higher than 52.3 A was expected because the sample reverted back to the normal state and the superconductivity destroyed when the critical current was exceeded. The general reduction trend described by Eq (2.29) is readily observed in Fig 4.23. The transport current reduces the flux free area and the penetration depth in the process. The lower penetration depth reduces the penetration field and, hence, the AC losses are reduced.

The reader is reminded that only the contribution from the magnetization loss was measured in this experiment. Therefore, the losses decreased as the current increased. However, the total losses due to a superconductor carrying a DC transport current

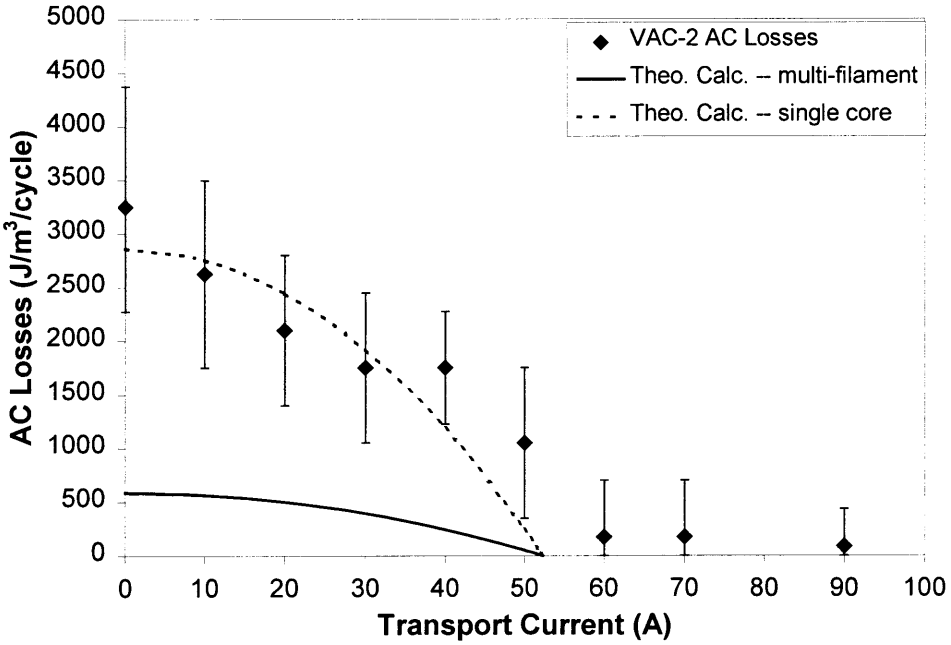

Figure 4.23 AC losses as a function of transport current in an alternating external magnetic field at a frequency of 0.093 Hz and a field maximum of 0.35 T oriented in-plane with the tape face at 77 K.

exposed to an AC magnetic field increase according to Eq (2.43). Since the magnetization loss was the only mode of loss measured during this experiment, the losses from the transport current power supply were not recorded or reported in Fig 4.23.

4.3 Error Analysis

4.4.1 *Critical Current Error*

The error for each experiment was very different for the critical current measurements and the AC loss measurements since each experimental setup used different equipment and was, therefore, determined separately. Errors in the critical current measurements were expected from sample orientation with relation to the external magnetic field, thermal voltage difference in the voltage taps, and magnetic field drift. The magnetic field orientation was set by eye and was deemed accurate to about 2°. The current in the magnet was monitored through a shunt resistor on the magnet power supplies to maintain a constant magnetic field over the measurement period. The critical current measurements were repeated several times for the same sample at constant conditions. The critical currents measured were all within 3%.

4.4.2 AC Loss Error

The errors in the AC loss measurements were much more significant than in the critical current experiments. The signal measured from the sample coil was in the 0.1 μV range when the sample was mounted. A low frequency background noise of unknown origin was observed during the data acquisition. When the pickup coil was mounted without the sample and the inductive background was cancelled out, the measured signal was

approximately half of the measured signal when the sample was mounted. The noise was measured by the lock-in amplifier even when the pickup coils were not attached and the inputs of the lock-in amplifier were shorted. The subtraction of this background was performed for each measurement. This noise was not small for the sensitivity required of the experiment. However, an average value that was nearly constant over the entire measurement time of 20 to 30 min was easily obtainable.

An average value of the V_{rms} signal was obtained for each condition by measuring the value for 30 min time spans with the sample mounted. A value was determined for the background noise by removing the sample and performing all tests without the sample. The voltages measured without the sample were subtracted from the voltages with the sample to eliminated the background noise from the measured data. The error bars were determined by averaging the high extreme values for the upper bar and the low extreme values for the lower bar.

5 Conclusions and Future Work

5.1 Conclusions

The goal of this thesis was to measure the critical currents and AC losses in high temperature superconductors for low frequency field sweeps and temperatures typical of fusion environments. An experimental station was designed to measure the critical current and AC losses of HTS samples approximately 11 in. in length. A test probe with heater and pickup coil configuration was designed and constructed at NW-22 of the Plasma Science & Fusion Center at MIT. A chart recorder and computer were used for data acquisition.

The critical currents were measured as a function of magnetic field strength and temperature for the VAC-1 and VAC-2 samples, which were BSCCO-2223/Ag tape superconductors approximately 11 in. long. The effects of the magnetic field orientation and transport current ramp speed on the critical current were also investigated. The AC losses of a BSCCO-2223/Ag tape superconductor in an AC magnetic field were measured as a function of peak magnetic field amplitude, frequency, and transport current at very low frequencies. Conclusions from this experiment are stated below:

5.1.1 Critical Current Measurements

The critical current data was well described by the Kim-like critical state model given by Eq (4.1) and shown again here.

$$I_c(B) = \frac{I_c(0)}{\left[1 + \left(\frac{B}{B_k}\right)^{\beta}\right]} \tag{4.1}$$

The B_k and β parameters of the VAC-1 and VAC-2 samples were determined by fitting the measured data with Eq (4.1). The B_k parameter is a function of temperature as well. The B_k parameter decreases from 10^{-1} T to 10^{-3} T as the temperature increases from 77 K to 110 K. The B_k parameter is also 10 times larger when the magnetic field is oriented in-plane with the magnetic field than when the magnetic field is perpendicular to the broad face of the tape. The critical current measurements were unaffected by the transport current ramp speed over the range of 6 A/min to 120 A/min.

The measured values for the critical current were repeatable and precise within approximately 3% error. Some samples show very low critical currents because the critical current measurement technique determined the worst value of the critical current over the region between the voltage taps. If any small region of the test area goes normal, a voltage is recorded. Therefore, any cracks or breaks that affect the filament bridging in the measurement region will affect the critical current value.

5.1.2 AC Loss Measurements

The experimental technique for measuring the AC losses at low frequencies gave results which are in reasonable agreement with theoretical predictions during the first attempt at this new experiment. This is a first order technique that is consistent with earlier work at higher frequencies but requires some improvements. Future work to understand the

background oscillation errors and to increase the signal-to-noise ratio is suggested in the second half of this chapter.

The AC loss measurements were well described by the Bean model at higher magnetic fields while the Kim model was more accurate for the losses at lower magnetic fields. However, the trend of the AC loss measurements with increasing magnetic field was linear, as predicted by the Bean model. The differences between the accuracy for the Bean model and the Kim model was the result of the critical current profile with respect to the magnetic field. The critical current was relatively constant at fields above 0.20 T, which is the main assumption in the Bean model. The critical current was greatly affected by the magnetic field at field strengths below 0.20 T and was well described by the Kim model for critical current. The VAC-2 sample and IGC-1 sample both showed a strong degree of filament coupling as described by the effective slab thickness. Both samples were better described by the monofilament case than for the multifilament case. Filament coupling and monofilament behavior for the IGC-1 sample was reported by Suenaga [24].

The discrepancies in the critical current values arise from the sensitivity of the superconductor to the perpendicular component of the self-field induced from the transport current and from the electro-magnetic coupling of the superconducting filaments. The long sample length provides long paths for circulating supercurrents to couple the filaments even at low frequencies of 0.1 Hz. In summary, the self-field critical

current determined from the four-terminal measurements will underestimate the critical current, and, hence, the AC losses calculated from the Bean model and the Kim model.

5.2 Future Work

The test probe was designed to fit the bore of a 2 T dipole magnet and a temperature controlled cryostat. The test probe, therefore, has the capability to measure the AC losses of HTS samples in a temperature range of 4.2 K to 120 K and in magnetic fields up to 2 T. The measurement circuit is also easily adapted to investigate the losses in HTS samples with AC transport currents in DC magnetic fields and AC transport currents in AC magnetic fields.

5.2.1 Signal-to-Noise Ratio

The signal-to-noise ratio must be improved to increase the accuracy of the measurement. Three suggestions to increase the signal are

1) Increase sample volume
2) Increase magnetic field amplitude
3) Increase pick up coil turns.

These suggestions are considered individually in the following sections.

5.2.2 Increase Sample Volume

Increasing the sample volume in the measurement area increases the total amount of loss in the sample and, hence, more signal is measured. One way to increase the sample volume would be to wind the tape into a coil. This method allows more material in a smaller volume. This suggestion would require a different magnetic field configuration

to reproduce the conditions in this paper, but magnets are available or easily constructed to provide the magnetic field orientations consistent with this experiment. However, the high temperature superconductor samples are very brittle and the critical currents degrade severely at modest bending radii.[22]

Another suggestion to increase the superconductor volume in the test region would be to stack the superconductors one on top of the other. Tests by Suenaga [24] have shown that the losses at low and high fields reach constant values separately and asymptotically when the number of tapes in the stack is greater than 20. However, it is not clear what effect stacking the tapes has on the internal field distribution. Since the superconducting regions in the slab are separated by the outer silver matrix of the tapes, the internal field distribution may not be close to that which is expected for a homogenous superconductor. Calculations by Matawari [31] have shown that the field profiles in a stack of thin superconducting platelets are essentially the same as those given for the Bean critical state model when the ratio of the distance between the platelets in a stack and the half width of the platelets is less than 0.2. Based on this information, a stack of approximately 30 tapes that are stacked very closely together would increase the signal and not change any underlying assumptions.

5.2.3 Increase Magnetic Field Amplitude

The AC losses are linearly proportional to the magnetic field amplitude. Therefore, increasing the field amplitude will immediately increase the measured signal. The probe was designed to fit the bore of a 2 T superconducting dipole magnet. Measurements of

the field profile and ramp rates of the magnet need to be made. These tests are easily performed and the increase in signal is instantaneous.

5.2.4 Increase Pick Up Coil Turns

Increasing the number of turns of the sample pick up coil will immediately increase the voltage recorded by the lock-in amplifier. The voltage in the pick up coil is induced from the magnetization flux from the HTS samples. Since the flux linkage is measured over a larger area, the signal is larger. However, the inductive background noise from the alternating magnetic field is also larger. Therefore, a larger balancing coil must be constructed to balance the increased background noise measured by the sample pick up coil.

5.2.5 Heater Improvements

Improvements to the heater are necessary before AC loss measurements at varying temperatures can be made. The sample pickup coil is placed between the copper plate and the sample and reduces the contact area. This reduces the heat conduction to the sample and the efficiency of the heater. Increasing the heater power would result in a larger heat flux and, hence, greater heat conduction. However, the temperature gradients would increased as well and the temperature would be harder to stabilize.

Warming the vapor before it reaches the sample is another idea to improve the efficiency of the heater. Resistive wires carrying transport currents could be wrapped around the open end of a cylinder with the test probe inside. The vapor rising through the cylinder is

heated by the power dissipation in the wires. This reduces the temperature difference between the vapor and probe and also decreases temperature gradients across the probe and sample. This method would allow for shorter time periods for temperature stabilization and would decrease the power requirement to the heater.

6 References

1. Rose-Innes, A.C., Rhoderick, E.H., *Introduction to superconductivity*, Pergamon Press, Oxford, (1978).

2. Wilson, M.N., *Superconducting Magnets*, Oxford University Press, (1983).

3. Minervini, J.V., *Superconducting Magnets Class*, Lecture Notes, Massachusetts Institute of Technology, Spring Term (1998).

4. Gung, C.Y., *Energy Dissipation of Composite Multifilamentary Superconductors for High-Current Ramp-Field Magnet Applications*, PhD thesis, Massachusetts Institute of Technology, USA, (1993).

5. Hoenig, M.O., "Internally Cooled Cabled Superconductors", *Cryogenics*, (1980).

6. Bottura, L., Mitchell, N., and Minervini, J. V., "Design Criteria for Stability in Cable-in-Conduit Conductors", *Cryogenics*, Vol. 31, (1991).

7. Private conversations Takayasu.

8. Hassenzahl, W., "Superconducting Magnetic Energy Storage", *IEEE Transactions on Magnetics*, Vol. 25, No. 2, (1989).

9. Luongo, C. A., "Superconducting Storage Systems: An Overview", *IEEE Transactions on Magnetics*, Vol. 32, (1996).

10. Takayasu, M., Kelland, D. R., Minervini, J. V., "Continuous Magnetic Separation of Blood Components from Whole Blood", *IEEE Transactions on Applied Superconductivity*, Vol. 10, No, 1, pp 927 – 930, (2000).

11. Miller, Luitpold and Löser, Friedrich, "System Characteristics of the Transrapid Superspeed Maglev System", *15th International Conference on Magnetically Levitated Systems and Linear Drives*, pp 19-24, (1998).

12. Soejima, Hiroumi, and Isoura, Katsutoshi, "Development of the Maglev System in Japan: Past, Present, and Future", *15th International Conference on Magnetically Levitated Systems and Linear Drives*, pp 8-11, (1998).

13. Nakashima, Hiroshi, and Isoura, Katsutoshi, "Superconducting Maglev Development in Japan", *15th International Conference on Magnetically Levitated Systems and Linear Drives*, pp 25-28, (1998).

14. Yamanashi Maglev Website, (WWW)
http://www.rtri.or.jp/rd/maglev/html/english/mlx01_E.html
(accessed 5 January 2000).

15. Iwasa, Yukikazu, *Case Studies in Superconducting Magnets*, Plenum Press, New York, (1994).

16. Meissner, W., and Ochsenfeld, R., *Naturwissenschaften*, 21, (1933), 787.

17. Serway, Raymond A., *Physics For Scientists & Engineers*, Saunders College Publishing, (1990).

18. London, F. and London, H., *Proc. Royal Society*, A149, London, (1935), 71.

19. Halley, J. Woods, Editor, *Theories of High Temperature Superconductivity*, Addison-Wesley Publishing Company, Inc., (1988).

20. Young, Hugh D., *University Physics – Extended Version with Modern Physics*, Addison-Wesley Publishing Co., 8th ed., pp 928-930, (1992).

21. Private conversations Minervini.

22. Miyamoto, K., Amemiya, N., Banno, N., Torii, Y., Hatasa, E., Mizushima, E., Nakagawa, T., "Measurement and FEM Analysis of Magnetization Loss in HTS Tapes", ASC, No. LLB-04, (1998).

23. Kwasnitza, K., Clerc, S., Flükiger, R., Huang, Y., "Reduction of alternating magnetic field losses in high-Tc multifilament Bi(2223)/Ag tapes by high resistive barriers", *Cryogenics*, Vol. 39, (1999).

24. Suenaga, M., and Ashworth, S.P., "AC Losses Due to Magnetic Fields and Transport Currents", *IEEE Transactions on Applied Superconductivity*, Vol. 9, No. 2, June (1999).

25. Ciszek, M., Glowacki, B.A., Campbell, A.M., Ashworth, S.P., Liang, W.Y., "Influence of External Magnetic Field and its Orientation on Transport AC Losses in Bi-2223 and Tl-1223 Silver Sheathed Tapes", *IEEE Transactions on Applied Superconductivity*, Vol. 7, No. 2, (1997).

26. Spreafico, S., Gherardi, L., Fleshler, S., Tatelbaum, D., Leone, J., Yu, D. and Snitchler, G., *IEEE Transcripts On Applied Superconductivity*. 9, 2159 (1999).

27. Kim, Y.B., Hempstead, C.F., and Strand, A.R., *Physical Review*, Vol. 139, 1965.

28. Kim, Y.B., Hempstead, C.F., and Strand, A.R., "Magnetization and Critical Supercurrents", *Physical Review*, Vol. 129, 1963.

29. Bean, C.P. and Livingston, J.D., Physical Review Letters, Vol. 7, 306 (1964).

30. Fukunaga, T., Inada, T., Oota, A., "Current Distributions and AC Losses in Self-Fields for Superconductor Tapes and Cables", *IEEE Transactoions on Applied Superconductivity*, Vol. 9, No. 2, June (1999).

31. Matawari, Y., *Physical Review*, **B54**, 13215 (1996).

Appendix A

The CGR sensors were calibrated against a silicon diode that was previously calibrated. The CGR sensors were mounted on a copper heating plate along with the Si-diode. The sensors were wrapped in stryo-foam and immersed in a liquid helium bath. Current was supplied to a copper coil beneath the copper plate. The copper plate was heated through the Joule dissipation in the copper coil. As the temperature increased, the resistance of the CGR's decreased and was recorded. The results of the CGR calibration are given in Fig 7.1.

The magnetic field uniformity was also measured to determine the location of the most uniformly distributed magnetic flux between the pole pieces of the copper electromagnet. A hall probe was used to measure the magnetic field. The hall probe was placed at points between the pole pieces within the bore of the copper magnet. The magnetic field was measured from the top of the pole pieces to the bottom of the pole pieces, from the back to the front of the pole pieces, and from the right pole piece to the left copper coil. Fig 7.2, Fig 7.3, and Fig 7.4 show the results of the magnetic field uniformity measurement between the copper coils. The magnetic field drops at the left copper coil because the left pole piece was removed to make room for the dewar. The disturbance in the magnetic flux was far enough away from the sample to assume that the magnetic field was uniform in the presence of the sample. Fig 7.5 shows a plot of the magnetic field strength versus the magnet current. This plot was used to set the desired external magnetic field.

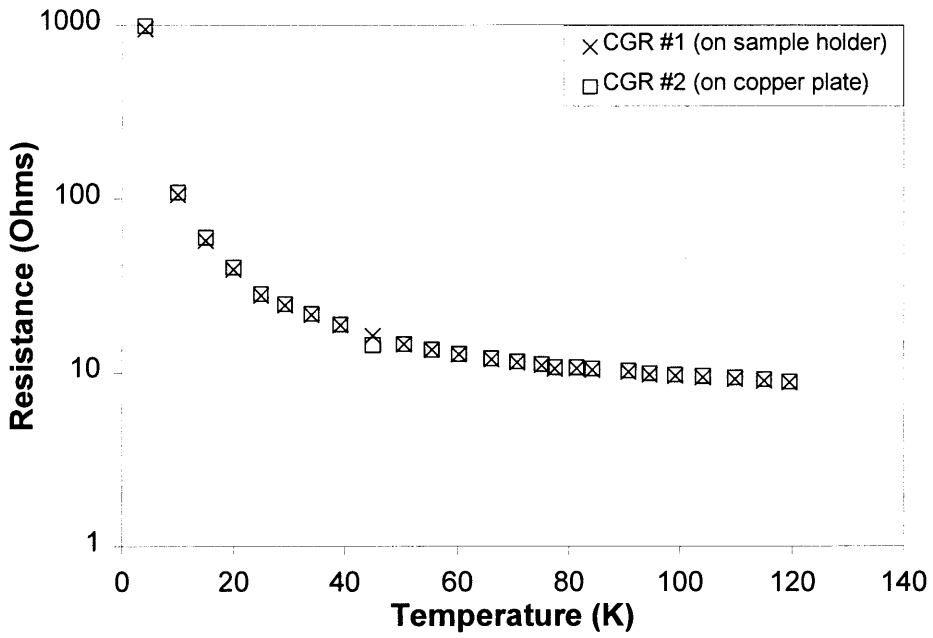

Figure A.1 Resistance as a function of temperature for 2 different CGR sensors.

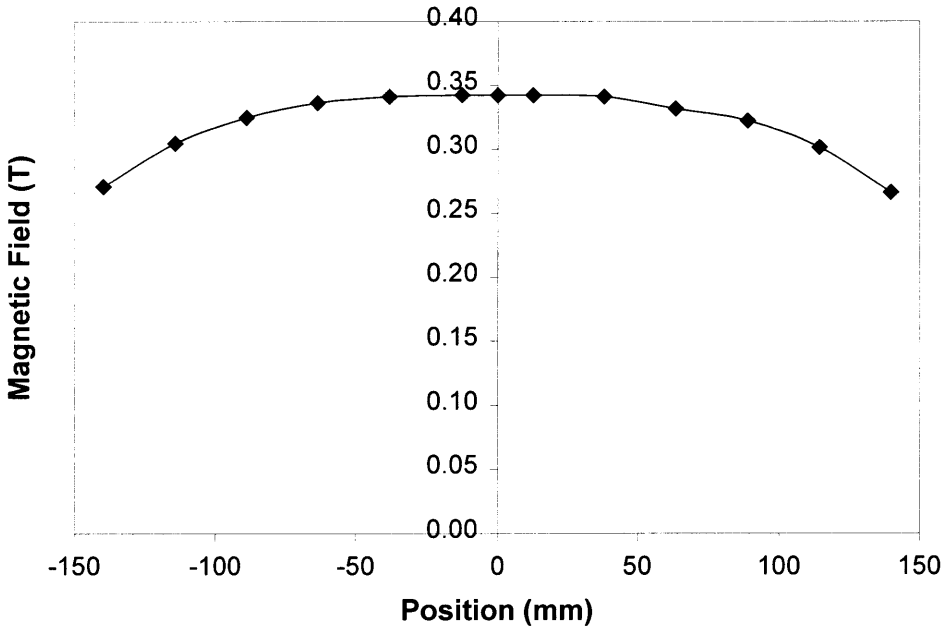

Figure A.2 Magnetic field distribution within the copper coils from the right coil to the left coil. The zero position corresponds to the center of the bore, -90 mm is the right coil, and 140 mm is the left coil.

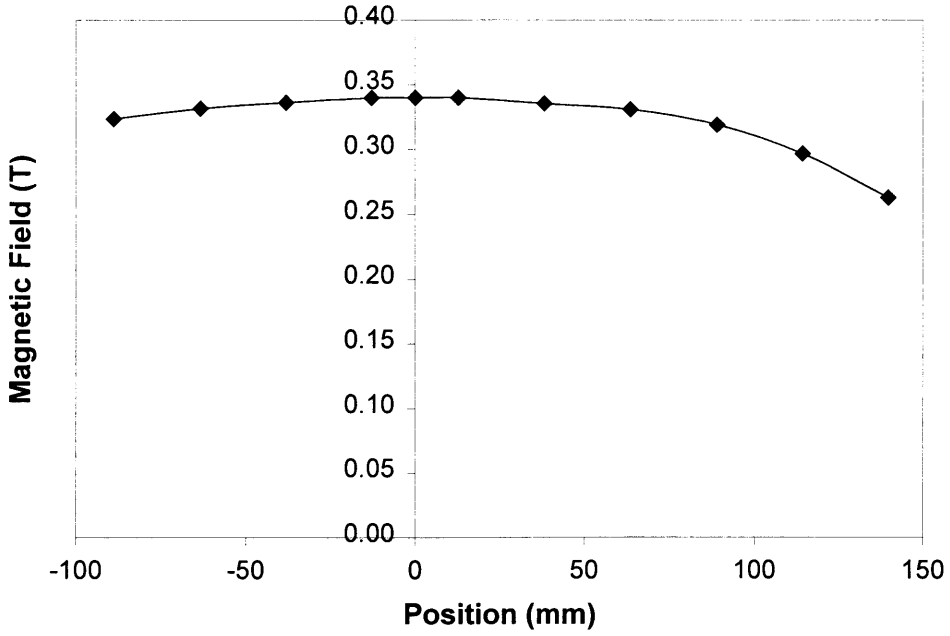

Figure A.3 Magnetic field distribution within the copper coils from the back of the pole piece to the front of the pole piece. The zero position corresponds to the center of the pole piece, -90 mm is the back of the pole piece, and 140 mm is the front of the pole piece.

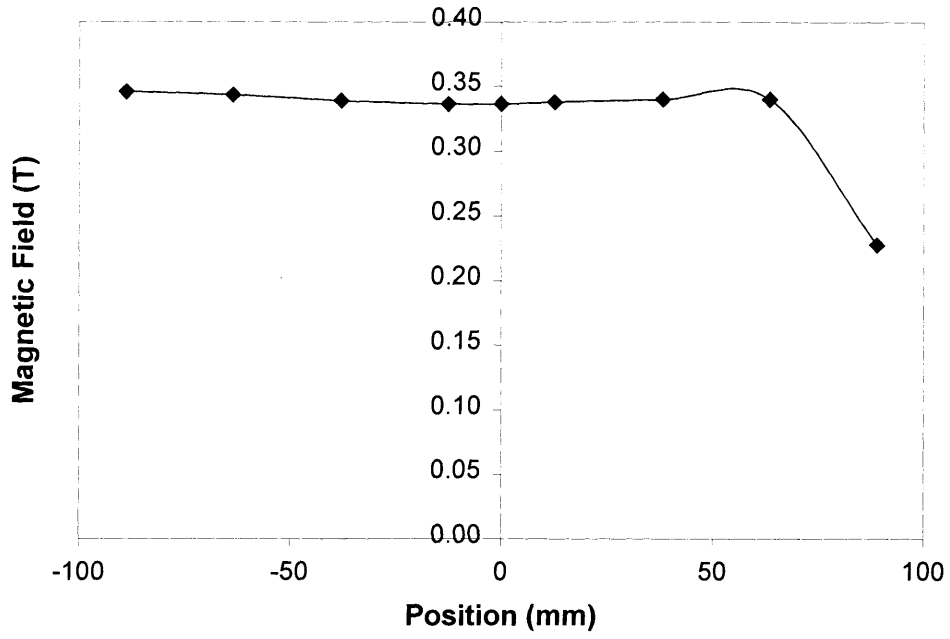

Figure A.4 Magnetic field distribution within the copper coils from the right coil to the left coil. The zero position corresponds to the center of the bore, -90 mm is the right coil, and 140 mm is the left coil.

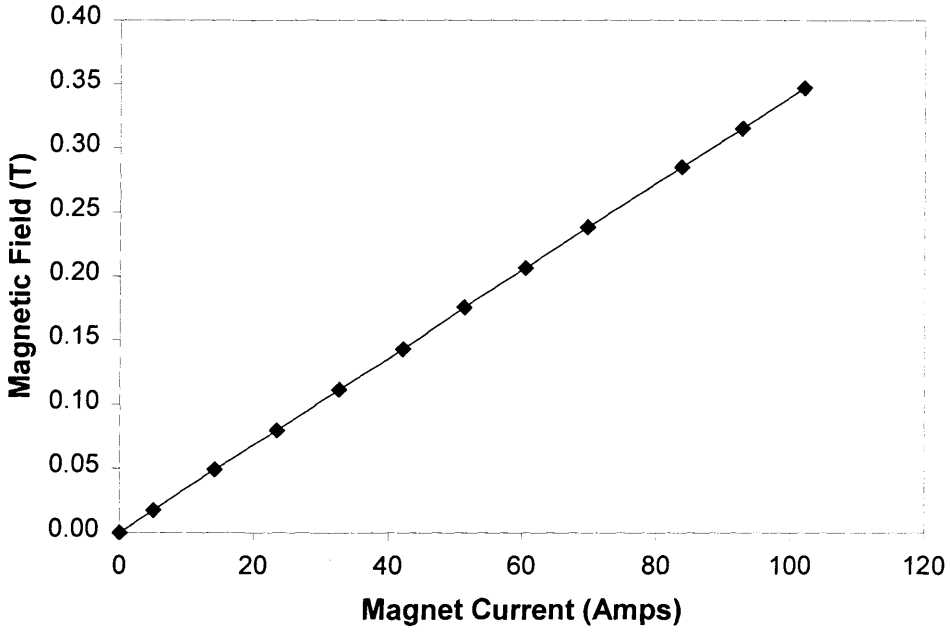

Figure A.5 Magnetic Field as a function of magnet current for the copper electromagnet.

Appendix B

The following design drawings are the basic parts for the construction of the test probe. The probe head was attached to the top of the G10 plate using screws. The sample holder was attached to the end of a 1.35 m G10 tube, which had a 12.7 mm inner diameter and 15.9 mm outer diameter, using a screw as well. Then, the G10 tube was connected to the G10 plate and probe head by inserting a hollow tube made of aluminum with the outer diameter just a bit smaller than the 12.7 mm inner diameter on the G10 tube and the hole in the middle of the G10 plate. All parts were secured together using Sty-cast® epoxy. The Sty-cast® was allowed to cure for 24 hours. All wiring and current leads were connected to the probe. Finally, the steel pipe was attached to the bottom of the G10 plate using screws.

REVISIONS				
ZONE	REV.	DESCRIPTION	DATE	APPROVED

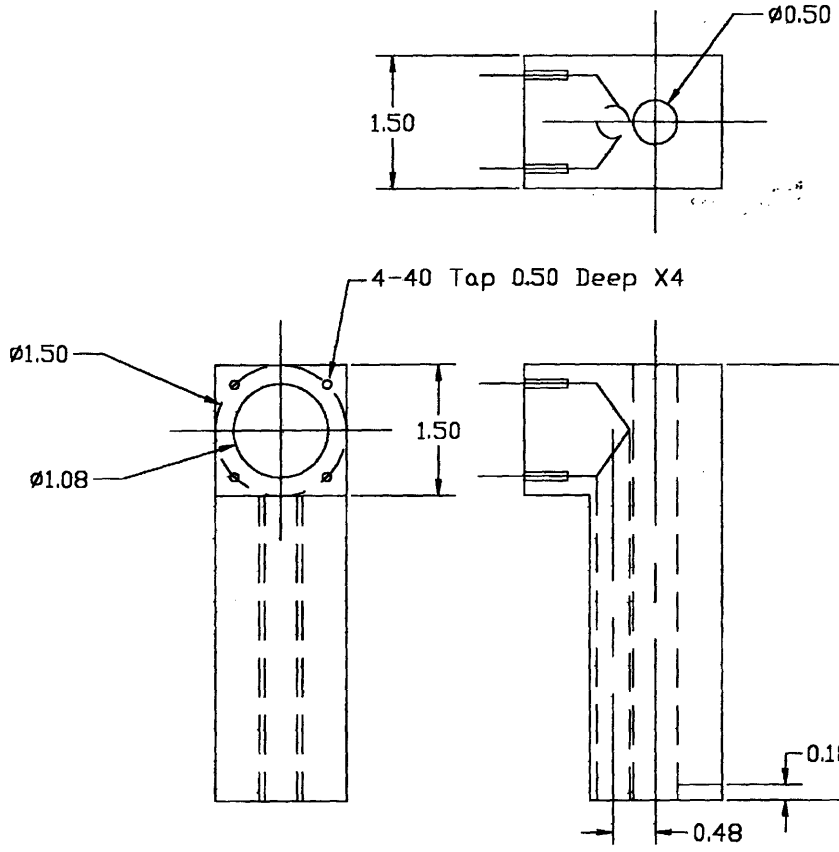

Material: G10

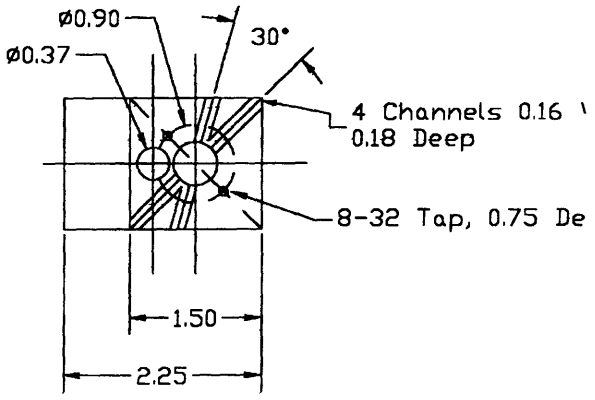

PLASMA FUSION CENTER MASSACHUSETTS INSTITUTE OF TECHNOLOGY	ITEM	PART NO.	DESCRIPTION			QTY.
			Probe Head			DWG A SIZE
TOLERANCES UNLESS OTHERWISE SPECIFIED: DECIMALS; ANGLES ±0.5°; 125; 3 PLACES ±0.005; 2 PLACES ±0.01; 1 PLACE ±0.1; REMOVE ALL BURRS; BREAK SHARP EDGES	DRAWN	T. MacDonald	DATE	7/14/98	DWG NO.	REV
	CHECKED		DATE			–
	APPROVED		DATE			
	CAD FILE		SCALE	None	SHEET 1 of 1	

REVISIONS				
ZONE	REV.	DESCRIPTION	DATE	APPROVED

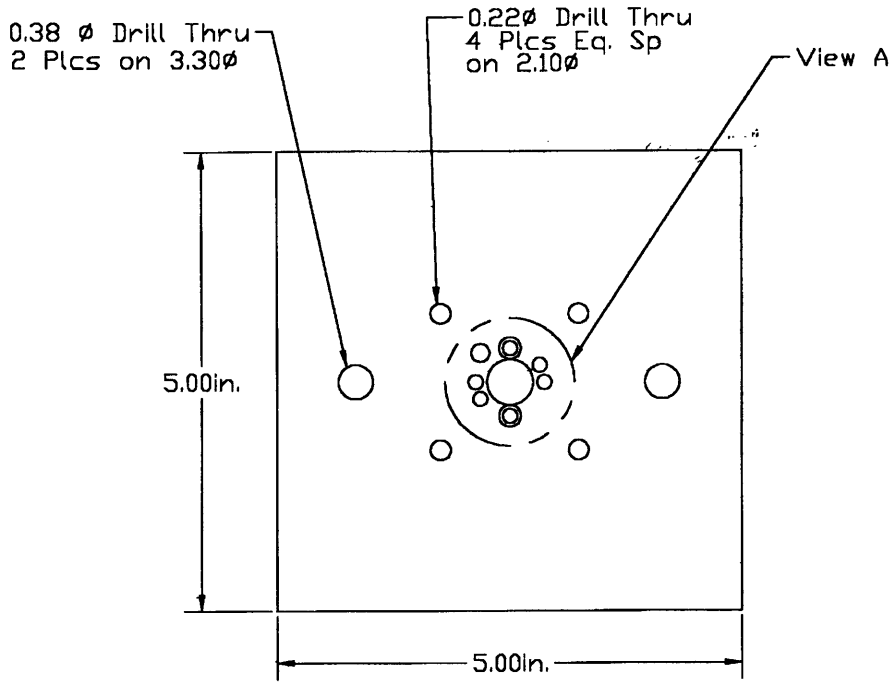

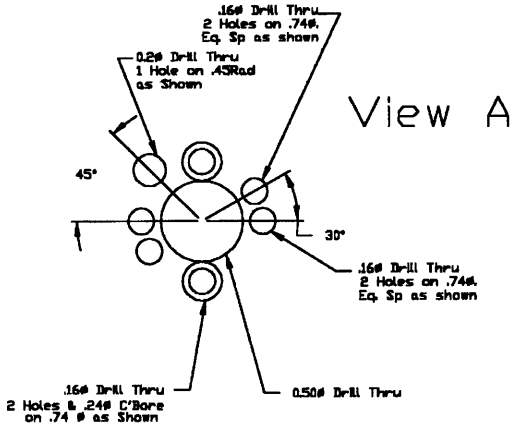

View A

Material: G10
Thickness: 0.25

PLASMA FUSION CENTER MASSACHUSETTS INSTITUTE OF TECHNOLOGY	ITEM	PART NO.	DESCRIPTION			QTY.
			G10 Plate			DWG A SIZE
TOLERANCES UNLESS OTHERWISE SPECIFIED DECIMALS ANGLES ±0.5° 2 PLACES ±0.05 125✓ 3 PLACES ±0.01 REMOVE ALL BURRS 1 PLACES ±0.1 BREAK SHARP EDGES	DRAWN	T. Mac Donald	DATE	7/14/98	DWG NO.	REV —
	CHECKED		DATE			
	APPROVED		DATE			
	CAD FILE		SCALE		SHEET None	

REVISIONS				
ZONE	REV.	DESCRIPTION	DATE	APPROVED

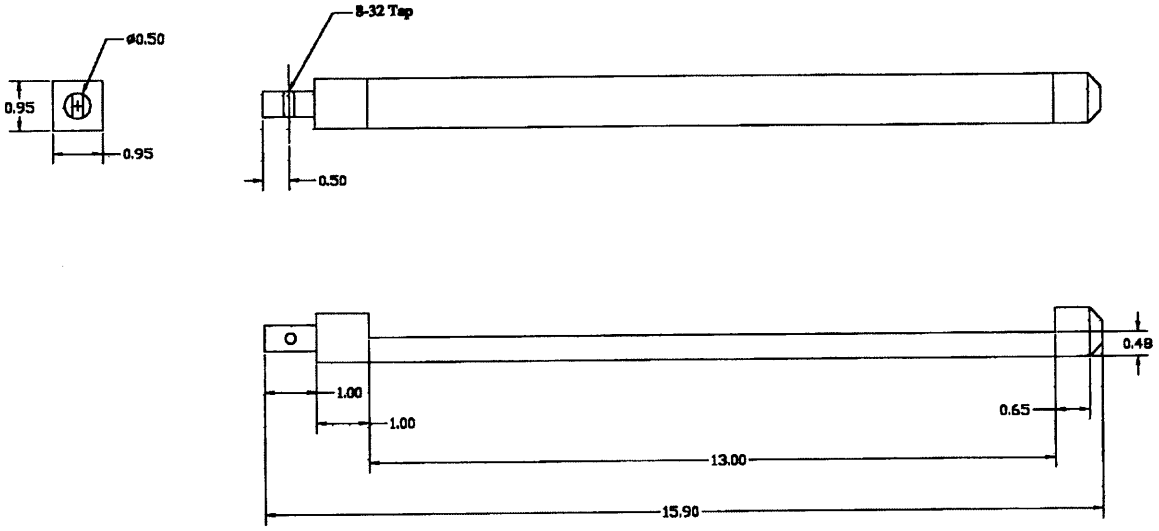

PLASMA FUSION CENTER
MASSACHUSETTS INSTITUTE
OF TECHNOLOGY

TOLERANCES UNLESS OTHERWISE SPECIFIED
DECIMALS ANGLES ±0.5°
3 PLACES ±0.005 125 ✓
2 PLACES ±0.01 REMOVE ALL BURRS
1 PLACES ±0.1 BREAK SHARP EDGES

ITEM	PART NO.	DESCRIPTION	QTY.
		Sample Holder	DWG A SIZE

DRAWN	T. Mac Donald	DATE	7/14/98	DWG NO.	REV —
CHECKED		DATE			
APPROVED		DATE			
CAD FILE		SCALE		SHEET 1 OF 1	

REVISIONS				
ZONE	REV.	DESCRIPTION	DATE	APPROVED

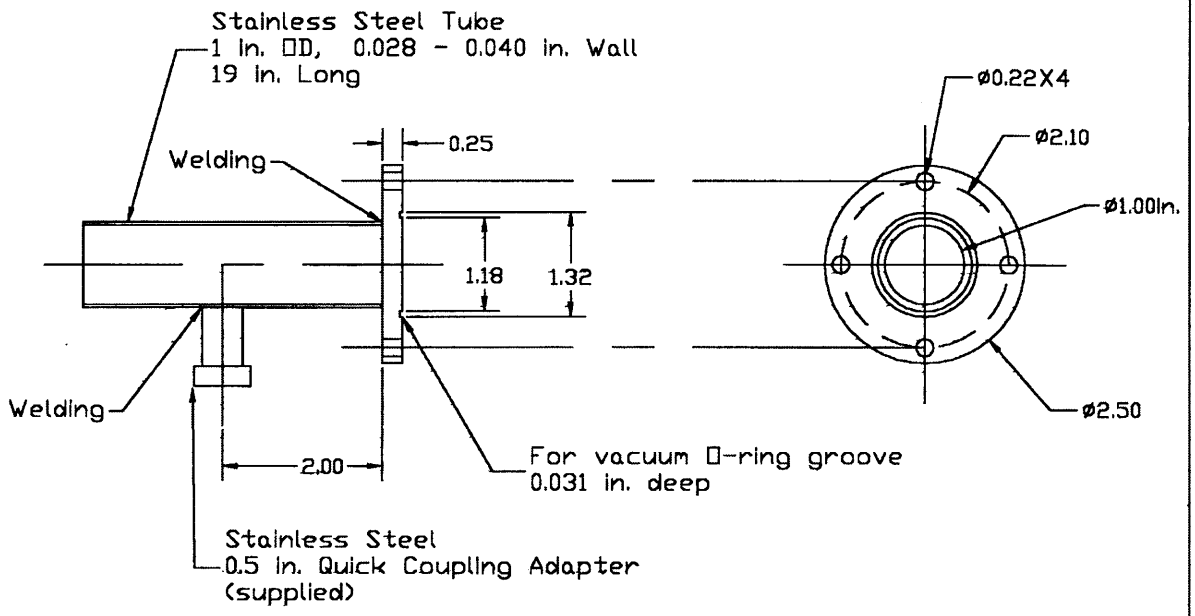

PLASMA FUSION CENTER MASSACHUSETTS INSTITUTE OF TECHNOLOGY	ITEM	PART NO.	DESCRIPTION	QTY.
			Steel Pipe Casing	DWG A SIZE

TOLERANCES UNLESS OTHERWISE SPECIFIED						
DECIMALS	ANGLES ±0.5°	DRAWN	T. Mac Donald	DATE	07/14/98	DWG NO.
3 PLACES ±0.005	125 ✓	CHECKED		DATE		REV —
2 PLACES ±0.01	REMOVE ALL BURRS	APPROVED		DATE		
1 PLACES ±0.1	BREAK SHARP EDGES	CAD FILE		SCALE		SHEET 1 OF 1